Università degli studi di Perugia
Dottorato di ricerca in Fisica
XXII Ciclo

Measurement of the B/C Ratio in Cosmic Rays with the AMS-01 Experiment

Dott. Nicola Tomassetti

Tutori:
Prof. Bruna Bertucci
Dott. Emanuele Fiandrini

Coordinatore del corso di Dottorato:
Prof. Maurizio Busso

A.A. 2008/09

Contents

Introduction

Preface

This thesis evolved from my work on the Alpha Magnetic Spectrometer project. AMS is a particle physics experiment designed for a high precision measurement of cosmic rays in space. AMS-02 is scheduled to be installed on the ISS for at least three years in July 2010. The AMS-01 precursor experiment operated successfully during a 10-day NASA shuttle flight in June 1998. Nearly 200,000 Z>2 nuclei were observed by AMS-01 during the mission. The data collected during this flight have been analyzed in this work with the aim to select charged ions and determine their energy spectra. In this thesis, the measurement of the B/C ratio between 0.35 and 45 GeV/n is presented.

Theoretical Motivation and Experimental Issues

Cosmic Rays (CRs) are the only direct sample of extraterrestrial matter arriving at Earth. The first experimental evidence of the existence of CRs dates back 1900 when Wilson observed the *dark current* effect in air contained in a closed box, and he concluded that a residual ionization was taking place. Wilson also hypothesized that the residual ionization was due to highly penetrating radiation coming from outside the atmosphere. A large number of observations, discoveries and theories were established in the century which followed. Interest in cosmic rays today embraces particle physics, astrophysics and fundamental cosmology.

Among the different components, CR nuclei provide a unique tool to understand the high energy processes occurring in the Galaxy as well as its physical properties. Past measurements of their chemical abundances helped for a qualitatively understanding of the source composition. Precise knowledge of their energy spectra will allow one to describe their production, acceleration and propagation mechanisms in the interstellar medium, validating or discarding specific models. This study is directly connected with new physics coming from the dark matter puzzle that still does not have a compelling explanation. In order to identify eventual new physics contribution and disentangle it from the standard observations, a certain degree of information about the standard component of the CRs is required, as they provide

the astrophysical background on the basis of existing models.

The Boron-to-Carbon ratio is considered one of the most important observables in studying the propagation. Since Boron is known to be absent in CR sources and entirely produced by interaction of Carbon and heavier nuclei through the ISM, the B/C ratio measures the net effect of the galactic propagation. Many effects are involved in determining its characteristic shape, like injection spectra, magnetic diffusion, spallation or re-acceleration.

The study of B/C ratio with the AMS-01 spectrometer presented several experimental challenges due to the reduced measurement redundancy and limited tracker acceptance in the precursor flight. In order to reach a reliable measurement of B/C, an improved charge identification algorithm has been developed. A detailed study of the characteristic energy loss as a function of the particle velocity has been performed to characterize the tracker response to different ion species. A maximum likelihood method has been used in order to combine charge measurements from different tracker layers. Contaminations at the percent level have been estimated in the selected B/C samples based on data and dedicated Monte Carlo simulations.

A deep understanding of CR interactions in the detector as well as the orbital environment are also fundamental issues for an accurate B/C measurement. Geomagnetic cut-off, varying in the $1 \div 15\ GV$ rigidity interval along the AMS-01 orbit, introduced different distortions of the energy spectrum measurement for different chemical species. A detailed study of the geomagnetic cut-off along the orbit and the careful evaluation of these effects have been carried out allowing a sound combination of statistics collected in different orbit locations.

Delta-ray production as well as possible nuclear fragmentation occurring in the detector material can induce different trigger and detection inefficiencies for different nuclear species. Related uncertainties have prevented the AMS-01 collaboration to pursue this measurement in the past. A detailed study of the detector response by means of extensive Monte Carlo simulation has been carried out. A stand-alone *Virtual* MC simulation has been developed for the AMS-01 trigger, with the aim of comparing results from the standard `GEANT3`-based simulation framework with the most recent `GEANT4` and `FLUKA` implemented models. The `AMS-VMC` project is currently under further development for the upcoming AMS-02 experiment.

Outline of the Thesis

Chapter 1 is entirely dedicated to the different aspects of the cosmic-ray propagation throughout the interstellar medium. Their observational properties and the theoretical approaches for acceleration and propagation mechanisms are reviewed. The solar and geomagnetic modulation are also discussed. A short review of the experimental status is then presented. Particular emphasis is given to the description of the role of the B/C ratio.

Chapter 2 describes the AMS experiment. The detector design and its performance are presented with specific information on the STS-91 flight, the trigger, the DAQ and the off-line softwares. In particular, the `AMS-VMC` project is introduced. The main physics results from STS-91 experiment are outlined.

Chapter 3 contains a basic step in the analysis work: the data selection. Analysis cuts based on the quality of the reconstructed quantities are described in the first part of the chapter, with close comparisons between simulations and measured data. The second part describes orbit-dependent cuts applied to the collected data; in particular, the rigidity cut to avoid distortions from the Earth's magnetic field and the shadow of the MIR space station in the nuclear channel.

In **Chapter 4** the new charge identification algorithm is presented. A deep inspection of the characteristic energy loss of charged CRs in the detector is made, and the signal equalization procedure for the different CR species is described in detail. The performance of the charge identification algorithm is presented in terms of efficiency, contamination, and their effect on the B/C ratio. Data from flight, MC simulation and beam test are used.

Chapter 5 deals with the determination of the differential energy spectra, i.e. the techniques used for the transition between the measured data and the B/C ratio. Many experimental issues are described: the acceptance estimation, the study of the trigger efficiency, the detector exposure time and the spectral unfolding. Therefore, the role of the Boron isotopic composition in the B/C is investigated, and the analysis of the various sources of uncertainties is presented. The measurement of B/C between 0.35 and 45 GeV/n is finally derived and discussed.

Chapter 1

Cosmic Rays in the Galaxy

Cosmic Rays (CRs) are charged particles reaching the Earth atmosphere in all directions from the outer space. Cosmic rays observed in the neighborhood of the Earth have undergone a chain of transformations beginning at their source. This includes interactions with matter and magnetic fields, resulting in the destruction of primary particles, production of secondary particles and radiation, energy losses and acceleration processes. The CR flux arriving at Earth is composed of $\sim 98\%$ nuclei and $\sim 2\%$ electrons and positrons. The nuclear component consists of $\sim 87\%$ protons, $\sim 12\%$ helium nuclei and $\sim 1\%$ for all heavier nuclei ($\sim GeV/n$) [1]. The spectra of nuclei extend to energies in excess of $\sim 10^{20}\ eV$. Change in slopes have been measured near $\sim 10^{15}\ \div 10^{16}\ eV$ and above $10^{19}\ eV$.

The understanding of the observed spectra and composition requires a consistent picture of the origin and propagation of cosmic rays. Several proposals have been made on the origin, propagation and confinement of relativistic cosmic-ray nuclei with energy between $\sim 10^8$ and $10^{15}\ eV$, thought to have galactic origin (GCR). The fundamental issues of GCR physics can be summarized as: (1) the sources of primary particles, (2) the acceleration processes, (3) the galactic propagation, (4) the propagation in the solar system. The picture continues to evolve as observations improve with time and it has stimulated a variety of models and theories.

In particular, among their different components, CR nuclei provide a unique tool to understand several aspects of the most energetic processes in the Universe. The study of the nuclear component of the CRs is directly connected with new physics coming from dark matter and dark energy, which are still poorly understood [2]. To explain this puzzle the efforts are mainly focused on new type of particles, whose existence is supported by non-standard theories of fundamental interactions. In order to identify eventual contribution of new physics and disentangle it from the standard processes, a high degree of knowledge is required about the standard component of

the CR. The measurement presented in this thesis is motivated by this last reason.

In this chapter, a complete review of CR astrophysics in the galactic medium is presented. Some general observational features are outlined in Section §1.1. Sections §1.2 and §1.3 are dedicated to the description of the journey of a galactic CR nucleus, from its origin to our instruments, with a survey of each process that occur during propagation throughout the Galaxy (§1.2) and the Earth's vicinity (§1.3). Section §1.4 is mostly focused on the physics of the Boron-to-Carbon ratio, i.e. the role of secondary CR nuclei for understanding the propagation mechanism and the experimental status of the B/C and CR nuclei measurements.

1.1 Observational Quantities

The CR energies span over a wide interval, from eV to 10^{21} eV, whereas the all-species differential fluxes vary significantly: from $particle/cm^2/second/MeV$ up to $particle/km^2/century/ZeV$ respectively. CRs with lowest energy $eV/n \div GeV/n$ have a solar origin and make up the solar wind [3]. CRs with energy between 10^9 and 10^{18} eV are thought to originate and accelerated in supernova explosions occurring in the Galaxy. In this picture, particle are accelerated by non-thermal mechanisms that lead to the power-law spectrum described in Fig.1.1:

$$\Phi = \Phi_0 E^{-\gamma} \tag{1.1}$$

where the spectral index γ takes values from 2.5 to 2.8 for the different chemical species. The low energy part of the GRC spectrum ($E < 10$ GeV/n) is influenced by the solar wind; solar modulation is discussed in §1.3.1.
At energies $\sim 10^{15}$ eV the CR spectrum has a steeping, the *knee*, characterized by a sudden variation of the all-particle spectral index from 2.7 to 3.1 (Fig.1.2). Two main effects are believed to be at the origin of the knee: (a) the reach of the maximum energy transferable by the cosmic accelerators, and (b) the CR leakage due to a less efficient galactic magnetic confinement [6]. Since these two processes are governed by the magnetic rigidity of the particles, the energy spectra for individual elements should exhibit different breaks for different total energies [7]. This is currently under investigation by the KASCADE collaboration, through measurement of CR composition in the knee region [8].

At higher energies, two breaks, a *second knee* and the *ankle*, are observed in the spectrum at 10^{17} and 10^{18} eV respectively. Above the ankle, a flatter spectrum is observed, with $\gamma \approx 2.7$. This particular structure is believed to be related to the transition between galactic and extra-galactic origin of the CR fluxes.
In the highest energy region $E > 10^{19}$ eV, the Greisen-Zatsepin-Kuzmin (GZK)

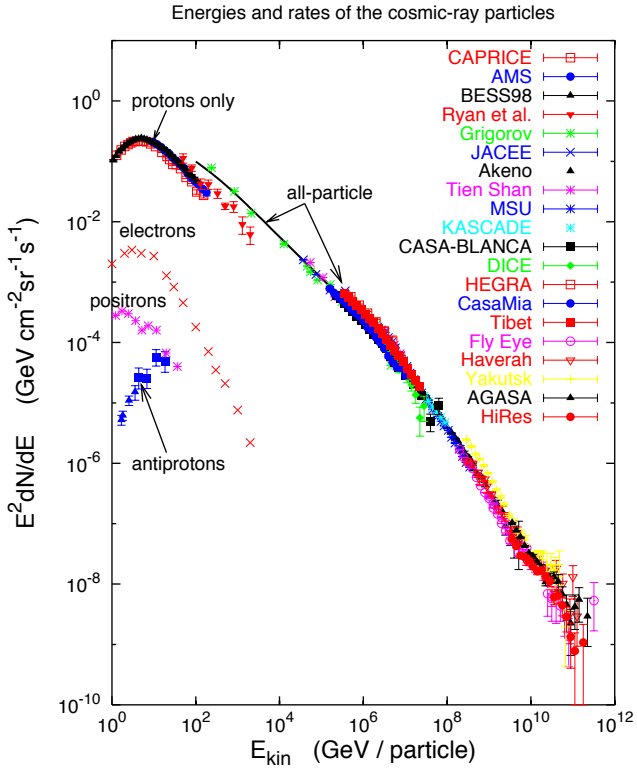

Figure 1.1: All particle cosmic-ray spectrum [4]. The spectrum extents to many order of magnitude and different techniques are used for CR measurements.

suppression is expected on the flux, due to inelastic interactions of cosmic rays with the CMB photons [9]. As the nature and the origin of the highest energetic CRs are nowadays under debate, their straight-line propagation through the galactic and extragalactic magnetic fields has opened a new vision in the astronomy with cosmic rays [10].

In Fig.1.3 the relative abundances of different CR elements is presented in comparison with those observed in the solar system. CR nuclei constitute a genuine sample of galactic matter. Some of them come altered from the sources, other are produced during the propagation throughout the galaxy. Considering the solar system somehow representative of a typical CR source, it is clear an observed over-abundance of cosmic rays in the Li-Be-B group ($3 \leq Z \leq 5$) as well as in the sub-Iron group ($22 \leq Z \leq 25$). Both the elemental groups are not typical products of nucleosynthesis processes [11].
The main mechanism that alters the CR composition from their production to the detection is called *spallation*. When a cosmic ray crosses the Galaxy, it may interact

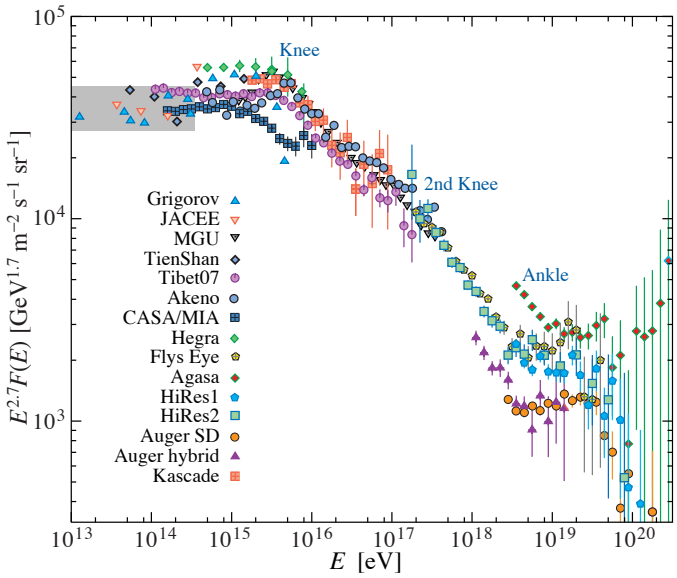

Figure 1.2: The all-particle spectrum from air shower measurements in the high energy region from below the *knee* to above the *ankle* [5]. The spectra are scaled by $E^{2.7}$.

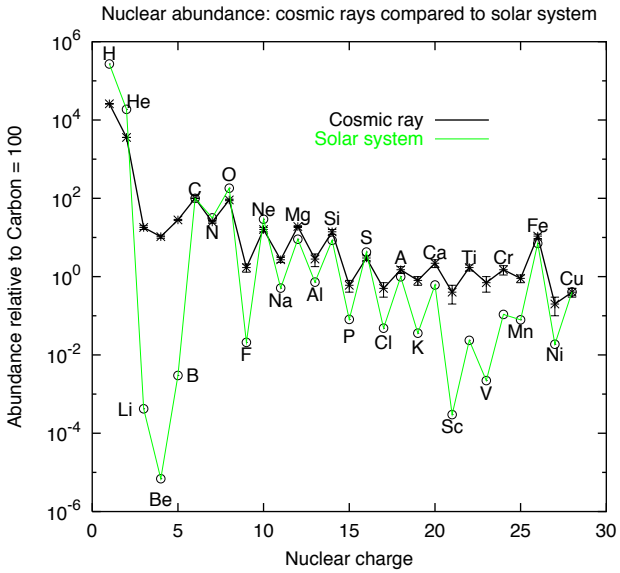

Figure 1.3: Elemental composition of galactic CRs [11] compared with the abundances in the solar system [12] The differences between the two chemical compositions are the fingerprint of secondary CRs, as the Li-Be-B and Sub-Fe group.

with interstellar matter and initiate a nuclear reaction [13]. From Fig.1.3, a less

pronounced odd-even effect is also observed in cosmic rays. Whereas odd-nuclei are weakly bounded and can be destroyed in the stellar thermonuclear reactions, even nuclides are much more stable and then more abundant at the source. Even-nuclei spallation can then contribute to a secondary fraction of the odd-nuclei abundance. A thorough study of this effect and the corresponding cross sections is of fundamental importance for understanding several aspects of the CR propagation.

1.2 Galactic Cosmic-Ray Nuclei

In galactic models the CR sources are located in the galactic disc. Determining the region where cosmic rays are concentrated (i.e. the diffusion region) is a different issue. Their non-thermal energy spectrum suggests that the most probable candidates are supernovae. Pulsars and neutron stars in close binary system are other possible candidates.
From the energetic point of view, these scenarios are completely acceptable. The average density of CR is $\sim$1 eV/cm^3. With a galactic disc volume of 10^{63} cm^3, the total CR energy content is then $\sim 10^{67}$ eV. The average CR lifetime is $\sim 3 \cdot 10^{14}$ s. Thus the rate of energy supply to maintain a stationary CR flux amounts to $\sim 5 \cdot 10^{40}$ erg/s; this must be provided by injection and acceleration of fresh CRs. Assuming supernova explosion each fifty years ($1.5 \cdot 10^9 s$) and a typical yields of 10^{50} erg in fast particles, it can be estimated an average power of $6 \cdot 10^{40}$ erg.
Thus from energetic point of view, SNs are quite plausible candidates as production sites of CRs.

1.2.1 Acceleration Mechanisms

The mechanisms responsible for CR acceleration are still not totally clear. The great variety of conditions and processes in the cosmos leads to the conclusion that there are different acceleration mechanisms of energetic particles. The sources are characterized by turbulent motion of the medium with the presence of high magnetic and induced electric fields.

Acceleration mechanisms have to justify the relativistic energy and the power law spectrum of cosmic rays. Theories of CR acceleration in the Galaxy have been focused on the Fermi acceleration theory [14], known as *second order Fermi acceleration*. In Fermi's original picture, charged particles are reflected from magnetic "mirrors" associated with irregularities in the galactic magnetic field. The mirrors are assumed to move randomly with typical velocity V. The particles gain energy statistically in these reflections. In the relativistic limit, the average energy gain per

collision is:

$$\left\langle \frac{\Delta E}{E} \right\rangle = \frac{8}{3} \left(\frac{V}{c} \right)^2 \tag{1.2}$$

This illustrates the famous result derived by Fermi that the average increase in energy is only *second order* in V/c. Since the same fractional increase occur per collision, it is apparent that the energy enhancement due to multiple reflections lead to a power low energy distribution $N(E) \propto E^{-\gamma}$. This process predicts the spectral index as:

$$\gamma = 1 - \frac{1}{\alpha \tau_e} \tag{1.3}$$

where τ_e is the mean time spent by a particle in the accelerating regions, and α reflects the typical rate of energy gain per collision. Both the quantities have to be derived with specific assumptions. In the modern version of the Fermi second order mechanism, the particles interact with various types of plasma waves and gain energy being scattered stochastically by these so-called Alfvén waves. The interactions between CR particles and Alfvén waves become increasingly ineffective at higher energies because of the falling power law nature of the primary spectrum. This process is quite attractive from the point of view of the diffusion of CR in the Galaxy.

A very attractive version of CR acceleration is based on *first order Fermi acceleration* through individual head-on collision leading to a more efficient energy gain. The framework is that of a strong shock wave propagating at a super-sonic velocity V parallel to the magnetic field direction lines through interstellar gas [15, 16]. One assumes that V is higher than the Alfvén velocity. In the shock reference frame, the gas is flowing with upstream velocity, relative to the shock, of $u_2 = V$. At the shock, the gas is compressed by a factor ξ, so that the downstream velocity, relative to the shock, is $u_2 = V/\xi$. The presence of scattering centers is postulated, so that cosmic rays diffuse on both sides of the shock, i.e. their motion is randomized in the downstream/upstream reference frames, where the scattering centers are frozen. Every passage through the shock is therefore equivalent to running head-on into the magnetic wall of velocity

$$W = u_1 - u_2 = V(1 - 1/\xi) \tag{1.4}$$

Averaged over all incidence angles, the mean energy gain per traversal of the shock is given by:

$$\Delta E = \frac{4}{3} \frac{V}{c} \left(1 - \frac{1}{\xi} \right) E \tag{1.5}$$

The probability P of a particle escaping the system can be estimated as $P = 1-(V/c)$ by the classical kinetic theory [17]. Taking proper account the escape probability,

this model leads to the time-independent spectrum:

$$N(E) \propto E^{-\gamma} \qquad \gamma = (2+\xi)/(\xi-1) \tag{1.6}$$

For strong adiabatic shocks, $\xi \approx 4$ and $\gamma \approx 2$. Weaker shocks generate steeper spectra. It is remarkable that the slope of the power law spectra generated by this mechanism depends only on the shock strength or the size of the scattering region. This spectral form is expected to apply to a wide range of energies, up to some TeV. The reason that this mechanism has excited so much interest is that, for the first time, there are excellent physical reasons why power-law energy spectra with a unique spectral index should occur in diverse astrophysical environments.
In this simplest version of the theory, the only requirements are the presence of strong shock waves and that the velocity vectors of the high energy particles are randomized on either side of the shock. It is entirely plausible that there are strong shocks in most sources of high energy particles, SN remnants, active galactic nuclei and the diffuse components of extended radio sources.

1.2.2 Propagation Models

The CR propagation in the Galaxy is dominated by particle motion in the galactic magnetic field. Cosmic rays move in helical trajectories around the large-scale field lines and interacts with its small irregularities, that act as collision-less scattering centers. The process is naturally described by means of diffusion theories. The galactic magnetic field extends out of the disc in a larger halo that designs the region where the diffusion takes place. Therefore a cosmic ray particle, in its travel from the source to the Earth, may accede to regions where the propagation conditions are different. Thus, a complete treatment of cosmic ray transport, has to consider diffusion in the full magnetic halo region.

The CR propagation is generally described by a transport equation which includes source distribution, particle diffusion in the galactic magnetic field, energy losses, nuclear interactions, decays and acceleration processes. Hereafter kinetic energy per nucleon will be used (just *energy*, for short, in this thesis), since this is the appropriate parameter to be used for CR nuclei, as it is conserved in nuclear reactions. The most known formulation was proposed by the Ginzburg-Syrovatskii [18] with the transport equation:

$$\begin{aligned}\frac{\partial N_j}{\partial t} = &+ \nabla \cdot (\mathbf{D}\nabla N_j) - \nabla \cdot (\mathbf{V} N_j) - \frac{\partial}{\partial E_j}\left[b_j(E) N_j(E)\right] \\ &- p_j N_j + \sum_{k>j} \left[N_k \cdot p_{k\to j}\right] + Q_j(E, \mathbf{r}, t)\end{aligned} \tag{1.7}$$

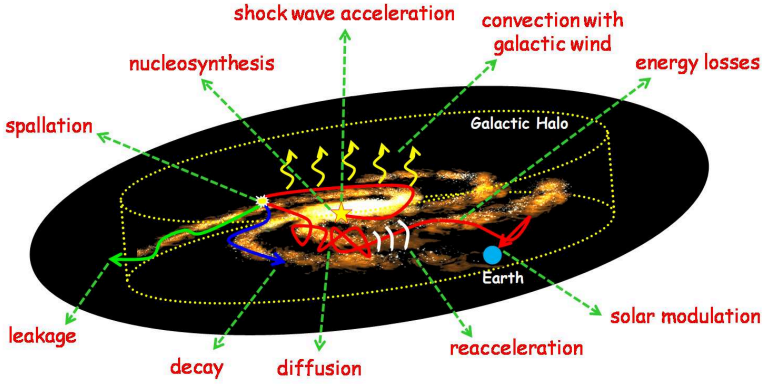

Figure 1.4: A schematic view of the galactic cosmic-ray nucleus propagation history. The nucleus is synthesized in a stellar process and accelerated. It wanders in the Galaxy trapped by the magnetic field for $\sim 10^7$ years, during which its energy and identity change, due to a variety of processes that are discussed in the text.

Many physical processes are contained in the equation. The physical meaning of the various terms is outlined as follows:

- **CR Density.** $N_j(E, \mathbf{r}, t)$ is the number density of particles of the $j-$th kind defined as:
$$N_j(E, \mathbf{r}, t) = \frac{1}{\nu} \int \phi_j(E, \mathbf{r}, t, \hat{\omega}) \cdot d\Omega \tag{1.8}$$
Here $\phi_j(E, \mathbf{r}, t, \hat{\omega})$ is the cosmic ray flux in the direction $\hat{\omega}$, and $d\Omega$ is the element of solid angle. $N = \frac{4\pi}{\nu}\phi$ for isotropic intensity.

- **Diffusion.** The first term on right hand side (hereafter RHS) describes the diffusion of particles in the turbulent magnetic field. The process is governed by the *diffusion coefficient* D. In a realistic description, it should be a tensor, discerning between its parallel and transverse components with respect to the magnetic field lines. A common parametrization for the diffusion coefficient D is:
$$D = \frac{1}{3}\lambda_D \nu \tag{1.9}$$
where ν is the particle velocity and λ_D is the diffusion mean free path.

- **Convection with galactic wind.** The particle convection with the galactic wind of velocity V_C is described in the second RHS term of Eq.1.7. CRs may not only diffuse in our Galaxy, because it is possible that they are also carried by a magnetic field structure in form of magnetohydrodynamic waves. The effect of this *galactic wind* is to dilute the energy of the particles located

in the disc in a larger volume, so that the adiabatic expansion results in a kind of energy loss (*adiabatic deceleration*), depending on the wind velocity $V_C = V_C(t, \mathbf{r})$. A characteristic value of the convection velocity is 20 $km \cdot s^{-1}$.

- **Energy losses.** The third RHS term represents the continuous energy losses:

$$b_j(E) = -\frac{dE}{dt} \tag{1.10}$$

that expresses the mean rate at which the particle j changes its energy. The only processes relevant for nuclei are ionization and Coulomb losses in ionized plasma. Other effects like bremsstrahlung, inverse Compton and synchrotron radiation are important only for light particles ($e^{\pm}$).

- **Decay and break up.** The term $p_j \cdot N_j$ represents the destruction rate due to collisions and decay, with:

$$p_j = n\nu\sigma_j + \frac{1}{\gamma\tau_j} \tag{1.11}$$

where τ_j is the lifetime of nucleus j for radioactive decay. The interstellar gas density, generally assumed to be hydrogen and helium is parametrized with $n = n(x)$, and σ_j is the total inelastic cross-section for the processes $N_j + ISM \rightarrow$ anything.

- **Spallation.** The sum $\sum_k$ describes the production of nuclei of type j from interactions of nuclei of different types k. Only heavier nuclei ($k > j$) are usually considered in the sum. The probability of the process is also given in terms of production cross sections $\sigma_{k\rightarrow j} \equiv \sigma(N_k + ISM \rightarrow N_j + \text{anything})$:

$$P_j = n\beta c\sigma_{k\rightarrow j} + \frac{1}{\gamma\tau_{k\rightarrow j}} \tag{1.12}$$

where the contribution from heavier radioactive nuclei k to the nuclear channel j is also considered. No energy migration $E_k \rightarrow E_j$ are considered in this term, as long as kinetic energy per nucleon is conserved in *spallation*. This is the main reason why theoretical models use the kinetic energy per nucleon as a fundamental quantity.

- **Source distribution.** Last term in Eq.1.7 is the primary source term. In the most general case it may be time and space dependent, even though stationarity and cylindrical symmetry are often invoked to simplify the problem.

Solving Eq.1.7 requires the complete analysis of a system of coupled equations. Together with the possibility of working out an analytical/numerical solution, an

assumption that all the parameters are well known or needed to be known is mandatory, and additional assumptions have to be done for defining the boundary condition of the equation.

Hence, different models of CR propagation in the Galaxy can be represented using Eq.1.7 with specific boundary conditions and approximations. Three very popular propagation models are presented in the following sections: the Diffusion Halo Model (DHM), the Weighted Slab Model (WSM) and the Leaky Box Model (LBM).

1.2.3 Diffusion Halo Model

The most realistic physical scenario for the CR propagation is a diffusion model in which the diffusion-transport equation is solved by taking into consideration all the physical processes involved together with observational physical constraints [19].

In this model the sources of CRs are distributed within a thin galactic disc; the escape from the disc into the halo and finally into the intergalactic space is determined by diffusion. In a model with diffusion there is a gradient of CR density away from the galactic disc. Consequently, a constant streaming of CR particles away from the galactic disc into the halo is produced. This streaming is determined by the energy dependence of the diffusion coefficient $D(E)$ and the halo size. The basic

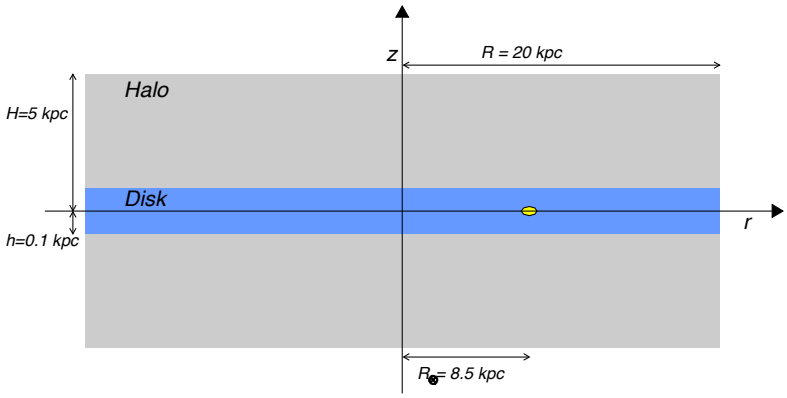

Figure 1.5: Schematic view of the physical concept of the DHM. The blue area symbolizes the thin galactic disc, surrounded by a huge halo, where the diffusion takes place. The sources of cosmic rays are placed in the disc. The CR escape into the halo and finally into the intergalactic space is controlled by diffusion.

quantities to be assumed or determined for defining the boundary conditions are the following:

- Halo Model: the shape and the size of the propagation region of cosmic rays in the Galaxy. Reasonable values are $H \sim 5\ kpc$, $h \sim 100\ pc$, $R \sim 20; kpc$ (see Fig.1.5).

- Gas distribution: spatial density and composition of the interstellar gas. ISM is a rather homogeneous mixture of hydrogen, helium, ionized gas and dust located in a narrow disc with average density of 1 $particle/cm^3$ [20].

- Magnetic field distribution: strength and topology of large-scale field distribution and irregularities. According to radio synchrotron, optical polarization and Zeeman splitting data, the average strength of the total magnetic field in the Milky Way is about 6 μG near the Sun and increases to $20 - 40\mu G$ in the Galactic center region. The overall field structure follows the optical spiral arms, and a radial distribution is a good approximation [20].

- Source distribution: spatial energy distribution of CR sources and composition. The most common used spatial distributions are flat ($Q(r) = 1$) or radial distribution $Q(r) \propto \sqrt{r} \cdot exp(1 - r/r_0)$, with $r_0 = 8.5\ kpc$. However, the difference between a flat and a radial distribution is a mere rescaling of the propagation parameter, i.e. not significant if one consider these parameters as effective in a consistent framework [21, 22]. The energy spectrum is determined by the acceleration processes at work. There is a strong belief that this spectrum is a power-law in rigidity $Q(R) \propto R^{-\alpha}$.

- Diffusion coefficient: the functional form of its space and energy dependences. For isotropic diffusion, it is a good approximation to regard it as constant function of the space coordinates, or at least a two-value function for diffusion in the disc and in the halo. Its energy dependence is usually expressed as a power-law in rigidity $D \propto R^{\delta}$. Its absolute magnitude is related on the level of hydromagnetic turbulence.

- Spallation cross sections: a huge number of cross-sections are involved and their knowledge is today affected by large uncertainties [23, 24]. Actually it is important to know not only the total cross section for the destruction rate of CRs, but also the branching ratios into all relevant channels which give the formation of secondary nuclei.

A simple picture is to define the Galaxy as a disc with semi-thickness $h \approx 100\ pc$ surrounded with a halo of scale height $H \gg h$ (Fig.1.5). This physical concept generally assumes that cosmic ray sources are placed in the thin galactic disc, where most of the interstellar gas is located. Cosmic rays are assumed free to diffuse out,

in the whole halo region, where they are able to spend considerable portions of their lifetime. Escaping the halo is also allowed; out of the region the CR density it becomes zero. A three dimensional diffusion equation would be the proper approach to the problem, that should cover physical details of the galaxy such as the spatial gas distribution of atomic and molecular hydrogen and considers also aspects such as convection with the galactic wind. Secondary and radioactive CR nuclei with decay times comparable with the confinement time play an important role in determining these physical parameters and also provide information on the mean gas density through which the particles propagate.

Since in real astrophysics environment, propagation can be more complex than a simple diffusion, reacceleration of CR particles can also be included. It seems likely that cosmic rays could encounter a number of weak shocks during their propagation through the interstellar medium. This acceleration is continuous and due to magnetic field inhomogeneities. The process can be studied in terms of a diffusion in momentum space provided that the hydromagnetic turbulence may be regarded as homogeneous and time-independent [25]. This involves an additional term in Eq.1.7:

$$\frac{1}{p^2}\frac{\partial}{\partial p}\left[p^2 D_{pp}\frac{\partial N_j}{\partial p}\right] \tag{1.13}$$

where D_{pp} is the diffusion coefficient that acts in the momentum space. If we idealize the magnetized fluid elements as hard spheres with masses much larger than those of the particles, D_{pp} is given for elastic collisions as:

$$D_{pp} = \frac{V_a^2}{3\lambda c\beta}p^2 \tag{1.14}$$

where V_a and $c\beta$ are the velocities of the fluid elements (Alfvén velocity) and particles, and λ is the mean free path against collisions with the fluid elements. The Alfvén velocity represents the velocity by which a perturbation in the magnetic field is propagates along the magnetic field lines. Expressing the (spatial) diffusion coefficient as $D = \frac{1}{3}\lambda\beta c$, a relation between D and D_{pp} can be established:

$$D_{pp} = \frac{V_a^2 p^2}{9D} \tag{1.15}$$

1.2.4 Weighted Slab Model

The principal idea of the weighted slab model is to choose a geometry for the Galaxy and to replace the time and space dependence of the fluxes in terms of matter thickness traversed [26, 27]. It is convenient to introduce the column density of matter traversed by the particle $x = \rho \cdot l$ (*grammage*), expressed in $g \cdot cm^2$. Nuclei of

the same species with a given energy do not have necessarily the same propagation history, so that a probability distribution of grammage is associated with all the species. The function $G(x)$, called *path length distribution*, is then introduced. $G(x)$ is the probability that a nucleus j has crossed the grammage x. The corresponding density N_j is given by:

$$N_j = \int_0^\infty \tilde{N}_j(x) \cdot G(x) \cdot dx \tag{1.16}$$

where the unweighted functions $\tilde{N}_j$ are the cosmic-ray densities after traversing a matter slab of thickness x. Since the grammage is directly related to the destruction rate and corresponding cross sections (total σ_j and partials σ_{kj}), the $\tilde{N}_j$ can be simply determined from equations:

$$\frac{d\tilde{N}_j}{dx} = \frac{1}{\overline{m}} \left[\sum_{k>j} (\sigma_{k\to j} N_k) - \sigma j \right] \tag{1.17}$$

where $\overline{m}$ is the average ISM mass, and the initial condition $\tilde{N}_j(0) = Q_j(E)$ must be imposed.

In WSM framework the $G(x)$ function are derived empirically in order to account for the data, and all information on the CR propagation have then to be inferred in terms of grammage. The $G(x)$ can also be determined by the choice of a propagation model. In this sense, the WSM represents a general technique more than model. Indeed the grammage can be used in any propagation equation (DHM, LBM) [28]. For instance, inserting Eq.1.16 into Eq.1.7 leads to:

$$n\beta c \frac{\partial G}{\partial x} - \nabla \cdot (D \nabla G) = f(\mathbf{r}, t) \cdot \delta(x) \tag{1.18}$$

which describes the propagation for point-like sources $\delta(x)$ spatially distributed according to $f(\mathbf{r}, t)$ (convection and energy losses are neglected here). The CR densities N_j are then given by Eq.1.16, more precisely:

$$N_j(\mathbf{r}) = \int_0^\infty \tilde{N}_j(x) \cdot G(\mathbf{r}, x) \cdot dx \tag{1.19}$$

where the separation between the *nuclear* part $N_j(x)$ and the *astrophysical* part $G(\mathbf{r}, x)$ is apparent. This model is quite satisfactory in the high-energy limit and for a particle-independent diffusion coefficient, where it becomes equivalent to the direct solution of the diffusion equation 1.7. It is also easy adaptable for every geometrical model of the Galaxy and for all spatial source distributions. The WLB allows to link LBMs with more realistic descriptions, explaining why LBM works so well.

1.2.5 Leaky Box Model

The Leaky Box Model, introduced in the sixties and today still largely used, can be viewed as a further simplified version of the WSM, i.e. an extremely simplified version of the diffusion model [29]. The basic assumption is that diffusion takes places rather rapidly. The distribution of cosmic rays in the whole box (i.e. Galaxy) is homogeneous; they are free to propagate in the Galaxy with a certain escape time of CRs from the system. Starting from the WSM formulation (Eq.1.18), it consists in the substitutions:

$$\nabla \cdot (D \nabla N_j) \longleftrightarrow \frac{N_j}{\tau_{esc}} \tag{1.20}$$

where τ_{esc} is the escape time of cosmic rays from the Galaxy, and with the average of every quantities (e.g. $n \leftrightarrow \overline{n}$). The result is the basic LBM equation:

$$\frac{\partial N_j}{\partial t} = Q_j - \frac{N_j}{\tau_{esc}} - \overline{n}\beta c \sigma_j N_j + \sum_{k>j} [\overline{n}\beta c \sigma_{k\to j} N_j] \tag{1.21}$$

The characteristic escape time τ_{esc} is to be determined experimentally and is a purely phenomenological quantity. In this model, other energy changing processes and convection are neglected. The physical interpretation of the LBM is that cosmic rays move freely in a containment volume, with a constant probability per time unit $P = \tau_{esc}^{-1}$. The number of escaped particles per unit time is the proportional to the number of particles present in the *box*. The other processes (decays, break up and spallation) may also be viewed in terms of characteristic times:

$$\begin{aligned} \tau_{int}^{j} &= \overline{n} \cdot \beta c \cdot \sigma_j \\ \tau_{int}^{k\to j} &= \overline{n} \cdot \beta c \cdot \sigma_{k\to j} \end{aligned} \tag{1.22}$$

For steady-state solutions $\frac{dN_j}{dt} = 0$, the resulting system of equations for the various kind of nuclei j are purely algebraic:

$$\frac{N_j}{\tau_{esc}} + \frac{N_j}{\tau_{int}^{j}} = Q_j + \sum_{k>j} \frac{N_k}{\tau_{int}^{k\to j}} \tag{1.23}$$

The characteristic time τ_{esc} is often replaced by λ_{esc}, which characterizes the amount of matter traversed by the CRs before escaping from the ISM:

$$\lambda_{esc} = \overline{m} \cdot \overline{n} \cdot \beta c \cdot \tau_{esc} \tag{1.24}$$

where $\overline{n}$ refers to the mean interstellar gas density through which the particles penetrate, $\overline{m}$ means the mean mass of the gas, and βc is the velocity of the particle. Analogous substitutions can be done for τ_{int}^{j} and $\tau_{int}^{k\to j}$, providing the mean interaction lengths for decay or break up λ_{int}^{j} and fragmentation λ_{int}^{kj}. As these latter

processes are obviously particle-dependent, it should be noted that the escape time or length is the same for all the nuclear species, i.e. this formulation assumes that all nuclei have the same propagation history.

Clearly this model is only an approximation which does not give indications of the main physical processes. Despite the simplicity of its physical framework, the LBM permits a direct analysis of flux measurements in function of only three fundamental parameters: the escape time, the mean matter density and the abundance sources. This is largely sufficient for many purposes, because it reproduces very well the main observed features of secondary to primary CR ratios.

1.3 Cosmic Rays Near Earth

At the final stages of their travel toward the Earth, cosmic rays are influenced by two local phenomena: the solar wind, which composes the heliosphere and extends up to the boundaries of the solar system, and the geomagnetic field, which composes the Earth magnetosphere. Both the effects produce a distortion of the interstellar spectra measured at Earth.
Two different approaches are traditionally followed by the CR physics community for the two phenomena.

The solar wind influence on CRs, which is still poorly understood, is studied by the theoretical community as well as other propagation aspects, i.e. the experimental measurements are usually presented uncorrected for this effect. Thus, low energy measurements are not representative of interstellar flux, and, since the solar wind varies with a 11-year timescale, experimental data coming from different epochs are not directly comparable unless solar modulation is accounted.
On the contrary, the geomagnetic modulation is considered as part of the experimental conditions: to take into account this effect is responsibility of experimentalists. Measured fluxes must therefore be corrected in order to quote the geomagnetically demodulated spectra.

1.3.1 Propagation in the Heliosphere

The energy spectrum of CRs in the solar system is modulated for energies up to several GeV/n. This is due to a phenomenon called the solar wind, a magnetized plasma in hydrodynamic expansion. In fact a fully ionized gas, basically constituted of low energy electrons and protons ($E \sim 0.5\ MeV$) is pushed radially out of the Sun's corona. Once the plasma has left the corona, the dynamic pressure of this wind dominates over the magnetic pressure through most of the solar system, so

that the magnetic field lines are driven out by the plasma. The combination of the outflowing particles motion with the Sun's rotation leads to an Archimedean spiral pattern for the flow. The region of space in which the solar wind is dominant is called heliosphere. The charged particles that penetrate the heliosphere are diffused

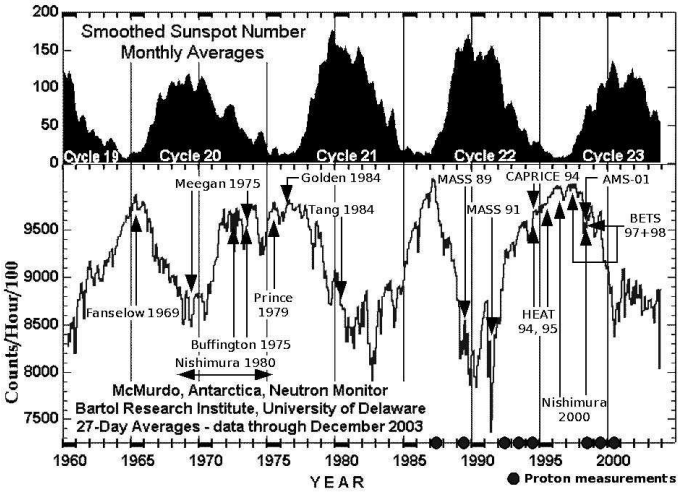

Figure 1.6: Cosmic-ray intensity variation (neutron counts) and their anti-correlation with the 11-year sunspot cycle. Low galactic CR intensity reaches the earth during periods with high solar activity and vice versa.

and energetically influenced by the expanding solar wind. As this effect involves all the cosmic rays that we detect at Earth (or in near space), it must be taken into account for interpretation of the measured spectra.

The modulation of galactic cosmic rays in the interplanetary medium can be discussed in terms of a spherically symmetric model in which particles undergo convection, diffusion and energy changes resulting from the expansion of the solar wind as a function of the radial distance r from the Sun. One method is the force field approximation, which consists in viewing the solar wind as a radial field with a potential ϕ [3, 30]. In this approximation the equation of density evolution is

$$\kappa \frac{\partial N}{\partial r} + \frac{V}{3}\left[T^2 - (mc^2)^2\right]^{3/2} \frac{\partial N}{\partial T}\left[\frac{N}{T\left[T^2 - (mc^2)^2\right]^{1/2}}\right] = 0 \qquad (1.25)$$

where $N(r,T)$ is the differential density, $V(r,T)$ is the solar wind speed, κ the diffusion coefficient, assumed to be constant, T the kinetic energy and m the particle mass. This equation can be integrated with the appropriate boundary conditions.

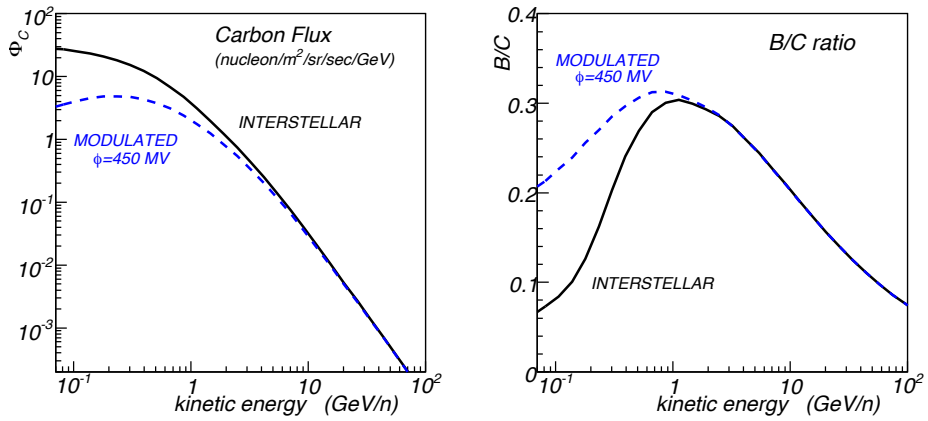

Figure 1.7: Left: Solar Modulation for Carbon energy spectrum. The effect is qualitatively similar for all the CR species, but its strength is charge-dependent. Right: the effect of the solar activity on the B/C ratio. The interstellar spectra are computed with `GchALPROP` [20] (see also §4.9). The solar modulation has been applied as discussed in the text.

Then, the cosmic ray flux $\Phi = \frac{\nu}{4\pi} N(E)$ can be expressed as follows:

$$\Phi_{\odot}(E) = \frac{E^2 - m^2c^4}{(E + Ze\phi)^2 - m^2c^4} \Phi_{IS}(E + Ze\phi) \tag{1.26}$$

In Eq.1.26 the differential particle intensity $\Phi_{\odot}$ at energy E in the heliosphere is related to the the *interstellar* differential intensity Φ_{IS}, i.e. beyond the termination of the solar wind. The proportionality factor between $\Phi_{\odot}$ and Φ_{IS} is the ratio of the two corresponding squared momenta $p^2_{\odot}/p^2_{IS}$. The modulation parameter ϕ is used to interpret the energy loss experienced by the particle when approaching the earth from the infinity:

$$\phi = \int_r^{\infty} \frac{V}{3\kappa} dr \tag{1.27}$$

The characteristic energy loss of a charge Z particle in the heliosphere is $\Delta E = Ze\phi$. The solar modulation parameter is indeed used to specify the level of solar activity which affects a specific measured differential CR intensity.
To produce diagrams of solar cycle activity like in Fig.1.6, the observation of the number of sunspots together with a neutron monitor technique are used. Variation of intensity in the interplanetary CR spectrum is anti-correlated with the number of sunspots. The effect of the modulation in the Carbon energy spectrum and in the B/C ratio is shown in Fig.1.7, where the interstellar energy spectra (black solid lines) are shown together with the corresponding solar-modulated (blue dashed lines) assuming $\phi = 450\ GV$, which is consistent with the period of AMS-01 flight (June 1998).

1.3.2 The Earth Magnetic Field

The last obstacle for cosmic rays before being detected by an Earth orbiting detector is the GeoMagnetic Field (GMF), that extends its influence on the cosmic radiation modulating the low-energy part of the observed spectra ($\lessapprox 10\ GeV/n$).

In first approximation, the GMF can be represented as an offset and tilted dipole field with moment $M = 8.1 \cdot 10^{25}\ G\ cm^3$, an inclination of 11° to the axis of Earth rotation and a displacement of about 400 km with respect to the Earth center. Because of the tilt and offset, the GMF is characterized by distortion, the highest of which is in the South Atlantic, where the field strength is the weakest. The charged particles penetrate deeper in this region and the radiation becomes stronger. This high radiation phenomenon is the so-called *South Atlantic Anomaly* (SAA).

The most important aspect for CR measurements is the determination of the *geomagnetic cut-off* [31]. Charged particles traversing the magnetic field experience the Lorentz force that produces a curved path for low rigidity particles. Cosmic rays can thus be prevented form reaching the detector, depending on their rigidity and incoming direction [32].
For a CR particle directed toward the Earth, the screening is determined by its rigidity, the detector location in the GMF and its incoming direction with respect to the field. Conversely, for given arrival direction and location, there will exist a minimum value of the particle rigidity R_C for which galactic CRs are allowed to penetrate the magnetosphere and be detected. In the dipole approximation, the rigidity cut-off R_C was analytically evaluated by Störmer [33, 34] that found the relation:

$$R_C = \frac{M \cos^4 \lambda}{\mathcal{R}^2 \left[1 + (1 \pm cos^3\lambda \cos\phi \sin\xi)^{1/2}\right]^2} \tag{1.28}$$

where M is the dipole moment. The arrival direction is defined by ξ and ϕ, respectively the polar angle from local zenith and the azimuthal angle counted clockwise form local magnetic East. The $\pm$ sign applies to negatively/positively charged particles. The arrival location is defined by the *geomagnetic coordinates* $(\mathcal{R}, \lambda)$, a commonly used coordinate system relative to the dipole axis. $\mathcal{R}$ is the distance from the dipole center, usually expressed in Earth radii units ($\mathcal{R} = r/R_\oplus$), and λ is the latitude along the dipole. These quantities come from the simple dipole field description, where the components of the field are:

$$B_r = -\frac{M}{r^3} 2 \sin\lambda \qquad B_\lambda = \frac{M}{r^3} \cos\lambda \tag{1.29}$$

and the field lines have the form $r \propto \cos^2\lambda$. For vertical incidence ($\xi = 0$) the azimuthal dependence of the cut-off simply vanished, putting in evidence the cutoff

behaviour as a function of the geomagnetic latitude:

$$R_{VC} = \frac{M}{4\mathcal{R}^2}\cos^4\lambda \equiv \frac{M_0}{\mathcal{R}^2}\cos^4\lambda \tag{1.30}$$

where $M_0 = 15$ if R_{VC} is measured in GV. The cut-off is maximum at the geomagnetic equator, with a value of approximately 15 GV, and vanishes at the poles.

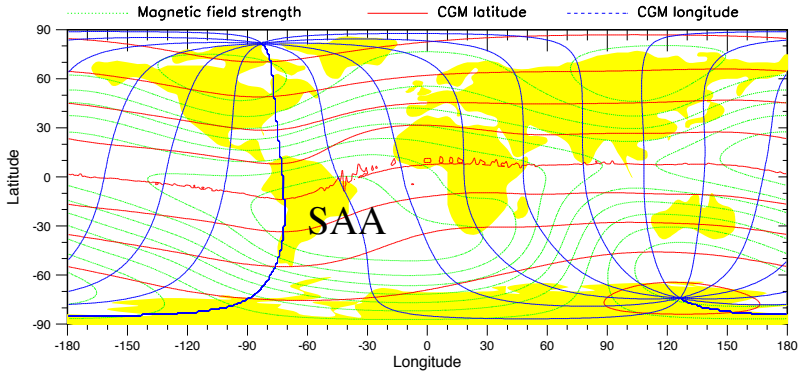

Figure 1.8: The CGM coordinate grid projected onto the geodetic map. The green contour lines are the magnetic field strength at the Earth surface. The red (blue) lines are the magnetic latitude (longitude). The SAA region is marked in this figure.

A more precise description of the cut-off can be obtained by replacing the dipole coordinates with the *Corrected GeoMagnetic* coordinates (CGM). The method consists in defining an opportune transformation $GM \leftrightarrow CGM$ that maps a more realistic GMF model into the dipole representation [35]. The most commonly used GMF model is the IGRF one. In this picture, a rather complex magnetic field $\mathbf{B}$ is treated as the derivative of a scalar potential V, $\mathbf{B} = -\nabla V$, with V expressed by a series of spherical harmonics [36]:

$$V = R_\oplus \sum_{n=0}^{\infty}\left(\frac{R_\oplus}{r}\right)^{n+1}\sum_{m=0}^{n} P_n^m(\cos\theta)\,(g_n^m\cos m\psi + h_n^m \sin m\psi) \tag{1.31}$$

where $R_\oplus$ is the mean earth radius 6321.2 km, r is the geocentric radius, θ is the geographic colatitude and ψ is the East longitude from Greenwich. $P_n^m(\cos\theta)$ are the Legendre polynomial functions, g_n^m and h_n^m are the Gaussian coefficients that specify the GMF, determined experimentally. The IGRF model is widely used in geophysics and contains coefficients up to order 12. The dominant terms in Eq.1.31 are related to $n = 1$ that leads to the simple dipole field.

The corresponding CGM coordinates are illustrated in Fig.1.8. This procedure allows to use the Störmer formulae Eq.1.28 and Eq.1.30 in a IGRF framework, and has been adopted in this thesis to estimate the effective exposure time of AMS-01 on Shuttle to galactic cosmic rays (§3.3 and §5.3).

1.4 The B/C Physics

The B/C physics is the physics of the *secondary-to-primary* cosmic rays. The *primary* galactic CR nuclei are those produced and accelerated at astrophysical sources. Their energy spectra and chemical composition are modified from the sources to the Earth by spallation processes on the ISM, producing *secondary* cosmic rays. Electrons and Protons, as well as Helium, Carbon, Oxygen, Iron and all the nuclei synthesized in stars are mainly primaries. Nuclei such as Lithium, Beryllium, Boron and the sub-Iron group (which are not abundant end-products of stellar nucleosynthesis) are typically of secondary origin.

Knowing the relative abundances of the various kinds of primary and secondary nuclei, fundamental parameters of the propagation models can be determined, such as the escape time (in LBM), or the mean traversed matter (WSM) or the diffusion coefficient (DHM).

1.4.1 B/C Models

The Boron-to-Carbon ratio is considered one of the most important observables to study propagation parameters. It is very instructive to consider the case of B/C ratio in the LBM framework. Boron is a purely secondary CR species, mostly produced by interaction of Carbon nuclei in the ISM. The Leaky Box equation for the Boron nuclei is then given by:

$$\frac{\partial N_B}{\partial t} = -\frac{N_B}{\tau_{esc}} - \frac{N_B}{\tau_{int}^B} + \frac{N_C}{\tau_{int}^{CB}} \tag{1.32}$$

In this description there is no primary source Q_B for Boron. The Boron escaping rate N_B/τ_B is balanced by its production through Carbon spallation on the ISM:

$$C + ISM \longrightarrow B + X \tag{1.33}$$

that occurs with characteristic time τ_{int}^{CB}. The steady-state solution leads to the ratio B/C:

$$N_B/N_C = \frac{\tau_{esc}/\tau_{int}^{CB}}{1 + \tau_{esc}/\tau_{int}^{B}} \tag{1.34}$$

where $\tau_{int} = (\overline{n} \cdot \beta c \cdot \sigma_{int})^{-1}$ are the characteristic interaction times for Carbon spallation (into Boron) and Boron destruction. The N_B/N_C ratio is therefore sensitive to the characteristic propagation time and the amount of matter traversed by CRs before the leakage. The relation is apparent if one expressed the formula in terms of escape and interaction path lengths (1.24) and neglects the boron destruction rate ($\lambda^B_{int} \gg \lambda_{esc}$): the ratio becomes $N_B/N_C \approx \lambda_{esc}/\lambda^{CB}_{int}$, where $\lambda^{CB}_{int} = \overline{m}/\sigma_{CB}$. Essentially, in the simplest LBM model, the B/C ratio determines the characteristic propagation length traversed by CRs before escaping from the Galaxy. For instance, using $\sigma_{CB} \approx 40\ mb$ and $\overline{m} \approx M_p$, for $B/C \approx 0.3$, a rough estimation of λ_{esc} is $\sim 10\ g/cm^2$.
This escape time (length) is in general energy-dependent, and expresses the relation between the source energy distribution $Q_C(E)$ and the observed one $N_C(E)$. Indeed the LB equation for Carbon leads to the stationary solution:

$$N_C(E) = \frac{\tau_{esc}}{1 + \tau_{esc}/\tau^C_{int}} Q_C(E) \tag{1.35}$$

Thus, information on the primary sources spectra and composition can be inferred directly through the B/C ratio.

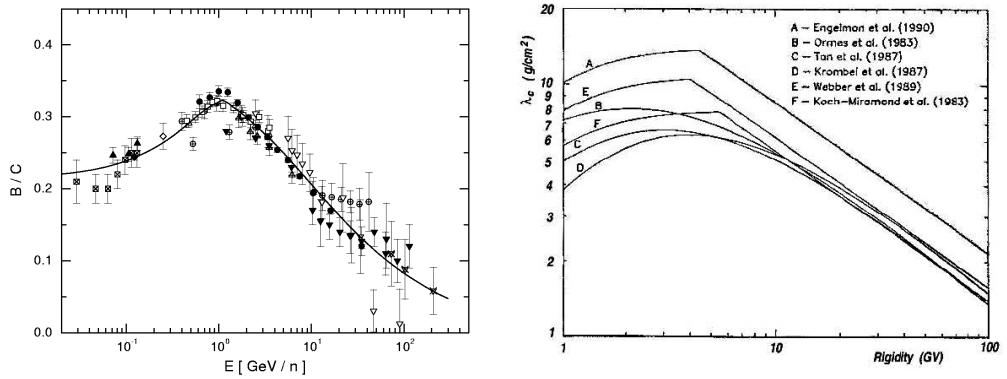

Figure 1.9: Left: collection of measured B/C ratios at different energies (references are in Tab.1.4.2). The fitted curve determines the λ_{esc} dependence, in the LBM, according to Eq.1.36 [37]. Right: rigidity dependence for λ_{esc} as proposed by different authors [38, 39, 40, 41, 42, 43].

Fig.1.9 shows, as an example, the fit to measured B/C ratio assuming a broken power-law in rigidity for the escape time τ_{esc} [37]. The escape length is written as:

$$\lambda_{esc}(R) = \begin{cases} \lambda_0 \beta \left(\frac{R}{R_0}\right)^{+0.8} & \text{for } R < R_0\ GV \\ \lambda_0 \beta \left(\frac{R}{R_0}\right)^{-0.57} & \text{for } R > R_0\ GV \end{cases} \tag{1.36}$$

where $\lambda_0 = 12.8\ g/cm^2$, and $R_0 = 4.7\ GV$. Similar calculations have been done by many authors (Fig.1.9, right). Working out the proper energy or rigidity dependence of λ_{esc} is a fundamental test for any propagation model.
It is clear from Fig.1.9 that the B/C typically peaks at some GeV/n and falls off to higher and lower energies. These result tells that the CR particles should traverse about $\sim 10\ g/cm^2$ interstellar matter before escaping from the confinement volume. A plausible physical reason for this characteristic shape, i.e. the power-law dependence and the breaking at R_0, does not exist in the LBM context, as the λ_{esc} is used as a pure phenomenological parameter.
However it can be understood if one notices the link between the leaky-box calculations and the diffusion halo models [19]. In DHM framework, the mean time τ_{esc} which a particle needs to escape freely into the intergalactic space is given by:

$$\tau_{esc} = \frac{H^2}{2D} \tag{1.37}$$

being H the halo size and D the diffusion coefficient. The theory of particle resonant scattering and diffusion in the turbulent and magnetized interstellar medium predicts a rigidity scaling law for $D(R)$ [6]:

$$D = D_0 \beta R^{\delta} \tag{1.38}$$

where D_0 is the normalization of the diffusion coefficient, linked to the level of the hydromagnetic turbulence and is generally expressed in $cm^2 \cdot s^{-1}$. The diffusion coefficient has a power-law dependence on the rigidity R with a spectral index δ which is linked to the density of the magnetic irregularities at different wavelengths. Since this is not strictly true, as reacceleration occurs whenever we have diffusion, the LB breaking at R_0 simulates the reacceleration in the halo. Following this last observation one can argue that the path length λ_{esc} suggests a way to reproduce B/C for the models in which reacceleration is completely absent. Another possible physical explanation is given in [44], by saying that below a particular rigidity R_0 the diffusion becomes slower than the convective transport in removing particles from the galaxy and the particle residence time becomes independent of rigidity or at least weakly dependent. The problem is therefore still open. However, many physical interpretations of the B/C ratio can be naturally given in the framework of the diffusion models, without invoking any artificial breaking.

At higher energies ($E > 10\ GeV/n$), δ is the parameter that mostly determine the B/C shape, as in the high energy limit the secondary-to-primary in DHM is dominated by the diffusion coefficient. At lower energies, the effect of energy losses, convection and halo size and spallation become more important in shaping the B/C ratio [21, 22].

The Kolmogorov theory for the turbulent spectrum predicts $\delta = 1/3$, while, in the case of a hydromagnetic spectrum, it has been predicted by Kraichnan as $\delta = 1/2$ [45]. On the other side, the phenomenological interpretation of CR spectra have not led to fix δ because of the complicated treatment of the physical phenomena at different energies. Moreover, existing data on the B/C ratio suggests higher values for δ $(0.4 \div 0.8)$.
At energies around 1 GeV/n lower $\delta = 1/3$ seems to be favored, but at this energies the CR spectra are strongly affected by other low-energy phenomena. Diffusive reacceleration contributes significantly in shaping the B/C ratio below few GeV/n. In this energy region the measured fluxes are also affected by solar modulation (Fig.1.7), which makes difficult to compare experimental data taken in different periods of solar activity.

Another possible effect that might be investigated with high energy B/C data is distributed reacceleration [46] i.e. sporadic encounters of CR particles with SNRs, during which they could gain small amount of energies. Time-dependent models have also been studied [47], considering SNs as discrete sources in the Galaxy. This scenario does not seem to modify the B/C ratio in shape, but only in an overall normalization factor.

However, in DHM as in LBM framework, the B/C ratio is a good test for propagation parameters through a fit of the spectral index δ. It is also clear that a precise measurement of the B/C on a large energy range will shed light on many aspects of the Galaxy properties.

1.4.2 B/C Experimental Data

Starting in the sixties, the CR chemical composition has been extensively studied in balloon-borne experiments (Tab.1.4.2).
The characteristic of CR nuclei is the low intensity. Therefore accurate measurements require large acceptances, long exposure times and optimal particle discrimination capabilities [48]. In spite of the large number of balloon experiments, the more precise and reliable measurements come from two space borne detectors: C2 onboard HEAO-3 [38] and CNR onboard the SpaceLab-2 mission [50]. C2 measured fluxes from Be up to Ni in the energy range 0.6 to 35 GeV/n using multiple layers of Čerenkov counters with different materials. The measurements have been extended by CRN up to TeV/n with TRD detectors. The new generation of experiments is devoted to extend the measured range up to the knee, following the road open by the JACEE collaboration [51], a series of balloon-borne lead emulsion chambers.

Instruments as TRACER [49], CREAM [52] and ATIC [53] are designed to provide

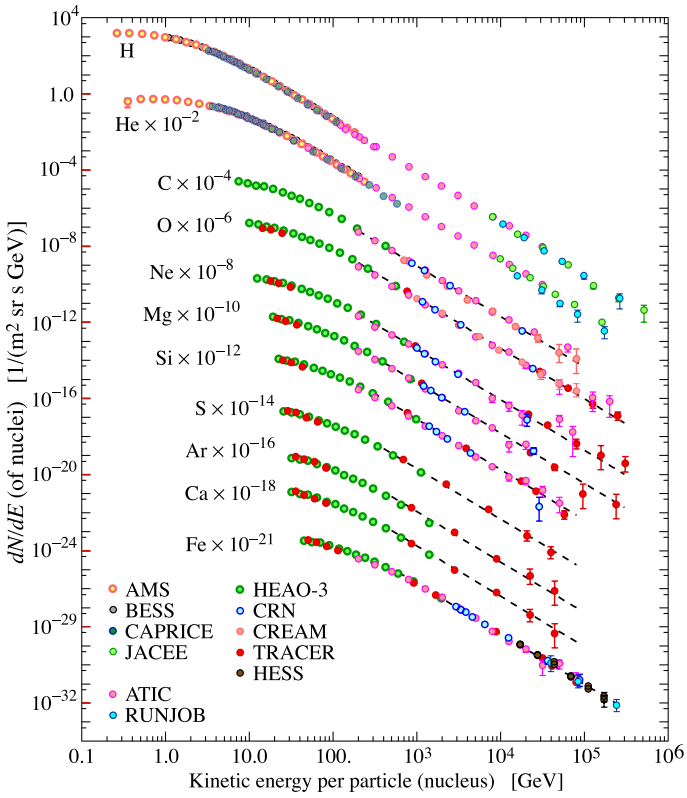

Figure 1.10: Differential energy spectra for the major component of the primary cosmic radiation. The dashed lines represent independent power-law fits to the spectra performed above 20 GeV/n [49, 5].

differential flux measurements of different CR species at energies between $\sim GeV/n$ and many TeV/n, by using different detectors, as calorimeters in ATIC, TRD detectors in TRACER or both in CREAM. All these new instruments are profiting of long duration balloon flights provided by the NASA Ultra Long Duration Balloon program in Antarctica.

On the other side, space borne experiments using spectrometric technologies have the capabilities to measure CR nuclei flux up to some TeV/n with large exposure factors. AMS-01 is an instrument of this type (§2). The magnetic spectrometer PAMELA was launched in June 2006 with the RESURS DK1 satellite. PAMELA is currently operational on DK1 along an elliptical orbit with inclination of 70°. The PAMELA concept is very similar to AMS. The spectrometer is based on a double-sided micro-strip silicon tracker located into a permanent magnet. A Si-W imaging calorimeter and a neutron monitor are used to distinguish primary protons and electrons. A Time-of-Flight system, using plastic scintillation detectors, measures

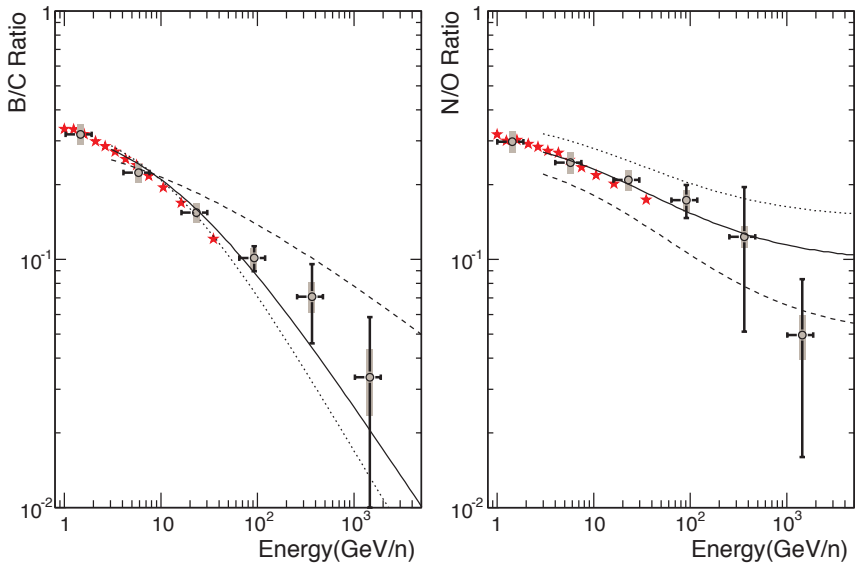

Figure 1.11: Measurements of the ratios B/C (right) and N/O (left) as a function of energy. Open circles show the nuclear ratios measured by CREAM experiment [52]. The thin vertical bars correspond to the statistical errors and the gray bars show the systematic uncertainties. The stars are data from HEAO3-C2 experiment [38]. In the B/C, the lines represent model calculations for various values of the rigidity dependence parameter $\delta = 0.33$ (long-dashed line), $\delta = 0.6$ (solid line) and $\delta = 0.7$ (short-dashed line).

velocity and charge of incident particles. Charge separation up to Oxygen is achievable by means of energy loss measurement in the Tracker, TOF and Calorimeter. A compilation of flux measurements is shown in Fig.1.10 for the major nuclear components of the CR radiation. The measurements performed so far are summarized in Tab.1.4.2. For a complete collection the reader is addressed to [56]. Fig.1.11 shows two recent measurements of the B/C and N/O ratios as a function of energies up to 2 TeV/n performed by CREAM collaboration [52].

Measurement	**Date**	**Experimental Method**	**Carrier**	**Z**	**E (GeV/n)**	**Exp** (m^2srh)
Juliusson et al. [57]	1971	Čerenkov Counters	Balloon	$3 \div 28$	20–120	7.6
Orth et al. [58]	1972	Magnetic Spectrometer	Balloon	$3 \div 26$	2–150	1.15
Maehl et al. [59]	1973	Čerenkov Counters	Balloon	$5 \div 26$	0.32–2.20	2.4
Caldwell et al. [60]	1974	Čerenkov Counters	Balloon	$5 \div 28$	5–90	4.5
Lezniak et al. [61]	1974	Čerenkov Counters	Balloon	$3 \div 28$	0.3–50	23.
Simon et al. [62]	1976	Ionization Cal.	Balloon	$5 \div 26$	2–100	15.5
Voyager 1 & 2 [63, 64]	1977–now	Solid-State Detector	Spacecraft	$1 \div 28$	0.001–0.500	—
Dwyer et al. [65]	1978	Čerenkov and MWPC	Balloon	$5 \div 28$	1–10	38.
JACEE [51]	1979–95	Emulsions Cal.	Balloon	$1 \div 26$	1000–10^6	1432.
C2 on HEAO-3 [38]	1979–80	Čerenkov Counters	Satellite	$4 \div 28$	0.6–35	430.
CRN [50]	1985	TRD and Čerenkov	Shuttle	$6 \div 27$	50–1500	70.
Buckley et al. [66]	1991	RICH	Balloon	$2 \div 8$	40–320	1.4
RUNJOB [67]	1995–97	Emulsions Cal.	Balloon	$1 \div 26$	10^4–10^6	1000.
TIGER [68]	1997	Čerenkov Counters	LDB	$26 \div 40$	0.8–5	—
ATIC [53]	2002	Si Matrix & Cal	ULDB	$5 \div 8$	10–300	300.
CREAM I [52]	2004–05	Čerenkov, TRD & Cal.	Balloon	$1 \div 26$	10–2·10^3	232
TRACER [49]	2003	TRD & Prop. Tube	LDB	$8 \div 26$	1–10^4	100.

Table 1.1: Summary table of the principal experiments devoted to nuclear composition measurements of CRs. Exposure factors in the last columns are expressed in units of $m^2 \cdot sr \cdot h$. Only measurements of published results are reported. For CREAM and TRACER projects, other flights are done or to be done. Other results are forthcoming from CREAM, TRACER, PAMELA.

1.5 Discussion

Cosmic-ray nuclei are a powerful tool for understanding the characteristic of the CR acceleration and propagation, as well as the physical properties of the interstellar medium. Present observations and those coming in the near future will yield more valuable information about the matter content and dynamical property of our Galaxy. A better understanding of the processes by which cosmic rays are produced, accelerated and propagated in the ISM would even allow to discover some evidence for new physics or exotic sources, as fundamental astrophysical processes constitute a background for the search of anomalous components.

Many consistent frameworks to describe the propagation of CR nuclei have been formulated in order to explain the available data. Theoretical studies of CR physics are currently stressing to correlate measured fluxes to the diffusion parameters: the spectral index of sources α, the normalization D_0, the spectral index of the diffusion coefficient δ, the height of the diffusive halo H, the galactic wind speed V_C and the Alfvén speed V_A.

Different classes of experimental channels may be indicators of some dominant physical phenomenon and be particularly sensitive to the corresponding propagation parameters. One of the most sensitive quantity is the B/C ratio, as B is purely secondary and its main progenitor C is purely primary.
Moreover, it is also a quantity measurable with reasonable accuracy within the various nuclear component of the cosmic rays, due to the relatively large abundance of the two species and other experimental benefits. Indeed, as a ratio of two nuclei with similar Z, the B/C is less sensitive to systematic errors and to solar modulation effects than absolute fluxes or other ratios of nuclei with more distant charges.
On the other side, existing data are still affected by sizable experimental errors, and propagation models still do not have a definitive standard picture. Comparisons of predictions between different authors should be taken with care. From the experimental point of view, it is a very exciting epoch for cosmic rays, as much data are expected soon from the most recent projects PAMELA, CREAM, TRACER, and the upcoming AMS-02 magnetic spectrometer.
Current and upcoming experiments such as PAMELA and AMS-02 are therefore a strong motivation for further elaborations.

Chapter 2

The AMS-01 Experiment

The Alpha Magnetic Spectrometer (AMS) is a high energy physics experiment operating in space. The experiment has been proposed and approved by institutes and space agencies in many countries. Italy, Swiss, Germany, Spain, France, Portugal, Denmark, China, Taiwan, South Korea, Russia, USA, Mexico, Romania, Finland and Netherlands are currently taking part in the AMS collaboration. The final version AMS-02, is scheduled for installation on the International Space Station (ISS) for an at least three year long exposure [69]. The reduced version, AMS-01, flew for ten days in a precursor mission in June 1998 on board the NASA space Shuttle Discovery [70]. The analysis presented in this thesis is based on the data collected during this flight.

The aim of this chapter is to present the AMS concept. Section §2.1 outlines the physics goals of the experiment. Sections §2.2, §2.4.1 and §2.4.2 describe the AMS-01 detector, the reconstruction algorithm and the simulation program. The AMS-01 flight is described in Section §2.5, while the main physics results from the STS-91 mission are summarized in Section §2.6.

2.1 AMS Physics goals

The main goal of the AMS experiment is to search for antimatter of primordial origin looking for the presence of anti-nuclei ($Z \leq -2$) in the cosmic rays. Experimental evidences indicate so far that our galaxy is made of matter. However, there are more than hundred million galaxies in the Universe and the Big Bang theory of the origin of the universe requires equal amounts of matter and antimatter. Theories that explain this apparent asymmetry violate other measurements. Whether or not there is significant antimatter is one of the fundamental questions on the origin and nature of the universe. The detection of even a single anti-nucleus in the cosmic

radiation, as a nucleus of $\overline{\text{He}}$, would provide evidence for the existence of antimatter domains, since the probability of a spallation production of $\overline{\text{He}}$ is extremely low [71].

Another interesting discover potential for AMS concerns the indirect dark matter detection. The visible matter in the universe, such as stars, adds up to less than 5% of the total mass that is known to exist from many other observations. The other 95% of matter is dark, either *dark matter*, which is estimated at ∼20% of the energy balance of the universe; the remaining part is made up by dark energy. The exact nature of both still is unknown. One of the leading candidates for dark matter is the neutralino. If neutralinos exist, they could be annihilating with each other and giving off an excess of standard[1] charged particles that can be detected by AMS-02 [2] Any excesses in the background positron, antiproton, or gamma ray flux could signal the presence of neutralinos or other dark matter candidates [72].
Thanks to the large acceptance, the long exposure time and the excellent particle identification capabilities, AMS can measure the spectra of the CR rare components ($\overline{p}$, e^+, $\overline{D}$, γ) with a great accuracy over a never explored energy range. In particular the positron channel is very promising as suggested by HEAT and AMS-01 experiments [73, 74] and the most recent results by Pamela, ATIC and FERMI/LAT [75, 76, 77].

The high statistics measurements of AMS-02 of all the charged species of the cosmic rays, including chemical species up to Iron and isotopes up to Carbon, will largely improve our knowledge of the cosmic rays and will help to solve several astrophysics fundamental questions (§1). The measurement of the nuclear and isotopic composition of cosmic rays can be used to validate or discard models for particle propagation in the interstellar medium.
The accurate determination of the Boron to Carbon ratio over a wider range of energies will be crucial to determine propagation parameters like the thickness of the galactic halo or the galactic wind velocity [48].
The construction, performance and qualification tests of the new AMS-02 detector are described elsewhere [78]. The AMS-01 experiment is described in detail in the following sections.

2.2 The AMS-01 Detector

The AMS-01 version of the Alpha Magnetic Spectrometer is represented in Fig.2.1. The experiment is $\sim 1.6\ m$ high and its horizontal cross section is about $2.6\ m^2$. The cylindrical permanent magnet, with a field strength along $+X$ axis of about $0.15\ T$ at the center, encloses a 6-layer micro-strip silicon tracker which measures

[1] "Standard" particles are those of the Standard Model of particle physics [5].

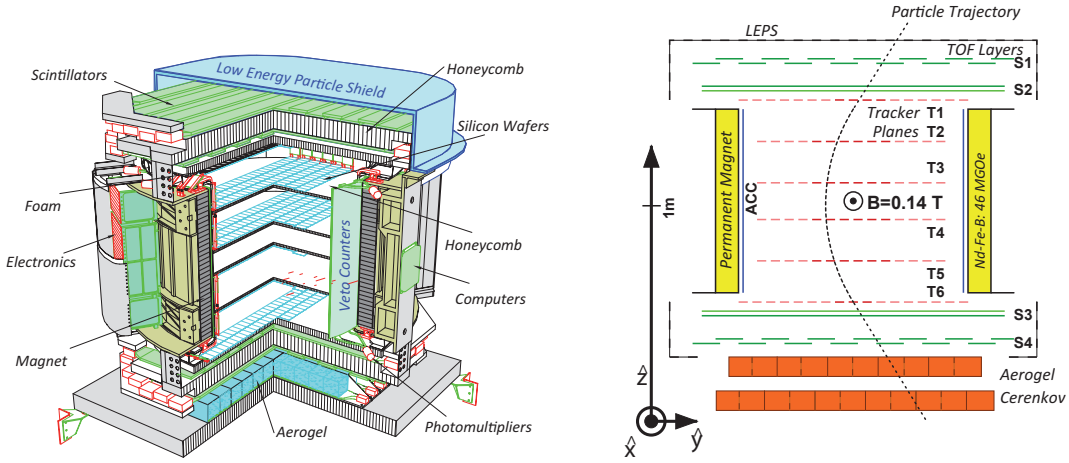

Figure 2.1: Left: iso-view of the AMS-01 spectrometer. Some construction elements such as honeycomb and foam are shown as well as the position of the electronics crates. Right: schematic view of the detector, showing the cylindrical permanent magnet, the silicon micro-strip tracker planes T1–T6, the time of flight (TOF) hodoscope layers S1–S4, the aerogel Čerenkov counter, the anti-coincidence counters (ACC) and the low energy particle shields (LEPS).

the rigidity of the charged particles traversing the volume. For the STS-91 mission the tracker was equipped with six planes of silicon sensors, resulting in a geometric acceptance of $\sim 0.3\ m^2sr$ for events with at least 4 tracker planes fired. Scintillator planes (TOF) and an Aerogel Threshold Čerenkov (ATC) counters complete the detector by measuring the particle velocity and dE/dx. A layer of Anti-Coincidence Counter (ACC) lined the inner surface of the magnet to veto triggers due to stray trajectories and background particles which may be produced by interactions in the detector material. To minimize the dead time, a Low Energy Particle Shield (LEPS) was mounted on the top to absorb the low energy particles (E<5 MeV) above the scintillator planes. The various sub-detectors, electronics devices and all the data reduction systems went through vigorous space qualification testing including acceleration, vibration, thermo-vacuum and temperature tolerance.

2.2.1 The Time Of Flight System

The TOF system provided a fast trigger signal, a measurement of the particle transit time between the scintillator planes, and the particle charge by the energy depositions. Each plane of the TOF consisted of 14 plastic scintillator (Bicron `Bc408`) paddles 1 cm thick, 11 cm width and with lengths between 71 cm and 136 cm to match the circular cross section of the AMS-01 magnet. Two planes were located above and two under the magnet. The upper part of the system is shown in Fig.2.2.

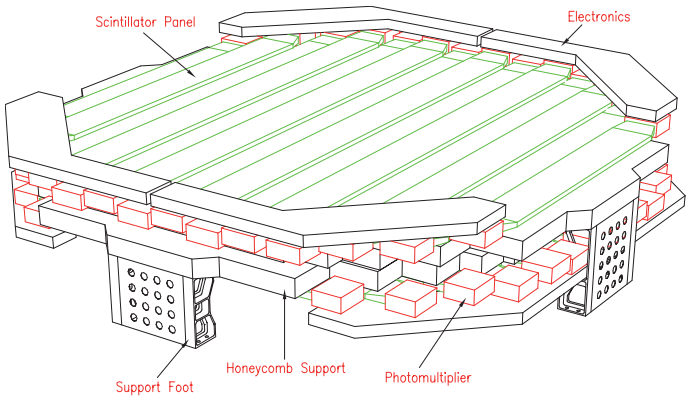

Figure 2.2: The upper two planes of the AMS-01 Time Of Flight system.

The paddles of each plane had 0.5 cm overlap to avoid geometrical efficiencies [79]. The paddles on the first (forth) plane were arrayed orthogonally to the paddles of the second (third) plane to create a matrix and allow for the identification of the particle impact point (X, Y). Each scintillator paddle was read out on the two sides by six photomultiplier tubes (PMTs), three per side. Signals from each triplet were combined in OR to from a unique readout per side. The PMTs were shielded

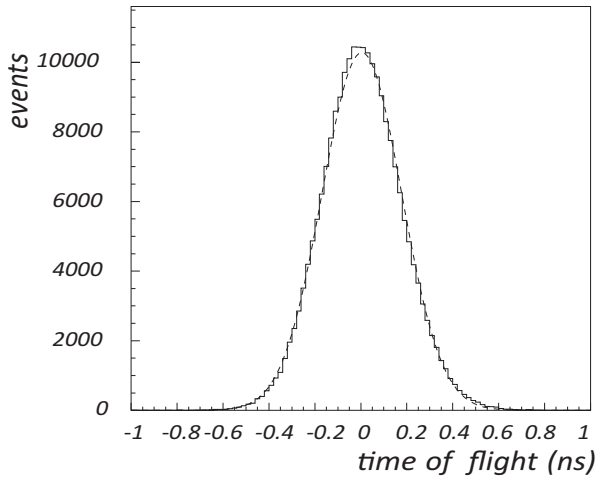

Figure 2.3: Time resolution between first and last AMS-01 TOF scintillator planes, corrected for the track length, for events taken with the AMS-01 experiment.

from the residual magnetic field ($\sim$ 200 G) by a 0.5 mm thick screen. To extend the dynamic range of the TOF system, the analog signal from both the first and the second to last dynodes were transferred to the readout electronics. The anode signals of each triplet were combined in OR and discriminated to reproduce logical

signals, sent to the fast trigger electronics (§2.3) and addressed to Time to Digital Converter (TDC) devices, which provided the time information.

2.2.2 The Magnet

The AMS-01 permanent magnet was designed to optimize the competing requirements of a large, powerful and uniform dipole magnetic field in a flight-qualified, relatively light-weighted system. The external field also needed to be minimized to

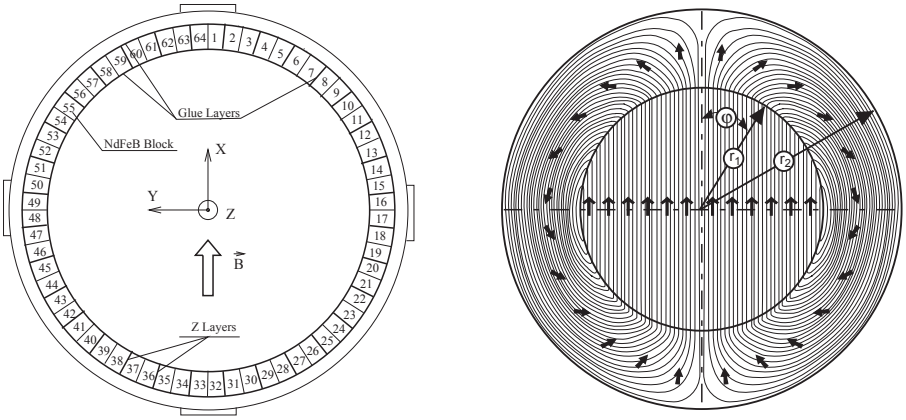

Figure 2.4: The AMS-01 magnet field orientation [70]. The varying direction of the magnetic field in the material allowed the flux to be returned primarily within the material allowing for a negligible external field. A quite uniform field is generated in the inner part of the volume. The magnet blocks and the coordinate system are shown in the left picture. The arrows in the right exhibit the magnetization direction α.

avoid torques on the space shuttle and interference with the electronic devices. The magnet was made of 6400 Nd-Fe-B blocks of sides $5 \times 5 \times 2.5\ cm^3$. The blocks were arrayed in a cylinder of length 800 mm, inner radius $r_1 = 111.5\ cm$ and outer radius $r_2 = 129.9\ cm$. The blocks were arranged to form 64 segments with varying field directions in order to produce a $0.15\ T$ field inside the volume with external residual field smaller than $2 \cdot 10^{-2}\ T$ (see Figure 2.4) [69, 70]. The magnetization vector resulting in the cylindrical shell was constant in magnitude and oriented according to:

$$\alpha = 2\phi + \pi/2 \tag{2.1}$$

being ϕ is the angular cylindrical coordinate. Such a distribution gave and internal field of:

$$B = B_r \ln(r_1/r_2) \tag{2.2}$$

where B_r is the residual magnetic flux density of the ring and r_1/r_2 is the inner/outer radii ratio. After construction the field was mapped and found to agree with the

design value to 1%. The final magnet had a maximum bending power of $BL^2 = 0.15\ Tm^2$. Its geometric acceptance was 0.82 m^2sr and its weight was 1998 Kg (2200 Kg including support structure).

2.2.3 The Silicon Microstrip Tracker

The AMS-01 silicon tracker [80, 81] was the first application in space of the high precision silicon technology developed for position measurements in accelerator experiments. The instrument, that occupied the central part of the detector, is shown

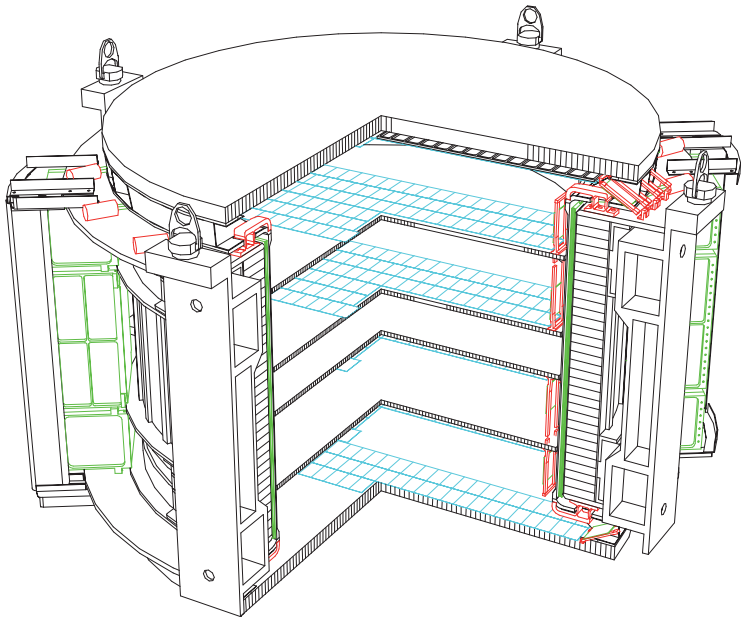

Figure 2.5: The AMS-01 silicon tracker. The six planes are equipped with silicon sensors (blue plates).

in Fig.2.5. The basic unit of the tracker was a module, called *ladder*, which consisted of 7 to 15 double-sided silicon micro-strip sensors, a Kapton routing cable and two hybrids equipped with the front-end electronics. In AMS-01, the ladders were supported by a composite structure made of low-density aluminium honeycomb and carbon fiber. This assured stability while minimizing the material inside the detector, resulting in $\sim 0.3X_0$. Each silicon micro-strip sensor had dimensions 40 $mm \times 72\ mm$ and a thickness of 300 μm. Their development was based on the design used for the L3 micro-vertex detector at the Large Electron-Positron collider (LEP) at CERN [82, 83]. Strips were implanted with a pitch of 27.5 μm on the p (junction) side and orthogonally with a pitch of 52 μm on the n (ohmic) side, so as to create a grid for measuring the two coordinates (Y, X) at the same time. Specifications are summarized in Tab.2.1. The sensor design made use of p^+ blocking

element	p-side	n-side
strip length	40 mm	72 mm
implantation pitch	27.5 μm	52 μm
readout pitch	110 μm	208 μm
n. of readout strips	640	192

Table 2.1: Specifications of the AMS-01 doubled sided silicon micro-strip sensors.

strips, implanted on the n-doped side, to minimize the influence of surface charge on the position measurement obtained from the ohmic side. Charge division readout

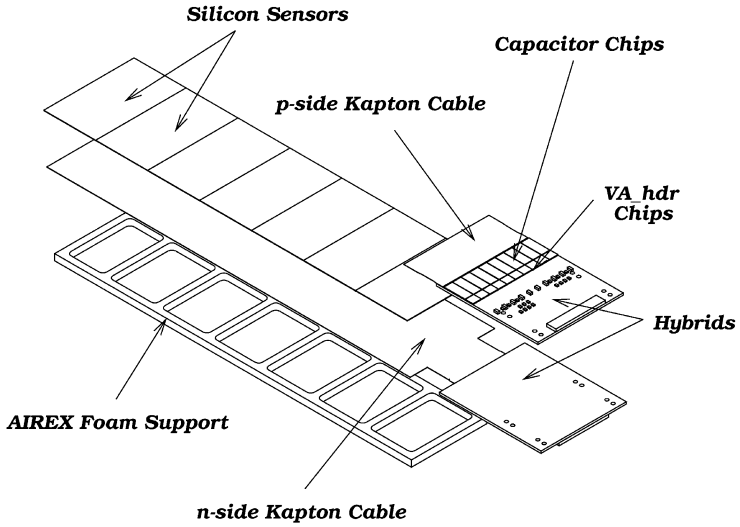

Figure 2.6: Exploded view of a silicon tracker ladder and its components [84].

by capacitive charge coupling was applied to the readout strips. In AMS-01 the six tracker planes were equipped with 3 m^2 of silicon sensors, for a total of 57 ladders and 70,000 readout channels. The sensors were oriented with the p-side strips orthogonal to the magnetic field lines. The system provided positional accuracy of a passing particle through each silicon plane to within 10 μm (30 μm) in the bending (non-bending) side.

To ensure that the AMS-01 detector had the desired accuracy, an infrared laser alignment system was developed. The laser beams partially ionized the silicon as they traversed the tracker planes. Laser-induced signals were used as an on-line monitoring tool to keep under control the system alignment.

The front-end electronics of the tracker were made of very low noise VLSI units. Each channel consisted of a hold low-noise charge preamplifier. They were read

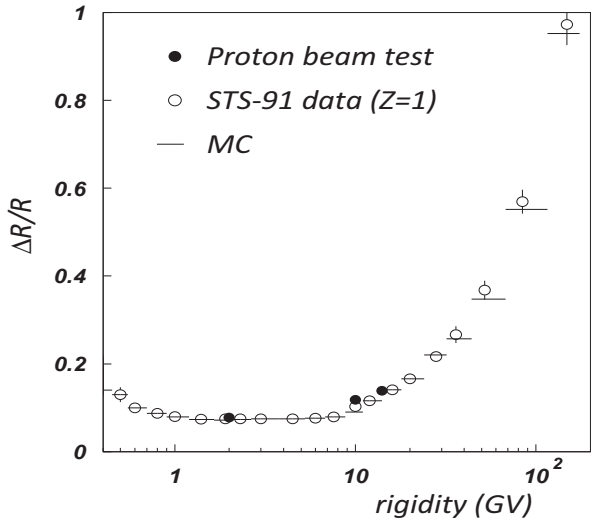

Figure 2.7: Silicon tracker rigidity (R) resolution averaged over tracks with 4, 5 and 6 hits for $Z = 1$ flight data compared with Monte-Carlo and CERN-PS beam test measurements (in this case $\Delta R/R = (R_{meas} - R_{beam})/R_{beam}$).

out sequentially at speeds up to 5 MHz. The data reduction electronics for the tracker were specifically designed to be light weighted and to use minimum power. The 58,368 readout strips were grouped into logical units of 64 channels. A signal, after passing the decoupling capacitor, was fed into a `VA_HDR.64` chip. After signal shaping and sampling, the chip was sequentially read out by means of an analog multiplexer. Further amplification and digitization of the signals occurred on the Tracker Data Reduction (TDR) boards, which were designed to perform data reduction and calibration as well. The passage of a charged particle in the silicon tracker was then recorded in terms of the position and amplitude of the reconstructed signals on the different planes, the tracker *clusters*, i.e. groups of readout channel with signal-to-noise ratio that exceeded over a certain threshold. The particle impact point was determined using the center of gravity of a cluster of at most five adjacent strips.

The amplitude of a cluster is also a direct measure of the energy deposit, so that this information was used to determine the absolute charge of traversing particles. The electronics developed for this purpose had a large dynamic response, allowing for an identification of charged nuclei that has been a crucial point in this work. As highlighted in this thesis, the silicon tracker provides outstanding capabilities on the identification of high charged ions ($|Z| > 2$). A powerful algorithm for the charge

determination is described in the next chapter (§4).

2.2.4 The Aerogel Threshold Čerenkov

A charged particle traversing a dielectric medium with a velocity βc larger than the light speed in that medium c/n emits electromagnetic radiation, similar to Mach's waves for supersonic speeds in a fluid. The emission angle θ_C depends on the particle velocity and on the refractive index of the medium,

$$\cos\theta_C = \frac{1}{\beta n} \tag{2.3}$$

from which follows that only particles with velocities above the thresholds $\beta_{Th} \equiv 1/n$ emit photons. This can immediately be translated into threshold values in terms of energy or momentum for a given mass, allowing a separation between leptons and nuclei.
The number of photons created by the Čerenkov effect is given by:

$$N_\gamma = L_A \times Z^2 \times \left(1 - \frac{1}{n^2\beta^2}\right) \tag{2.4}$$

where L_A is the path length in the material and Z the charge of the incoming particle.

In AMS-01, an Aerogel Threshold Čerenkov (ATC) counter was located at the bottom of the instrument, below the lowest scintillator plane. The ATC was composed by 168 blocks of size $11 \times 11 \times 8.8\ cm^3$ with refractive index $n = 1.035$, wrapped in Teflon and arranged in two layers. These cells were connected to PMTs through wavelength shifters. The ATC detector was essential for the $\bar{p}/e^-$ and e^+/p discrimination up to the threshold values $p_{th} = 3.51\ GeV/c$. The information of the ATC is not used for this analysis, since the discrimination of high charged nuclei is completely achievable with charge measurements. For the unambiguous identification of low energy leptons it was, on the contrary, essential [85].

2.2.5 The Anti Coincidence Counters

The Anti-coincidence counter system consisted of a cylindrical shell made of 16 modules of plastic scintillator surrounding the silicon tracker inside the magnet. Their function, in conjunction with the Time-Of-Flight counters, was to provide anti-coincidence protection against background particles entering the sides of the AMS apparatus or generated within AMS. Photomultiplier tubes were connected at each end of scintillators. Because of very limited space available and mechanical stability to be mantained, thin wavelength shifter fibers were used to guide the light to the PMTs. The system is shown in Fig.2.9.

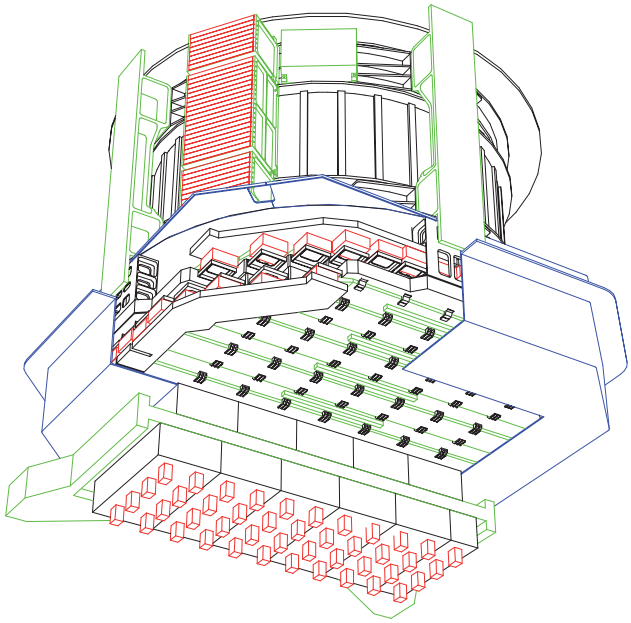

Figure 2.8: The AMS-01 Aerogel Threshold Čerenkov counter layers (only half of them is displayed).

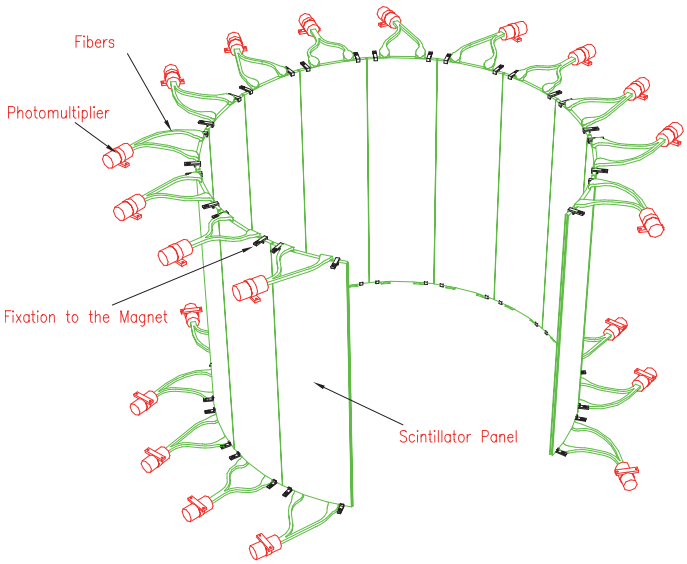

Figure 2.9: The AMS-01 Anti-coincidence System.

2.3 Trigger and DAQ

The trigger is the digital signal that starts the data acquisition (DAQ) chain. This decision is taken if a set of logic conditions is fulfilled. The AMS-01 trigger was

designed with the aim to provide a fast and efficient selection of CR particles entering the detector that could be potentially interesting. The conditions that form the trigger logic are the following [86]:

- **Fast Trigger**
  At least one signal from one photomultiplier on each of the four TOF planes was required. Each scintillator was viewed at its two ends by two photomultiplier triplets combined in OR. If the coincidence of the four TOF planes was not fulfilled within 200 ns, the event was discarded.

- **Level-1 Matrix Trigger**
  As only the central part of the tracker planes was equipped with silicon sensors, a reduced geometrical acceptance resulted. In order not to trigger events whose track could not be measured by the tracker, a correlation matrix between the $14 + 14$ paddles of the two outer TOF planes was set up. Only specific combinations of paddles were accepted, corresponding to tracks traversing the sensitive part of the tracker.

- **Level-3 TOF Trigger**
  The identification of a good event was refined by requiring a signal on both sides of the scintillator paddles. One and only one cluster was required in each plane (a cluster corresponds to one hit or two hits in two adjacent paddles).

- **Level-3 Tracker Trigger 1**
  The TOF conditions were also used to determine a straight fiducial road of 6.2 cm width around the track. The number of tracker clusters inside the road was required to be larger than two and on at least three different tracker planes.

- **Level-3 Tracker Sagitta 2**
  During the pre-docking phase (first 7 hours of data taking) an additional pattern recognition algorithm was applied with the main purpose of rejecting low energy particles. It calculated the residuals from a straight line joining the first and the last TOF cluster and required the average not to exceed a certain value $D = 6\ cm$.

- **Anti-coincidence Trigger**
  It was required that no signal is recorded in the ACC subdetector to discard events with multi-tracks or interacting particles, that produce secondary particles hitting the magnet walls.

In order to characterize the effect of the various trigger conditions, during the STS-91 flight an *unbiased* data set was recorded [87]. This sample was collected by requiring

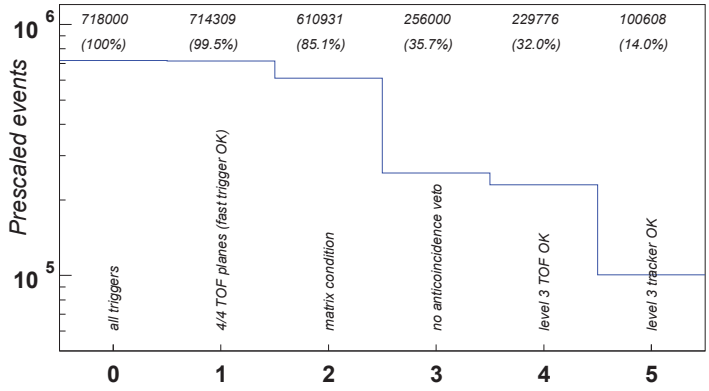

Figure 2.10: The effect of the AMS-01 trigger conditions applied off-line on the proton data collected with the unbiased trigger.

only the fast trigger condition (called also *unbiased trigger*). One out of 1000 normal triggers was prescaled with the unbiased trigger. This unbiased dataset was used to characterize the trigger efficiency for cosmic ray protons, helium nuclei and electrons.

The Data Acquisition system consisted of several steps, including the collection of the digitized signals from each subdetector, event building, data buffering, disk storage and down-link. The total readout dead time was about 100 μs resulting in

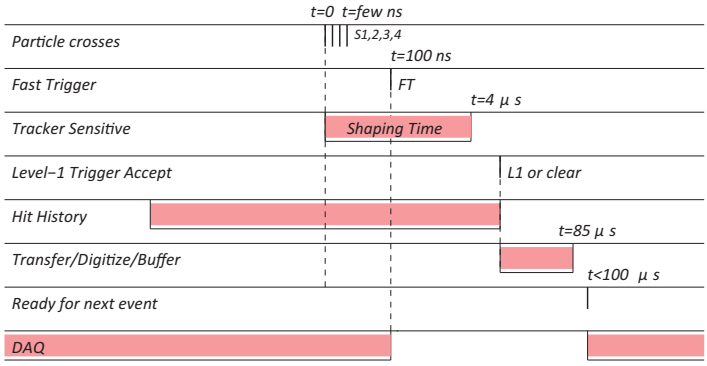

Figure 2.11: Timing sequence of the DAQ Chain.

roughly 13% losses at the highest counting rates. In Fig.2.11 the timing sequence of the trigger logic is shown. After a particle crossed AMS-01, within few nanoseconds the time counting started ($t = 0$) and the information from the four planes of the TOF system was read. Within 100 ns the fast trigger was produced. The shaping time, required by each VA to integrate and amplify the signal, was 4 μs. The TOF readout provided an *history time* gate of about 12 μs, centered on $t = 0$ and

recording the history of the TOF detector before the trigger, with the purpose of monitoring particles traversing the detector but not triggered because out of time. Other 80 μs were required to read, digitize and buffer the readout information and reset the DAQ system ready for a new event.
Within each orbit there was a considerable variation of DAQ live-time as the Shuttle passed through different regions of the earth magnetic field [88]. This variation reflects the geomagnetic cutoff. The AMS-01 DAQ live-time fraction α varied between 0 and 96%, corresponding to recorded event rates of 700 to 100 Hz. The

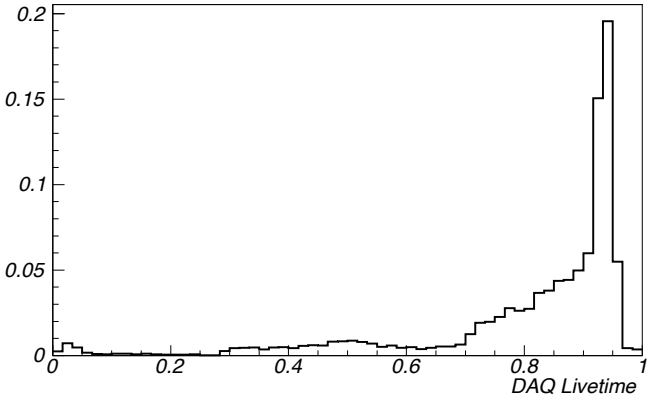

Figure 2.12: Normalized DAQ live-time distribution over all the data taking period.

lowest live-time generally corresponds to high particle fluxes observed near the polar geomagnetic latitudes reached by the Shuttle. The average live-time was about 80% on the whole orbit, and drop when the Shuttle was passing through the South Atlantic Anomaly (§1.3.2), where the high CR rate precluded effective data taking. The live-time distribution is shown in Fig.2.12. To avoid large correction for DAQ live-time inefficiencies, data collected close to the SAA region are excluded from the analysis (§3.3).

2.4 The Offline Software

The purpose of AMS-01 was to identify cosmic rays and measure their momentum. A particle can be identified when its mass and signed charge are known, which are determined by the velocity, rigidity and energy deposit in the active material. For this purpose, an event reconstruction algorithm has been developed to process the raw signals from the subdetectors and to return rigidity, velocity, charge sign and charge magnitude [89, 90]. The response of the AMS-01 spectrometer to the passage of charged CR particles has been extensively studied by means of the Monte-Carlo

simulation program `AMS-GBATCH`. Other simulation frameworks have been developed to better characterize the trigger response for high charged particles. Reconstruction detector simulation softwares are described in the next subsections.

2.4.1 Event Reconstruction

In AMS-01 the physical quantities to be reconstructed are the particle charge Z, rigidity R and incoming direction (θ, ϕ). The particle mass is derived from the measured velocity and the momentum $p = RZ$. The sign of the charge is determined from the curvature of the reconstructed trajectory.

Velocity reconstruction

Readout devices summed the signal from the three PMTs at the end of each TOF paddle, for anode and dynode. These signals were used to generated fast trigger and time measurement.
For each TOF signal, a mean time (t_m) is computed from the time measurements at the two ends 1 and 2 of the paddle:

$$t_m = \frac{t_1 + t_2}{2} \tag{2.5}$$

Using the known effective velocity of light in the scintillator material, the particle impact point along the paddle can be estimated. Time measurements are also corrected for time slewing due to variations in the PMTs pulse heights, cabling lengths and incident angle. A linear fit on the value t_m versus the track length is then performed to find β^{-1}.

Track Reconstruction

Track reconstruction begins in the DAQ electronics of the tracker. On-board data compression was done by selecting strips that have signal-to-noise ratio over a given threshold (3.5 for p-side, 2.75 for n-side) as seeds to form the clusters with the adjacent strips.
Clusters from both sides of the silicon are used to generate three-dimensional hits by combining the X and Y positions of all possible p-side and n-side combinations. Each n-side channel has a 6 to 8-fold position degeneracy (i.e. 6 to 8 positions associated with the same readout channel) due to the readout scheme used. Thus the number of candidate hits may be quite large. This degeneracy is fully resolved using multiple layers and combining information from the TOF data.

A charged particle in a homogeneous magnetic field moves along a helical trajectory with radius proportional to the particle momentum. At first approximation

the track is regarded as a straight line, and a linear fit procedure over all the hit combinations is performed to recognize the track. The set of hits with lowest χ^2 is the best track candidate. Then a helical fit is computed. If its χ^2 is below a given threshold, the track hits are passed to a more sophisticated fitting procedure, that accounted for a realistic magnetic field distribution and the material traversed by the particle.
Deviations in particle track are caused by multiple scattering in the silicon support material and are included in the error estimation. Two different track reconstruction algorithms are used

- **Fast Fit Algorithm.** This widely diffused algorithm [91] is based on a matrix inversion that iteratively minimizes a χ^2 between measured hit and propagated hits. These latter are reconstructed from a trajectory numerically propagated through the **B** field from a set of initial kinematic conditions. The fit is performed twice, with and without including multiple scattering in the error estimation. Disagreement between the two fits could indicate events with large amount of Coulomb scattering integrated along the tracker material. The Fast Fit was also applied to the first and last three hits in the tracker to reconstruct two independent *half tracks*. Disagreement between the two corresponding half rigidities and the overall rigidity could indicate a particle that underwent large scattering angle or a failure in the rigidity reconstruction.

- **GEANE Fit Algorithm.** The `GEANE` tracking algorithm [92] was used to calculate particle trajectory, transport matrix and covariance matrix. This algorithm propagates the tracks through the inhomogeneous magnetic field under the framework of `GEANT3` Monte-Carlo simulation [93]. All the relevant physics processes are then included and simulated (2.4.2). The track is evaluated with a Kalman filter method [94].

Charge Reconstruction

The charges of the particles are determined by a maximum likelihood method applied to the truncated mean of the energy deposits.
The truncated mean was computed separately for the four TOF clusters and up to $6 + 6$ tracker clusters in both the silicon sides. Clusters are selected by the above mentioned track reconstruction algorithm. The truncated mean is the average cluster amplitude excluding the contribution from the cluster with the highest energy deposit. This reduces the effects of the Landau fluctuations, i.e. avoids discrepancies between mean and MPV value of the energy deposit distributions.
Likelihood functions have been estimated from a set of calibration measurements made at the CERN PS (protons) and GSI (helium) beam test data. Flight data themselves have been used too. Probability distribution functions $f(\Delta E, \alpha(Z))$ are

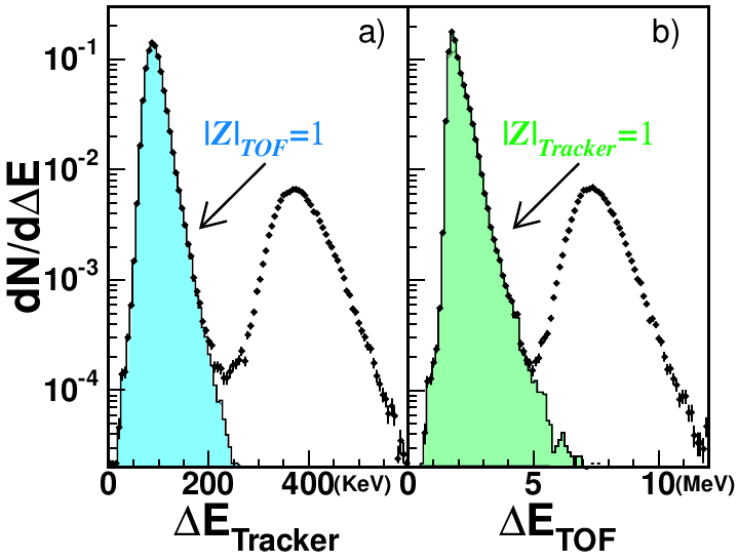

Figure 2.13: Tracker-TOF charge identification capabilities [105]. Energy loss (points) are made independently in the tracker (a) and TOF (b) for $|Z| \leq 2$ events. The filled histograms show which events were assigned to be $|Z| = 1$ with the other detector.

defined by considering separately the energy losses in the TOF and in the tracker. For the tracker cluster amplitudes, a combination of the two sides is considered. Two sets of truncated mean are then calculated and corrected for the particle incidence angle. A β^{-2} dependence is also accounted in the PDFs. The maximum likelihood equation is solved separately for the various sample of measurements and a charge Z is finally computed as the value for which the probability P_Z is maximum. Two charges are assigned to each event independently from TOF and tracker, i.e. two probabilities P_Z^{TOF} and P_Z^{Tk} are computed. For charge up to $|Z| = 2$ the TOF and tracker information are combined together in a unique Z estimation. Fig.2.13 shows the charge identification capabilities of the two instruments for $Z = 1$ and $Z = 2$ [105].

For $|Z| > 2$ only the tracker information can be used, due to the limited dynamical range of the TOF readout electronics. In this thesis, a new improved charge identification algorithm has been developed for $Z > 2$ ions. It is described in Chapter §4.

2.4.2 The Monte-Carlo Simulation

The response of the AMS-01 spectrometer to the passage of charged CR particles has been extensively studied by means of the Monte-Carlo simulation program

AMS-GBATCH. In AMS-GBATCH the detector geometry design is described in detail: mechanical drawing, detector mis-alignments, support structures, dead sensors and the measured magnetic field map are included. The GEANT-3.21 software is implemented to simulate the energy deposits and the interactions of incident particles within the different detectors, as well as their transport in the material and the magnetic field. Physical signals are then converted in the equivalent experimental readout[2], to be combined together for reproducing the trigger chain. These raw signals are then processed by the event reconstruction algorithm as it would to be done in the real data, and finally compiled into PAW ntuples or ROOT-Tree objects [98]. Together with the reconstructed quantities, the original Monte-Carlo records of the generated particles i.e. the true kinematic parameters are provided.

NUCLEUS	MOM RANGE	GENERATED	STORED
^{7}Li	$2 \div 250\ GeV/c$	$100,000,000$	$539,116$
^{9}Be	$2 \div 250\ GeV/c$	$100,008,090$	$412,855$
^{10}Be	$2 \div 250\ GeV/c$	$105,635,216$	$497,303$
^{10}B	$2 \div 250\ GeV/c$	$100,000,000$	$398,637$
^{10}B	$199 \div 560\ GeV/c$	$20,000,000$	$67,523$
^{11}B	$2 \div 250\ GeV/c$	$102,400,101$	$392,723$
^{11}B	$219 \div 506\ GeV/c$	$20,000,000$	$66,576$
^{12}C	$2 \div 250\ GeV/c$	$100,000,000$	$345,777$
^{12}C	$239 \div 552\ GeV/c$	$20,000,00$	$51,905$
^{14}N	$2 \div 250\ GeV/c$	$200,147,195$	$628,780$
^{16}O	$2 \div 250\ GeV/c$	$200,007,225$	$554,142$

Table 2.2: Monte-Carlo production table for $Z > 2$ cosmic ray ions.

As a general procedure, the first step of a simulation consists in the random generation a cosmic-ray flux according to the expected energy and angular distribution for the channels under study.
In order to sample the full energy spectrum with significant statistics and prevent the total production to grow beyond a manageable size, some optimizations have been performed, connected to the choice of the *probe spectrum* and the *generation volume*: only particles that may contribute to the acceptance have been simulated, and a flatter probe spectrum has been employed rather than the expected one. Moreover, only events that satisfy trigger conditions involving the TOF are stored in the disk. Further details on the generation strategies are provided in Section §5.1.

For an accurate estimation of the detector response, large samples of Monte-Carlo

[2] The responses of each device have been experimentally determined by calibration measurements performed on the detector during the pre-flight testing phase.

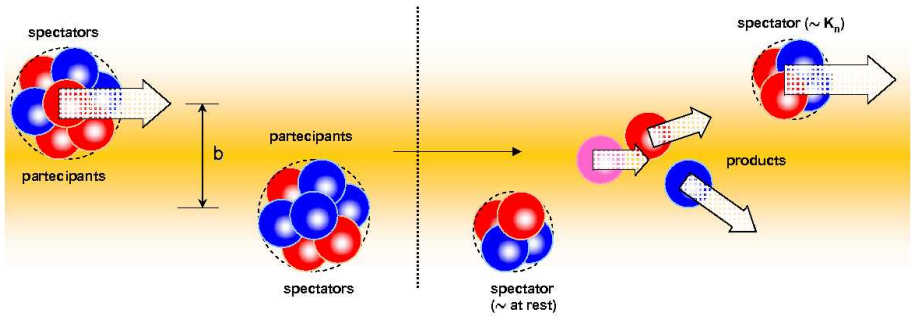

Figure 2.14: A schematic view of the nucleus-nucleus inelastic collision at high energies. Only the low impact parameter nuclei regions are involved in the fragmentation. Residual non-interacting nucleons are spectators and tend to conserve the original kinetic energy.

events have been produced for all the particle species observed by AMS-01. For the purpose of this work, the samples considered are those containing Lithium, Beryllium, Boron, Carbon, Nitrogen and Oxygen nuclei. B and C are the channels under study, while the other species are sources of possible background. The MC production is summarized on Table2.2.

2.4.3 Inelastic Collisions and the AMS-VMC project

For a reliable simulation of the detector response in the ion channels, a detailed description of nuclear interactions in the active and passive AMS material is fundamental. In fact, inelastic collisions and fragmentation processes affect the detector acceptance in the measurement of the differential fluxes. The role of interaction in the detector have therefore been taken into account.

For this purpose, under AMS-GBATCH, the particle transport code GEANT3 has been interfaced with the RQMD hadronic package (*Relativistic Quantum Molecular Dynamics* [95]). RQMD describes nucleus-nucleus collisions under phenomenological models inspired to the QCD and based on the Lund model [96]. The collisions are treated by a geometrical point of view. Projectile nucleons and target collide along their straight line trajectories (see Fig.2.14). Some nucleons, called *participants*, undergo inelastic interactions in the process, and the other ones, called *spectators*, do not take part to the process. The kinetic energy per nucleon is roughly conserved in each final product. The interaction probability is given by the inelastic cross sections. As RQMD is made for reproducing an effective description as much realistic as possible, the nucleus-nucleus cross sections are based on experimental data and hadronic interaction models. This approach fixes the free parameters of the underlying models, and turns out to be particularly helpful in analyzing the role of fragmented events

in experimental contexts.

Besides AMS-GBATCH, additional simulation tools have been developed for AMS as original part of this work. The main purpose is the validation the AMS-01 acceptance estimation under different physics models of particle interactions, as unbiased data did not give enough statistics (§5.2).

A stand-alone Virtual Monte-Carlo application (AMS-VMC) has been implemented for AMS-01 [97]. The concept of VMC and its development for AMS-01 are described in Section §5.2.1. A short description of the VMC physics models implemented is outlined as follows.

The VMC libraries are integrated into the ROOT framework [98]. The basic idea of the AMS-VMC project is to use a unique interface to run different transport codes. Three stand-alone simulations have been implemented for AMS-01:

- VMC-GEANT3
  This version implements the same physics engines of the standard simulation program AMS-GBATCH. Particle transport and electromagnetic interactions are simulated by GEANT-3.21; the heavy ions fragmentation is implemented with a RQMD-1.07 interface. As it is fully independent from AMS-GBATCH, VMC-GEANT3 has been used as a control interface for the description of the detector response and the trigger logic in the VMC context.

- VMC-GEANT4
  The particle transport and interactions are based on GEANT4 [99]. Inelastic collision and ion fragmentation are simulated via the
  G4-Binary-Ion-Reaction class, based on the binary cascade interaction model [100]. In this representation, each participant nucleon is seen as a gaussian wave packet. This wave function has the same structure as the classical Hamilton equations, calculated with a time-dependent optical potential, and can be solved numerically. For light ions ($A < 16$), the nuclear matter distribution follows the harmonic oscillator (shell model), as well as the optical potential.

- VMC-FLUKA
  This version of VMC supports FLUKA. The transport of charged particles is performed through an original multiple coulomb scattering algorithm [101], with inclusion of nuclear form factor for heavy ions. The treatment of ionization energy loss is based on a statistical approach, alternative to the standard Landau and Vavilov ones, that provides a very good reproduction of average ionization and fluctuations. Nucleus-nucleus interactions are supported in three models. Below 100 MeV/n the simulation is based on the Boltzmann Master Equation

(BME) theory for nucleus-nucleus interactions. At higher energies, `RQMD-2.4` is used for heavy ion reactions. Above 5 GeV/n the simulation runs under the `DPMJET-III` event generator [102], which based on the Dual Parton Model in connection with the Glauber formalism.

Simulation results for these different models are presented in §5.2.1. The `AMS-VMC` project is currently under further development for the AMS-02 incoming experiment.

2.5 AMS-01 on the Space Shuttle

STS-91 was the final flight of the NASA Shuttle Program to the MIR space station [103]. The flight lasted 10 days. Its main purpose, beside providing the last Shuttle-MIR rendezvous mission before the ISS construction (the final location of the AMS-02 experiment) was to test the spectrometer under real space flight conditions. During this 10 day mission, after an initial checkout phase, AMS-01 had $\sim$ 184 hours of dedicated data taking time [104]. A large amount of data on the fluxes of different cosmic-ray particles in near Earth orbit was collected. Analysis of those data led to significant physics results on rates and spectra of galactic cosmic rays (§2.6) in the kinetic energy range 0.1 $GeV/n \div 100$ GeV/n, and provide the most precise upper limit at that time on the anti-helium to helium ratio [105]. STS-91 flight was operated by Space Shuttle Discovery, launched from Kennedy Space Center, Florida on June 2^{nd}, 1998. The orbit had an inclination of 51.7° and an altitude varying between 320 km and 390 km.

To operate the AMS electronics and detectors required about 700 Watts of power from the shuttle. AMS was also set to be commanded from the ground, especially during the checkout phase. Monitoring data were generated by AMS and transmitted at a net rate of 10 Kb/s during the 70% of the time. Though the events recorded were written locally to disk, an on-line down-link had been foreseen for science data too: 10% of the data were transmitted to ground, allowing the on-line monitoring of the detector performance.
The weight of the payload was $4,200$ kg. It was mounted in the rear of the shuttle bay with the doors open during the whole flight. The SpaceHab module and MIR docking equipment were located in front of AMS.
In addition to the goals mentioned above, this mission served to exercise command and data interfaces, measure backgrounds to allow the trigger and detectors to be tuned for the the AMS-02 mission, and verify the AMS thermal modeling.

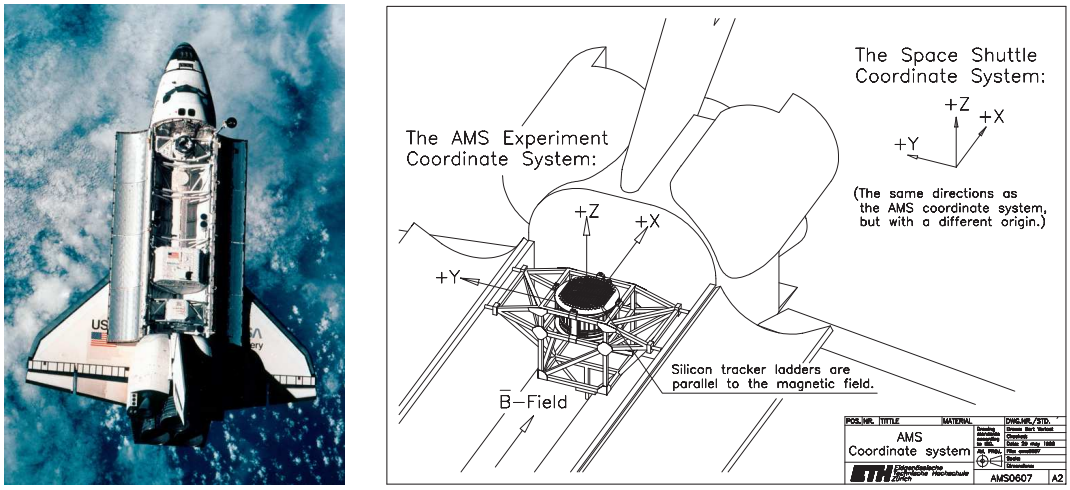

Figure 2.15: Left: picture of the Space Shuttle Discovery taken from the MIR space station during the docking phase. Right: configuration of AMS-01 on the Discovery Space Shuttle.

2.5.1 Flight Parameters

The Discovery orbital parameters during flight STS-91 are an essential ingredient of the AMS data analysis. The flux, the momentum range and the composition of the particles recorded by the spectrometer depended critically on the position and the attitude of the Shuttle during the on-orbit period. The relevant parameters available from NASA during and after the flight were time, position, velocity and attitude of the shuttle.
A reference frame is defined at a given time (epoch) by an origin and three orthogonal axes fixed with respect to a given body (Earth, Shuttle, etc). In this reference frame a point P is defined by:

- **Cartesian coordinates:** the tree components (X, Y, Z) of a vector $\vec{R}$ from the origin P.
- **Spherical coordinates:** the magnitude of the vector $\vec{R}$, the angle ϕ between the projection of $\vec{R}$ on the XY-plane and the X-axis, positive toward the Y-axis, and the angle θ between $\vec{R}$ and the XY-plane. Note that this is not the usual definition of a spherical coordinate system, as the angle θ is not with respect to the Z-axis. In Cartesian coordinates:

$$\begin{aligned} R &= \sqrt{X^2 + Y^2 + Z^2} \\ \phi &= \arctan\left(Y/X\right) \\ \theta &= \arcsin Z/R \end{aligned} \tag{2.6}$$

- **A set of parameters:** e.g. the geodetic latitude, longitude, altitude.

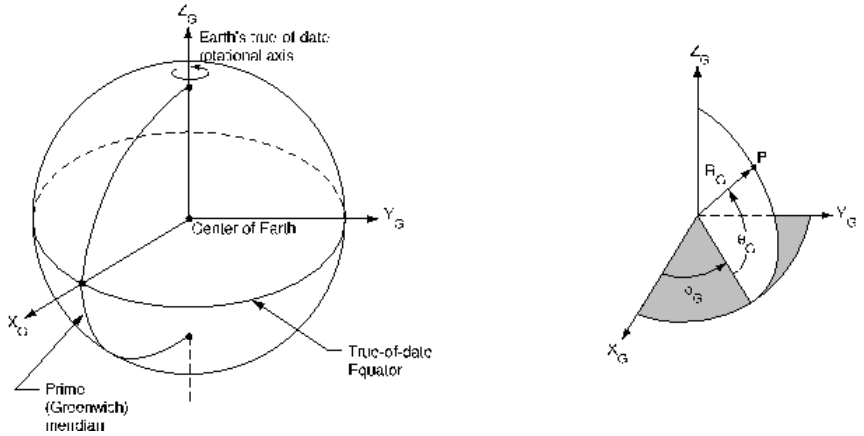

Figure 2.16: Greenwich True-of-Date Reference Frames: a) Cartesian coordinates. b) Spherical coordinates.

In this work the *Greenwich True-Of-Date* (GTOD) reference frame is used [106]. It is defined as a fixed reference frame relative to the Earth, and rotating together with it (Fig.2.16). The three components (X_G, Y_G, Z_G) are specified as follows:

1. The $X_G Y_G$-plane is the Earth True-of-date Equatorial Plane.
2. The X_G-axis is directed toward the prime (Greenwich) meridian.
3. The Z_G-axis is directed along the Earth True-of-date rotational axis and positive North.
4. The Y_G-axis completes a right-handed Cartesian system.
5. The angle ϕ_G is called Geocentric Longitude, the angle θ_G Geocentric Latitude.

Once the position of the spacecraft is determined, its orientation is specified by the *Body Axes Reference Frame* (Fig.2.17). The origin is the Shuttle center of mass. The X_S-axis is parallel to the Shuttle structural body axis, positive toward the nose. The Z_S-axis is perpendicular to the X_S-axis and parallel to the plane of symmetry, positive toward the bottom of the Shuttle airframe. The Y_S-axis completes the right-handed orthogonal system. The attitude sequence associated with this system is a *yaw-pitch-roll* sequence. It defines the Shuttle orientation relative to a coordinate system XYZ as the maneuver sequence which would align the body axes $X_S Y_S Z_S$ with the XYZ axes as follows:

1. Yaw the angle ψ around the Z_S-axis (positive is X_S to Y_S).
2. Pitch the angle θ about the Y_S-axis (positive is Z_S to X_S).

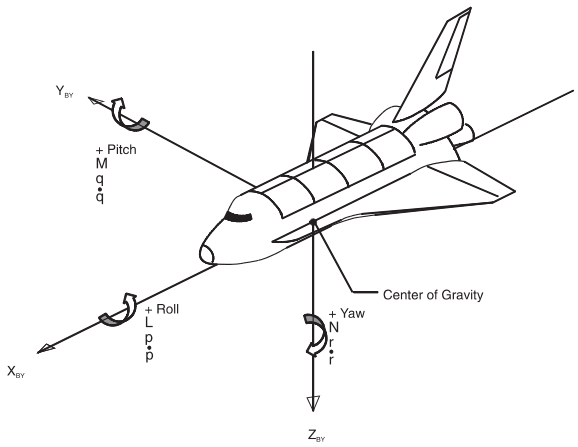

Figure 2.17: Body axes reference frame

3. Roll the angle ϕ about the X_S-axis (positive is Y_S to Z_S).

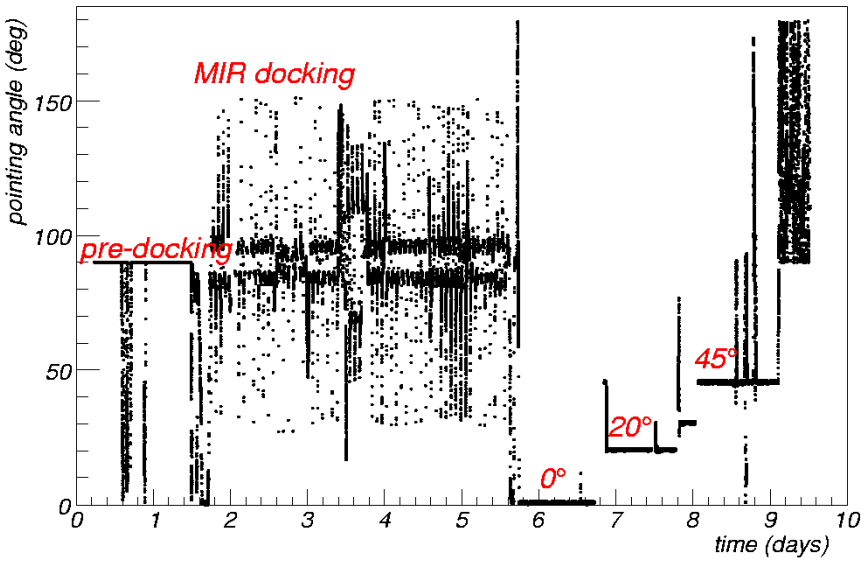

Figure 2.18: Attitude (or pointing angle) of AMS-01 with respect to the zenith versus mission elapsed time. The period of great variability corresponds to the Shuttle-MIR docking phase. Dedicated exposure time at different fixed angles was available after docking.

where ψ, θ and ϕ are the Euler angles of the corresponding rotations, to be implemented with the usual rotation matrices R_ψ, R_θ and R_ϕ.
The AMS-01 body axes (Fig.2.4) are rotated 180° around the Y_S-axis with respect

the Shuttle body axes: the AMS-01 X-axis points toward the tail of the Shuttle, and the Z-axis points upward from the shuttle. The origin is also shifted to the AMS-01 center of symmetry. The attitude angle is seen as the AMS pointing direction with respect to the zenith direction. Fig.2.18 shows the AMS-01 attitude as a function of the mission elapsed time (days). The period of great variability ($\sim 2^{nd} \div 5^{th}$ day) corresponds to the Shuttle-MIR docking phase, when AMS-01 and the MIR were co-moving together as a unique body, and the resulting attitude followed the MIR precession motion accordingly. Dedicated exposure time at different fixed angles was available after docking (i.e. plateaus at 0°, 20°, 45° in the figure).

2.6 AMS-01 Physics Results

From the STS-91 flight of AMS-01, experience and knowledge on how to execute a particle physics experiment in space have been gained. The construction of the complete AMS-02 detector, which will operate on the International Space Station, has benefited of this test flight for technical capabilities and performance of each component under actual flight conditions. The detector performance as well as the temperature and the alignment were monitored continuously during the flight. After the flight, AMS-01 was checked again. The continued monitoring of AMS-01 confirmed that the detector performance before, during and after the flight remained the same.

Though STS-91 was an engineering flight, nearly 100 million events were collected and analyzed. In addition to validating the AMS concept, analysis of these events led to the following significant results:

- **Search for anti-helium in cosmic rays**
  A total of 2.86×10^6 helium nuclei with rigidity up to 140 GV were observed. No antihelium nuclei were detected at any rigidity. The upper limit on the ratio of the flux of antihelium of less than 1.1×10^{-6} has been obtained [105].

- **Protons in near earth orbit**
  The proton spectrum in the kinetic energy range 0.1 to 200 GeV was measured. Below the geomagnetic cut-off, a substantial *second spectrum* was observed. Most of these second spectrum protons follow a complicated trajectory and originate from a restricted geographic region [107].

- **Leptons in near earth orbit**
  The lepton spectra in the kinetic energy ranges 0.2 to 40 GeV GeV for e^- and 0.2 to 3 GeV for e^+ were measured. From the origin of the leptons two distinct spectra were observed: a higher energy spectrum and a substantial

second spectrum with positrons much more abundant than electrons. Tracing leptons from the second spectra shown that most of these leptons travel for an extended period of time in the geomagnetic field and that e^+ and e^- originate from two complementary geographic regions [108].

- **Cosmic protons**
  The precise primary proton spectrum in the kinetic energy range 0.2 to 200 GeV was accurately measured. Above the geomagnetic cut-off, the observed spectrum is parametrized by a power law [109].

- **Helium in near earth orbit**
  The helium spectrum from 0.1 to 100 GeV/n was measured. Above the geomagnetic cut-off, the spectrum is parametrized by a power law. Below the cut-off, a second helium spectrum was observed. In the second helium spectra over the energy range 0.1 to 1.2 GeV/n, in the geomagnetic latitude from $-0.4 \div +0.4$ rad, the flux was measured to be $(6.3 \pm 0.9) \times 10^{-3}/(m^2 sec\ sr)$ and, contrary to expectations, more than ninety percent of the helium was determined to be ^3He (90% CL) [110].

- **Study of trapped high energy CR in near earth orbit**
  Detailed analysis of the particles below geomagnetic cut-off have established the existence of permanently trapped high energy p, e^+ and e^- with trajectories crossing the South Atlantic Anomaly [111].

- **Positron fraction measurement**
  A measurement of the cosmic ray positron fraction $e^+/(e^+ + e^-)$ in the energy range $1 \div 30$ GeV was published. The results have confirmed the anomaly obtained in previous experiments and deeply discussed as a possible signature of new physics [74].

- **Deuterons and antiprotons**
  A total of 10^4 deuterium nuclei in the energy range 0.1 to 1.0 GeV/n were observed allowing the first accurate test of galactic confinement models. The antiprotons flux was measured between 0.2 and 5 GeV of kinetic energy [70].

The present study of the nuclear components of the cosmic rays therefore completes the variety of subjects successfully investigated by the AMS-01 experiment.

Chapter 3

Data Selection

The goal of this analysis is to find the energy spectra of the light CR nuclei, with particular regards to Boron and Carbon and their ratio. In this chapter the event selection will be presented and discussed. The various cuts imposed to the data can be classified in two different sets:

- Cuts depending on the detector measurements.
- Cuts depending on the orbital conditions.

The first set of cuts is based on the quality of the detector measurements. Cuts are defined and studied with the aim of removing all events whose parameters have been poorly determined. This selection has been imposed to the whole dataset with no regards about the nuclear species involved, i.e. the same selection criteria are applied for all the $|Z| > 2$ measured data. These criteria are developed with the help of a Monte-Carlo simulation for the detector reconstruction capabilities, but much care and attention have been payed to the measured data themselves.

Then, few global cuts depending on the orbital conditions are outlined in the second part of this chapter. Data collected when the shuttle passed over the *South Atlantic Anomaly*, where the trigger rate saturated, have been excluded. A global orbit-dependent rigidity cut has been applied to the low energy part of the spectrum, distorted by the Earth magnetic field. Finally, during the shuttle-MIR docking phase, part of the MIR space station lay in the AMS-01 field of view and affected the measured flux. This MIR shadow has been cut away from the detector acceptance.

3.1 Initial Dataset

During the Shuttle mission STS-91, 99 million events were detected by AMS-01. The majority of these particles are protons (Z=1) and helium nuclei (Z=2). The raw

data from the flight were processed by the AMS-01 event reconstruction program (§2.4.1) and compiled into PAW ntuples. Reconstruction was performed as described in Section §2.4.1. The ntuples included track, velocity, charge sign and magnitude and all the relevant information from the detector and the orbit. The structure of these ntuples is described elsewhere [112].

Starting from this standard output, a preliminary selection of the nuclear candidates has been done. The initial set of preselection cuts required each event to satisfy the minimal requirement to have exactly one reconstructed particle with associated track and nuclear charge $|Z| > 2$. A total of 232,035 candidates have been identified at the preselection level collected during the whole data taking period.

3.2 Detector Cuts

A quick inspection of the preselected candidates reveals that a fraction of them came from mis-reconstructed trajectories. A set of quality cuts has then been applied to eliminate these mis-measured events, with the aim to obtain a clean sample of nuclei maximizing the acceptance in the entire rigidity range accessible to the detector.

Detector cuts involve variables reconstructed from information of the TOF scintillator and from the silicon tracker. Since the selection efficiency, estimated with MC data, might play an important role in the final B/C measurement, much care has been taken in using the observable quantities better reproduced by the MC simulation. A charge independent selection has been carried out, mainly based on quality criteria involving the tracking. Other criteria involving the goodness of the charge identification are described in the next chapter.

3.2.1 Monte-Carlo Normalization

Selection cuts have been defined with the help the Monte-Carlo simulation program AMS-GBATCH. The simulation setup and the features of the generated data are described in sections §2.4.2 and §5.1. The final output of the full simulation is a compressed data file with exactly the same format as flight data, plus information on the original Monte Carlo record of the generated particles and their kinematics. The MC *probe spectrum* exhibits a momentum distribution:

$$\frac{dN}{d\log P} = const \tag{3.1}$$

that corresponds to a momentum power-law with spectral index $\gamma = -1$, whereas the CR ions are described with a kinetic energy power-law with $\gamma \sim -2.5$.

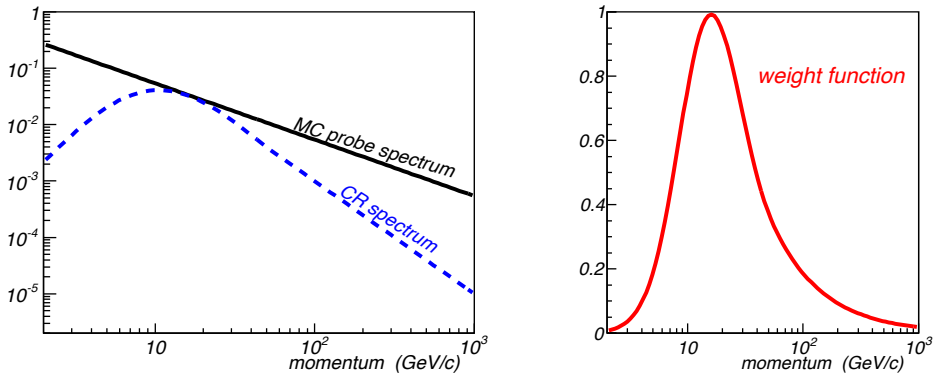

Figure 3.1: Left: Monte-Carlo probe spectrum in comparison with a typical CR expected spectrum after solar modulation applied. Spectra are shown in arbitrary units. Right: Rescaling function defined as the ratio of CR and MC left spectra (CR/MC). A more physical CR spectrum is obtained weighted the MC distribution by this factor. This weighted spectrum will be used in the future MC-DATA comparisons.

The choice to use a flatter probe distribution is an efficient generation strategy aimed to maximize the detector response study at high energy.
The role of MC in this analysis (via efficiencies, acceptance, resolution) is pretty much independent on its probe spectrum distribution. However, for an appropriate comparison DATA-MC over all the energies, the MC spectrum have been weighted according to the expected CR distribution.
In Fig.3.1 the MC spectrum is shown and compared with a more physical CR spectrum (power law in kinetic energy) after conversion in momentum units and accounting for the influence of the solar activity (§1.3.1). The weight function (on the right) is just defined as the ratio of the two spectra CR/MC.

3.2.2 Quality of Time Of Flight Measurements

During the data taking, the AMS-01 instrument was traversed in up-ward and downward directions by the approximately isotropic flux of cosmic rays. Particles coming from the bottom were also able to be accepted by the trigger and reconstructed as well. Fig.3.2 shows the signed β distribution of the events collected during the flight (left). The traversing direction was determined with no ambiguity by the Time Of Flight system. This is a key point to discriminate the sign of the charge, together with the track curvature. However, upward-going nuclei most likely interact with the detector support structure or with the shuttle airframe before reaching the

spectrometer. Thus, the accuracy in their composition and energy measurement is spoiled by fragmentation and energy losses. Upward-going events have been therefore excluded from this analysis, and not considered in the following discussion.

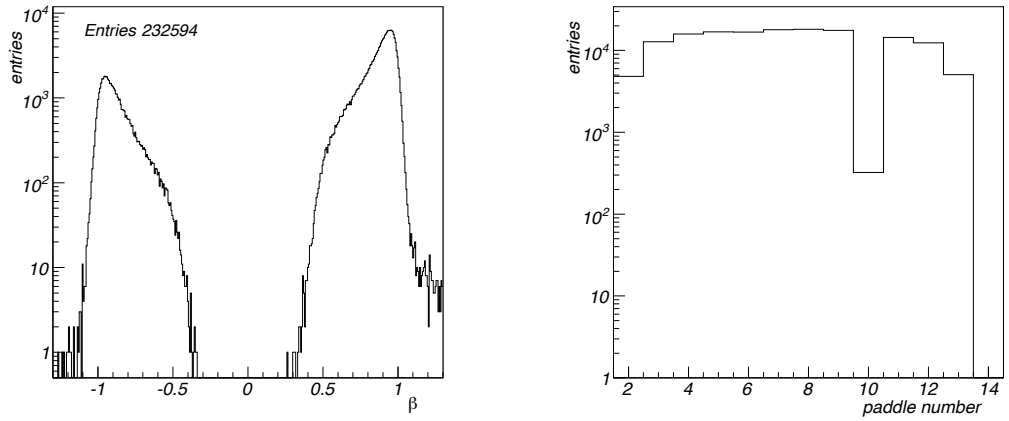

Figure 3.2: Left: Distribution of signed velocities measured by the TOF. The leftmost population (upward-going particles) has been discarded. Right: Paddle occupancies in Layer 3. Due to an abnormal behaviour, Paddle 10 results less efficient in yielding reconstructed particles. All the trajectories traversing this paddle have been discarded.

During the flight, Paddle 10 on the third TOF layer provided unreliable response. As shown in Fig.3.2 (right), this anomalous behaviour made a considerably less efficient triggering and reconstruction for all the particles crossing this paddle. All the event containing a hit in this paddle ($O(\%)$ of the high Z candidates) are thus discarded from the flight data as well as from the Monte-Carlo sample.

3.2.3 Acceptance Restriction

A restricted acceptance of 32° from the negative z-axis was used (θ_{AMS}>2.58 rad in the AMS reference frame) as applied in previous AMS-01 analyses [108, 107]. There are two main reasons to consider this restriction. Due to the particular tracker geometry (§2.2.3), particles coming with high inclinations have little chance to hit the upper and lower silicon layers; hence, a restriction in the azimuthal angle θ_{AMS} reduces the fraction of events with small lever arm in the tracker, typically associated to poorly reconstructed tracks and charges. Furthermore, since the AMS-01 tracker geometry was far from being a truly cylindrical symmetry, a pronounced structure on the azimuthal coordinate distribution ϕ_{AMS} has been observed, that would make more appropriate a differential acceptance study. Unfortunately, the collected statistics for $Z > 2$ particles is not enough for a detailed study of the

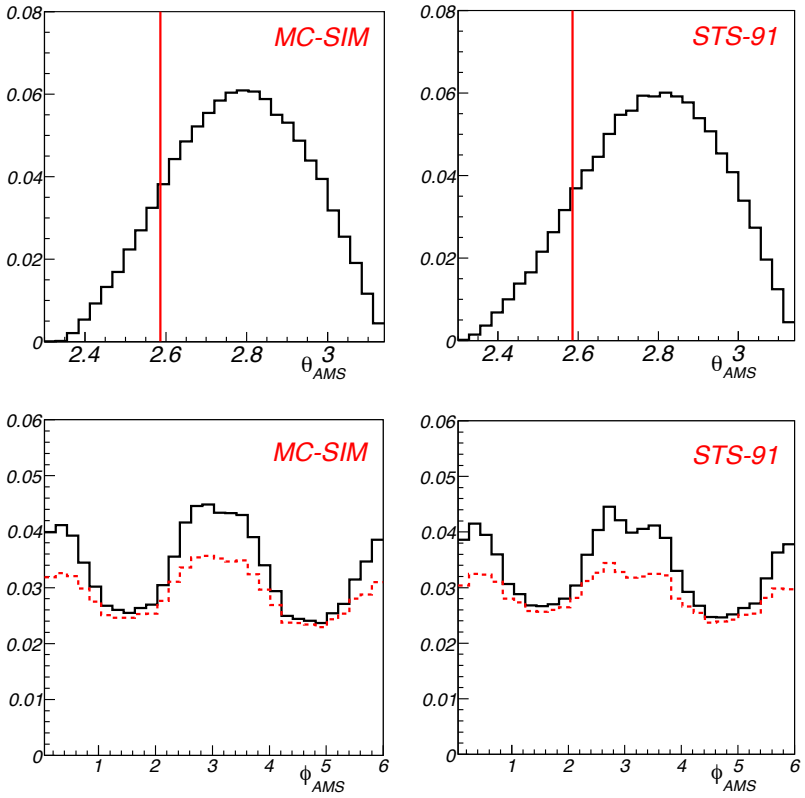

Figure 3.3: Normalized distributions of θ_{AMS} (upper panels) and ϕ_{AMS} (lower panels) from MC simulated data (left) and flight data (right). A cut on trajectories with high inclinations θ_{AMS} is applied as shown (left part is removed). the more uniform ϕ_{AMS} distribution after the cut is indicated by the dashed red line.

incoming fluxes differentiating θ_{AMS} and ϕ_{AMS} intervals. A restriction on the track inclination is then helpful to produce a more uniform ϕ_{AMS} structure, as indicated in Fig.3.3. In the next sections, all the distributions presented satisfy the cuts on *beta* (downward-going), no paddle 10 in 3^{rd} TOF-plane and $\theta_{AMS} < 32°$.

3.2.4 Quality of Track Reconstruction

In this section a basic set of criteria for the rejection of poorly measured tracks is defined. Firstly this will be presented only for the Monte-Carlo data. To identify the quantities most sensitive to mis-reconstruction, the first step has been to split our MC data sample into two streams of events (*good* and *bad*) w ith different accuracy of the reconstruction. The distributions of several experimental quantities in the different streams have been compared to identify the most useful for our selection. Since in Monte-Carlo data the true kinematical parameters are exactly known, the

relative deviation of the reconstructed from the generated rigidity of the particle can be defined as:

$$\delta R \equiv \frac{R_{gen} - R_{meas}}{R_{gen}} \tag{3.2}$$

Poorly reconstructed events are those for which large δR; thus the condition $\delta R > 1$ will be used to classify the *bad* event stream. Since the rigidity resolution is expected to depend on the rigidity itself, this classification is rigidity-dependent as well. In the following sub-sections, a set of cuts will be presented with the above mentioned criteria for Monte-Carlo samples of Boron and Carbon.

Subsequently (§3.2.5) the same distributions will be plotted and further examined in comparisons with the real data as *last cuts* (i.e. with all the other cuts of the set already applied to the sample) to see explicitly the effect of each cut on the data.

In this section, all data distributions will be represented by open black squares. Solid blue markers will be referred to the population of *bad* events, whereas red lines will be used to describe the various cuts.

Cut on Chi Squares

As described in section §2.4.1, reconstruction of the particle trajectory can be obtained by applying different fitting procedures to the data. The fast nonlinear fitting algorithm is used in the following modes:

- All tracker clusters are used to determined the trajectory of the particle. A χ^2_{Fast} is given.
- Same algorithm is applied to the two half tracks built with first and second half. The corresponding half rigidities R_1 and R_2 are determined.
- The algorithm is applied neglecting multiple scattering effects. A χ^2_{NoMS} is given.

The χ^2_{Fast} and χ^2_{NoMS} distributions are plotted in Fig.3.4 as a function of the reconstructed rigidity. Monte-Carlo samples of Boron (left) and Carbon (right) ions are shown, together with the population identifying the *bad* events (blue solid markers). The χ^2_{Fast} and χ^2_{NoMS} distributions are both peaked at low values and show an extended tail at low rigidities. It is also apparent that it is difficult to characterize a high efficiency cut based on the chi squares. A loose rigidity dependent cut has been applied with the main purpose to eliminate low rigidity mis-reconstructed trajectories. As the dominant process is the multiple scattering, these cuts work in particular in the χ^2_{NoMS} distributions, whereas a very loose cut has been imposed on the χ^2_{Fast} distributions. All the events above the red lines are discarded.

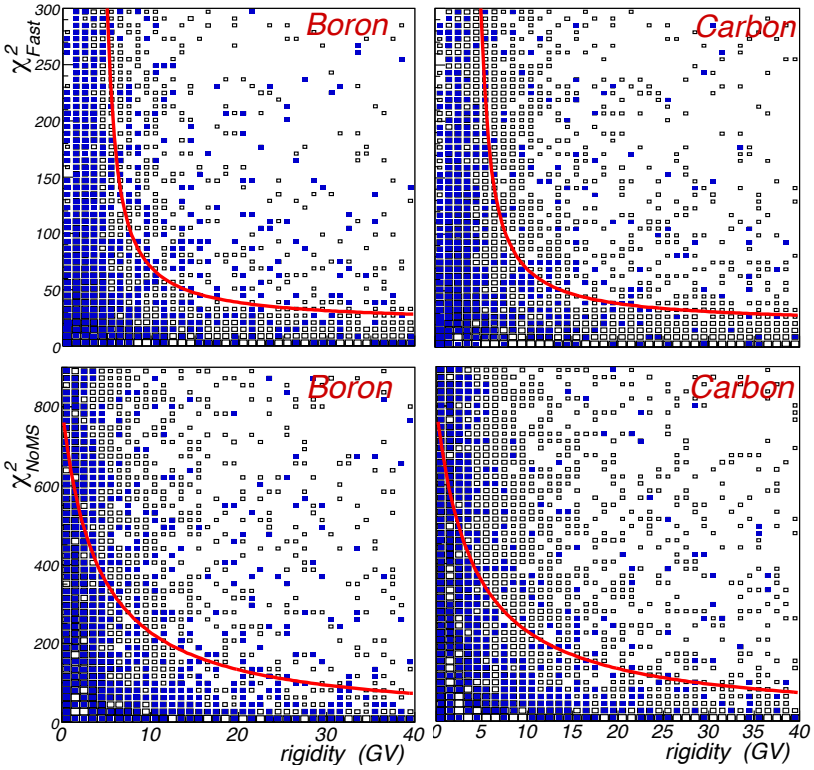

Figure 3.4: Distributions of χ^2_{Fast} (top) and χ^2_{NoMS} (bottom) as a function of the measured rigidity for Monte-Carlo samples of Boron (left) and Carbon (right). Blue solid squares indicate the $\delta R > 1$ population (*bad* events). Events above the red lines are discarded.

Cut on Half Rigidities

An important source of mis-reconstruction is the Coulomb scattering in the tracker material. Although the silicon tracker is very thin, it is possible for a single interaction in one of the six silicon planes to alter the particle trajectory so much to loose any information on the primary rigidity. Mis-reconstruction arises even without real scattering events, as the algorithm that determine the track can be confused by spurious or secondary hits. In order to identify events with bad rigidity reconstruction, a consistency check on the two half rigidities has been carried out.

As mentioned above, the full particle track is split in two half tracks each one containing hits from the three upper/lower layers[1]. Despite the rigidity resolutions of half-tracks is worse than for a complete one, large discrepancies between the two

[1] In tracks with less than 6 hits, those in the middle are shared to build the two half tracks.

half rigidities are a powerful criterion for detecting a change in the reconstructed trajectory. In a clean event, indeed, the two rigidity determinations R_1 and R_2 are compatible once the finite resolution effects are taken into account. In Fig.3.5, the

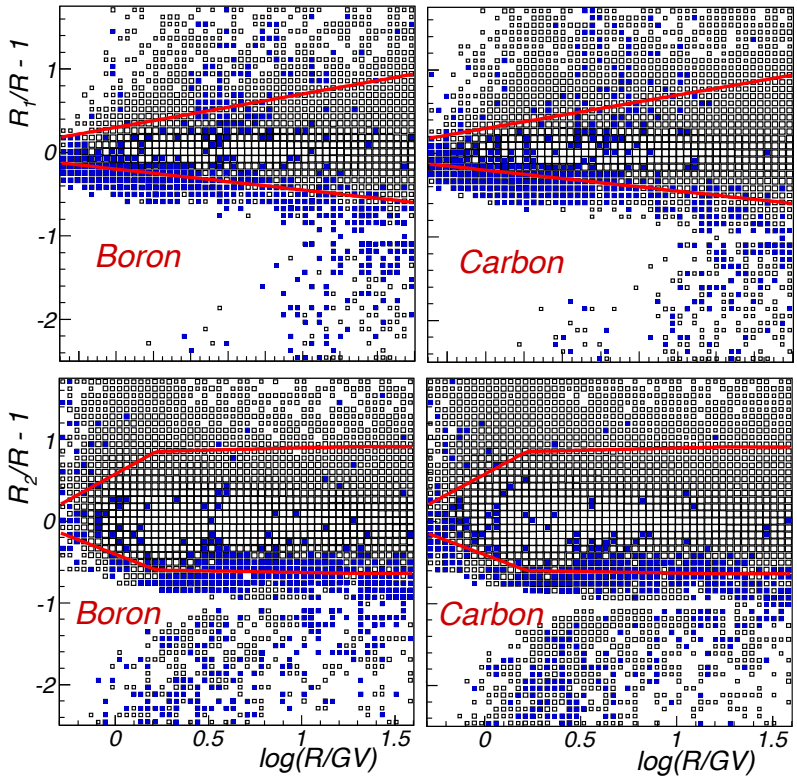

Figure 3.5: Distribution of the relative half rigidity ratios $(R_1 - R)/R$ (top) and $(R_2 - R)/R$ (bottom) as a function of the measured rigidity R for MC Boron (left) and Carbon (right) nuclei. Blue population marks the $\delta R > 1$ *bad* sample. Events within the red bands are selected.

ratios $(R_1 - R)/R$ (top) and $(R_2 - R)/R$ (bottom) are plotted as a function of the full rigidity R for Boron (left) and Carbon (right) MC samples. The distribution of *bad* events (blue) is superimposed. Charge-independent cuts have been applied to these quantities: all events ending out of the region defined by the red lines are discarded. One notices that *bad* events cluster at low R_j/R values, but higher R_j/R are also suspected as bad reconstructed particles. Hence symmetric cuts have been used. Multiple scattering contribution is clearly apparent, as distributions of the ratio R_2/R are broader than R_1/R which corresponds to larger integrated effect along the particle paths. It is also noticeable, in the lower regions of the plots, a population with $R_j/R < 0$ indicating two measured rigidities with different signs.

Beta-Rigidity consistency

For this analysis, the measurement of the time-of-flight of a particle is not strictly mandatory. For a given measured curvature and charge Z, the nuclear species and its momentum are identified and an additional β measurement might be thought as a redundant information[2]. Nevertheless, the relationship between β and R can be used. Since mis-measured particles are not supposed to obey a consistency among the two measurements, a simple and powerful compatibility criterion is provided by the relation that links the particle rigidity to its velocity:

$$\frac{1}{\beta} = \sqrt{1 + \frac{(mc^2/Ze)}{R^2}} \tag{3.3}$$

All nuclear species from Lithium to Oxygen lie along an ideal line defined by their

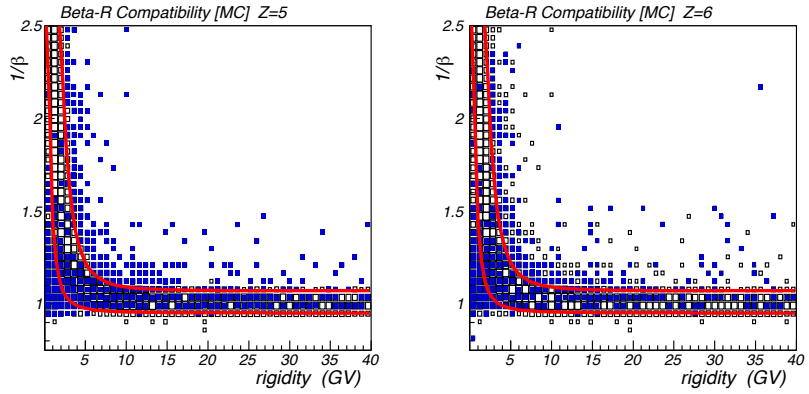

Figure 3.6: Consistency check between velocity and rigidity. The measured time of flight $1/\beta$ is plotted against the reconstructed rigidity for Boron (left) and Carbon (right) Monte-Carlo data. Well measured events are placed within the red bands that define the cut.

mass to charge ratio. It ranges between 2.2 for ^7Li up to 1.9 for ^{16}O isotopes, but this differences are not appreciable, because of the poor mass resolution of the instrument. Hence, a unique selection cut based on the β-R compatibility request has been applied as indicated in Fig.3.6. Only events lying within the band defined by the two red lines have been accepted.

It is apparent that most of poorly reconstructed events (blue markers) are gathered at low rigidity values or/and low velocities, i.e. events with wrong velocity and/or wrong reconstructed track. The cutting lines are defined with the aim to

[2]A time of flight measurement would be necessary in determining the particle masses. In this work the nuclear species is determined by the charge assignment, as explained in §4.

leave out this *bad* data stream. Actually the two measurements β and R are not strictly independent, as the velocity computation accounts for the particle inclination factor[3], which is mostly determined by the tracking. Furthermore, a reconstructed particle object is created if the extrapolation of the track matches fired TOF paddles.

Finally, it should be noted that this cut acts in different ways for different mass/charge isotopes, and, since the isotopic composition of CR nuclei is not well known and unmeasurable with AMS-01, it might be suspected that this $\beta - R$ selection would introduce an unavoidable bias in the selection. This is not the case; the last-cut distribution presented in next section (Fig.3.12) reveals that this cut has a loose effect in the bulk of the distribution but it is well efficient in avoiding mis-reconstructed particles. Nevertheless, the overall efficiency for different isotopic mixture is discussed in Section §5.5.1.

Cut on Missing Layers

A track is reconstructed from the coordinates built from the x and y signals of the six tracker planes, as a result of the pattern recognition algorithm.

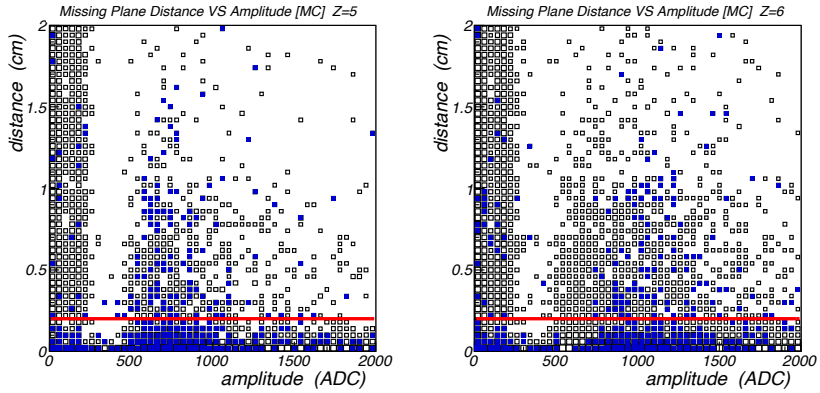

Figure 3.7: For each layer with no hit that belongs to the track, the distance from the closest neighbour hit and the track extrapolation is plotted as a function of the p-side cluster amplitudes. *Bad* events are correlated with missing hits within short distances. Events with missing hit distances smaller than 2 *mm* are discarded (red lines). These quantities are plotted for Boron (left) and Carbon (right) from the MC simulated data.

In all the reconstructed tracks with a number of hits less than six, signals on *missing layer* (namely silicon layers with no hit belonging to the track) have been investigated. The area close to the track extrapolations in the *missing layers* has been

[3] As the incoming particle is inclined, the effective path length is larger than the distance from the TOF planes.

explored with the aim to search for missing hits. Clearly, whenever a cluster is missed by the reconstruction algorithm, it might be argued that rigidity measurement is consequently distorted.

For each missing layer, the hit closest to the track extrapolation has been recognized, and its distance has been computed. In Fig.3.7 it is shown the distribution of this *missing distance* as a function of the cluster amplitude evaluated in the p-side (bending side). One notices that *bad* events are likely to be gathered near in the neighbourhood of the track extrapolation. A two millimeter window has then been defined as the minimum distance allowed to accept the event. It is also apparent that the amplitudes of such missing hits are well above the noise level, suggesting that they are non-spurious hits missed by the reconstruction.

3.2.5 Comparisons with Flight Data

A set of six cuts based on the quality of the track reconstruction has been presented. It can be summarized in these four points:

- Chi squares χ^2_{Fast} and χ^2_{NoMS} cuts;
- Half Rigidities R_1 and R_2 cuts;
- Velocity-Rigidity compatibility cut;
- Missing Layer cut;

In the previous section, these quantities have been examined only for Monte-Carlo data. Now a comparisons with flight data is done.
In the next figures (from Fig.3.8 to Fig.3.13), the same plots already discussed are shown as last cut for Boron (top) and Carbon (bottom), Monte-Carlo (left) and data (right). The explicit effect of each cut on the different sets of data is therefore apparent.
In should be noted that, whereas in MC data the particle identity (i.e. B or C) is exactly known, for the measured data it has been established by means of the charge identification algorithm that will be described in the next chapter.
Although its reliability on the charge discrimination power will be proved (§4.6) for the final selected data sample (i.e. the cuts under discussion here are included too) a reasonable purity is certainly achieved at the last cut level too[4]. In order to

[4] In general, an event with mis-measured track may be associated with a good charge assignation and vice versa, but common sources of both the mis-measurements may be fragmentation of primary nuclei or emission of secondary particles. This is one reason why, for data, it is more desirable look at the *last cut* population.

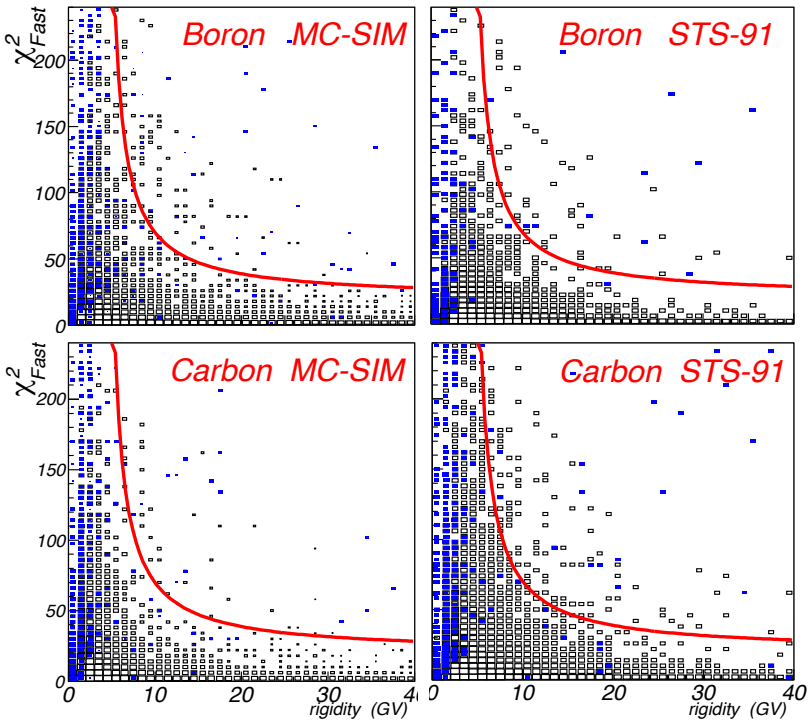

Figure 3.8: Distributions of χ^2_{Fast} as a function of the measured rigidity for Monte-Carlo (left) and measured data (right) of Boron (top) and Carbon (bottom) nuclei. Blue solid squares indicate the $R < 0$ population (*bad* events). Events above the red lines are discarded.

use only measured variables in these plots, a good indication of mis-reconstructed tracks can be gathered looking at distributions of negative rigidity particles. Indeed no anti-nuclei are expected in the $|Z| > 2$ detected sample[5] and the particle identities in Monte-Carlo data are exactly known. The $\sim 8,000$ events with negative rigidity detected out of $\sim 180,000$ downward-going particles are clearly linked to a bad rigidity determination (the *spillover*). This population, now representing the event stream classified as *bad*, is plotted, again, using solid blue markers.
In order to give a full understanding of their distribution among the kinematic quantities, these *bad* event sample is shown as *first cuts* (i.e. none of the above mentioned cuts is applied). Indeed only few of them (0 to 10, depending on the cut) would survive up to the last cut level (and after the application of all the cuts they are completely removed for B as for C) but to appreciate their distributions a suitable statistical sample is needed.
Comparing these distributions with those previously presented, it is clear that this

[5] A dedicated analysis proved that no heavy anti-matter is found in AMS-01 data [113].

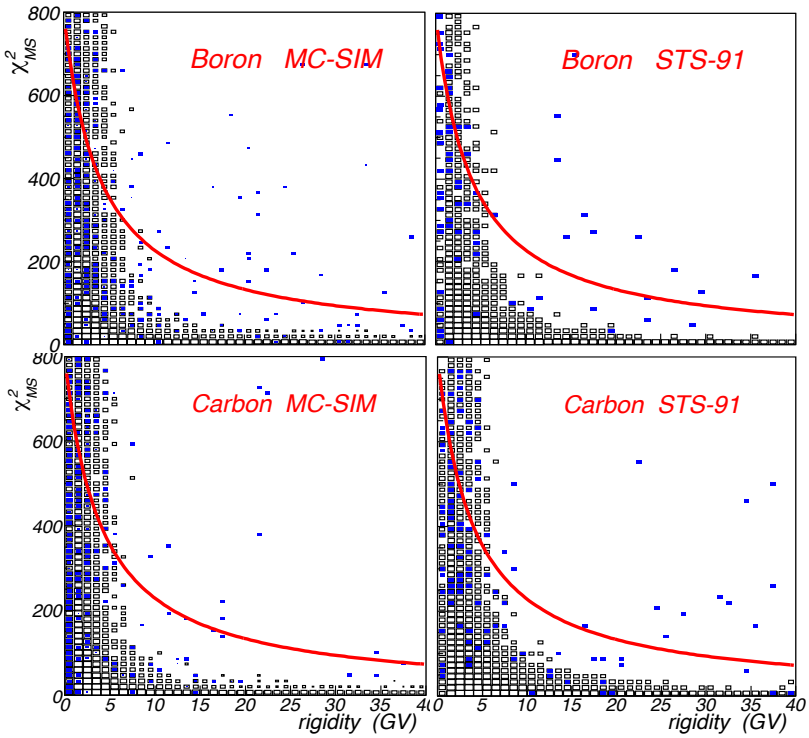

Figure 3.9: Distributions of χ^2_{NoMS} as a function of the measured rigidity for Monte-Carlo (left) and measured data (right) of Boron (top) and Carbon (bottom) nuclei. Blue solid squares indicate the $R < 0$ population (*bad* events). Events above the red lines are discarded.

$R < 0$ population well matches the previous $\delta R > 1$ event stream.

It is clear from Fig.3.8 the marginal effect of the χ^2_{Fast} cut on the distributions. Indeed it removes only ~ 200 events out of $\sim 45,000$ B and C nuclei detected from flight data. More effective is the cut on χ^2_{NoMS}, i.e. the cut on distributions where the multiple scattering in not accounted in the χ^2 computation. Fig.3.9 shows the χ^2_{NoMS} values plotted against the measured rigidity, for Monte-Carlo (left) and data (right) of Boron (top) and Carbon (right). High χ^2 events are indicator of particles that underwent large scattering angles; clearly the effect is rigidity-dependent, as multiple scattering becomes dominant for low momentum particles.
The cuts on half rigidities are shown in Fig.3.10 and Fig.3.11; their power in discriminating against the $R < 0$ events is clearly apparent. It should be noted that these cuts are shown as a function of log(rigidity), with rigidity ranging from 1.5 to $\sim 40\ GV$, as log-rigitity scale is much appropriated for many inspections involving CR data.

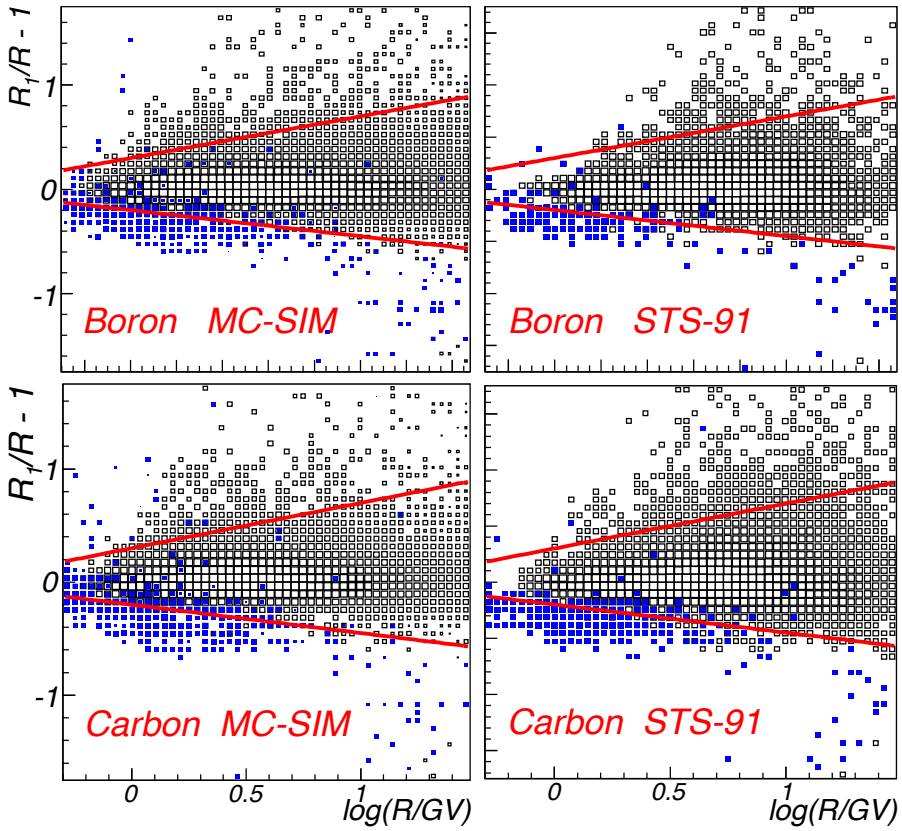

Figure 3.10: Half rigidity ratio $\frac{R_1}{R} - 1$ as a function of the measured rigidity R. Distributions for Monte-Carlo (left) and data (right) are shown for Boron (top) and Carbon (bottom) nuclei. Blue population marks the $R < 0$ *bad* sample. Events within the red bands are selected.

The β-R consistency request, as previously noticed, produces a quite slight effect on the measured data (Fig.3.12), as the bulk of last-cut events is well concentrated in the selection bands (red lines). This cut represents however a powerful criterion in rejecting mis-measured quantities.
The cuts on missing layers are illustrated in Fig.3.13, where the *missing distance* is plotted againts the corresponding hit amplitude for measured data and Monte-Carlo. Fig.3.14 shows the distributions of hit amplitudes versus the corresponding rigidity; red squares indicate the events removed by the cuts of Fig.3.13. It is interesting to note, explicitly from Fig.3.14, that removed events (red squares in the plots) are mainly those with high-charged missing hits, i.e. even the loss of a single good hit may cause a wrong sign assignment in the rigidity measurement.
A closer comparison between data and MC is made in the plots of Fig.3.15, Fig.3.16 and Fig.3.17 for the most important cuts. Cumulative distributions (from 1.5 to

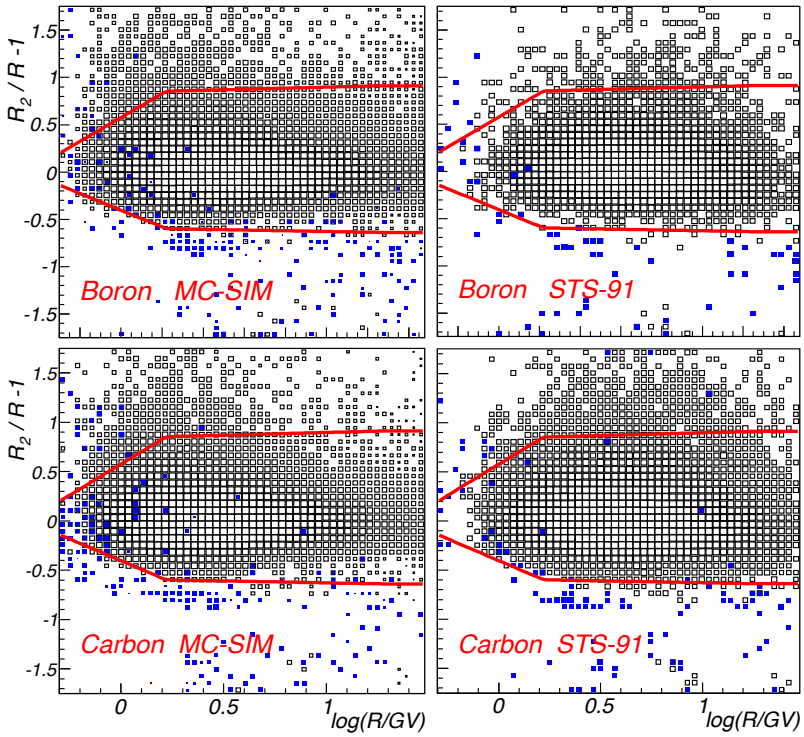

Figure 3.11: Distribution of the relative half rigidity ratio $\frac{R_2}{R} - 1$ as a function of the measured rigidity R for Monte-Carlo (left) and data (right) of Boron (top) and Carbon (bottom) nuclei. Blue population marks the $R < 0$ *bad* sample. Event within the red bands are selected.

40 GV) of χ^2's, half rigidities and missing distances are shown in the upper panels (colored plots). Measured data (solid markers) are superimposed with those from MC (solid line). Boron (blue) and Carbon (red) are also shown together in the same plots.

It is clear from Fig.3.15 (top) that the last-cut distributions of χ^2_{NoMS} are better described by the MC simulation than the χ^2_{Fast}'s, where the simulation exhibits smaller tails. This is a reason why the most effective cuts have been imposed to the former quantity.

It is also apparent from Fig.3.16 (half rigidities) the difficulty of the MC simulation in describing the tails of the $(R_j - R)/R$ distributions (upper panels).
It should be noted, however, that the observed discrepancies between MC and data in the single-ion distributions are not a relevant source of error for what concerns the final B/C measurement. In fact, the goal this if this analysis is the measurement

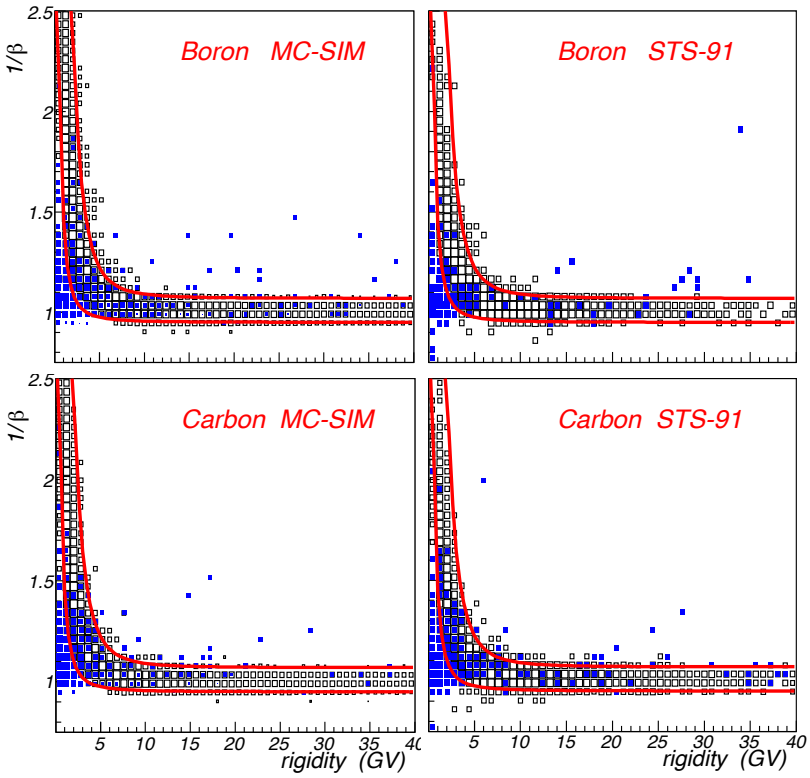

Figure 3.12: Consistency check between velocity and rigidity. The measured time of flight $1/\beta$ is plotted versus the reconstructed rigidity for Monte-Carlo (left) and data (right) of Boron (top) and Carbon (bottom) nuclei. Well measured events are placed within the red bands that define the cut.

of a ratio between the two fluxes. Thus, the relevant comparisons must be carried on the corresponding ratios.
This is shown in the lower panels of Fig.3.15 and Fig.3.16: the B/C ratio of the above distributions is plotted for measured data (black markers) and compared with simulated data (gray lines). A general good agreement DATA-MC is found. It should also be noted that these ratios are somewhat stable around unity, i.e. the MC description of the cut efficiencies has not effect in the B/C for the presented selection. Thus, any possible bias in the results is avoided.
Same conclusions can be stated for the missing-layer distributions, shown in Fig.3.17.

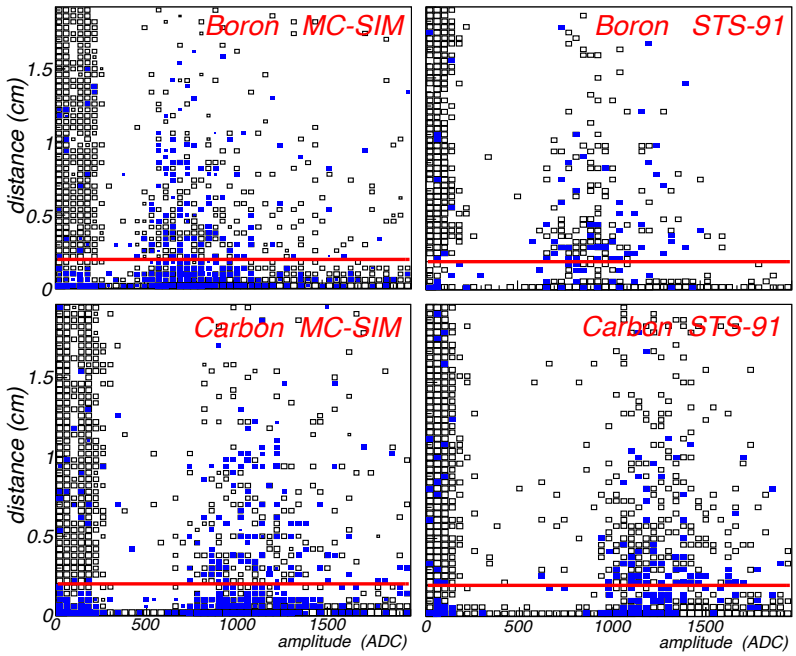

Figure 3.13: For each layer with no hits belonging to the track, the distance from the closest neighbour hit and the track extrapolation is plotted as a function of the p-side cluster amplitudes. Events with negative measured rigidity are correlated with missing hits within short distances. Events with missing hit distances smaller than 2 mm are discarded (red lines). These quantities are plotted for Boron (top) and Carbon (bottom) from Monte-Carlo (left) and data (right).

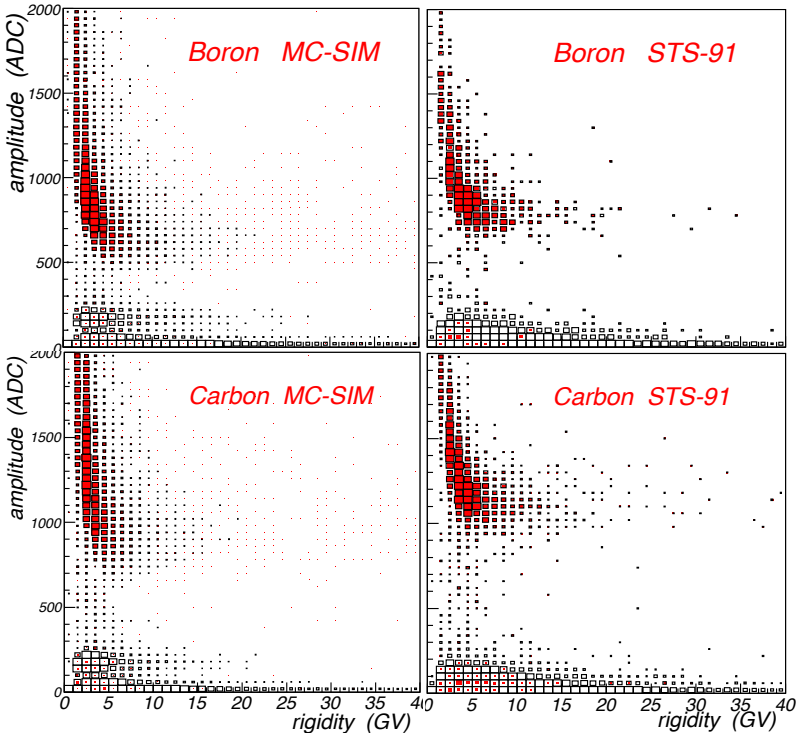

Figure 3.14: Missing hit amplitudes VS measured rigidity. For each layer with no hits belonging to the track, the p-side cluster amplitudes of the closest neighbour hits (to the track extrapolation) is plotted as a function of the measured rigidity. Events removed with the *missing layer cut* of Fig.3.13 are indicated as red squares. These events are mainly those with high-charged missing hits, i.e. the loss of a good hit causes a wrong rigidity measurement. These quantities are plotted for Boron (top) and Carbon (bottom) from Monte-Carlo (left) and data (right).

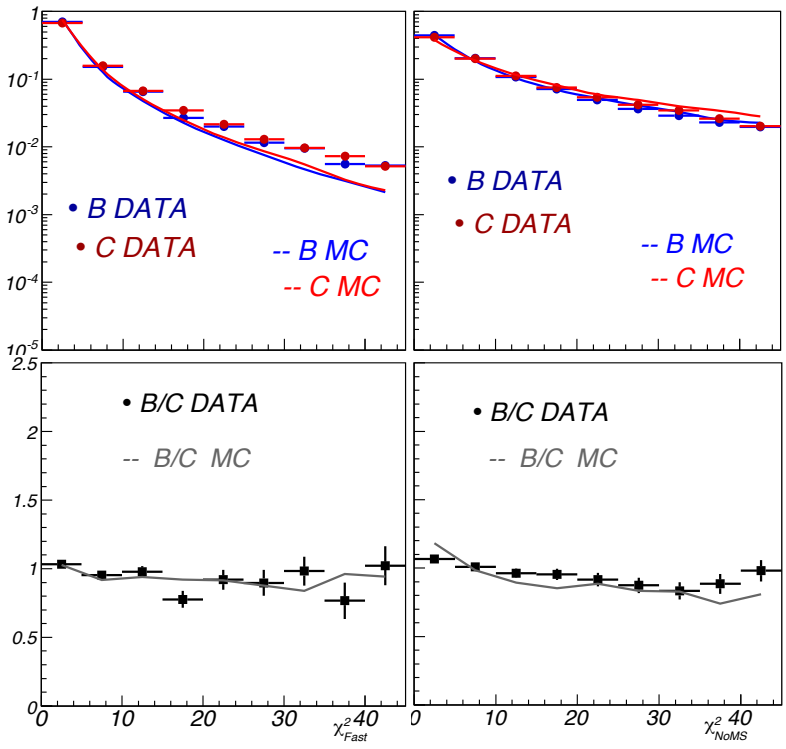

Figure 3.15: Top: distributions of χ^2_{Fast} (left) and and χ^2_{NoMS} (right). Monte-Carlo (solid lines) and measured data (full circles) are superimposed for Boron (blue) and Carbon (red) nuclei. Bottom: the ratio of above distributions for data (black squares) and MC (gray solid line).

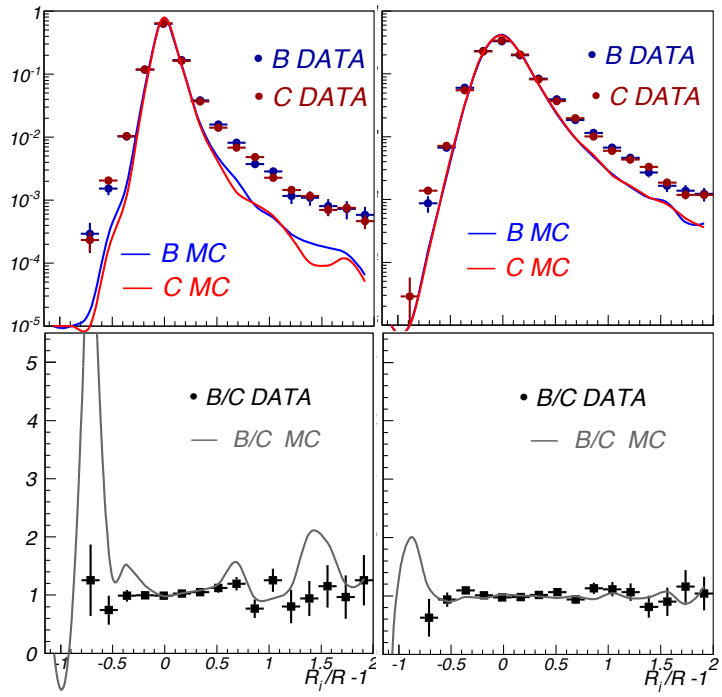

Figure 3.16: Top: cumulative distributions of the relative half rigidity ratios $\frac{R_1}{R} - 1$ (left) and $\frac{R_2}{R} - 1$ (right). Monte-Carlo (solid lines) and measured data (full circles) are superimposed for Boron (blue) and Carbon (red) nuclei. Bottom: the ratio of above distributions for data (black squares) and MC (gray solid line).

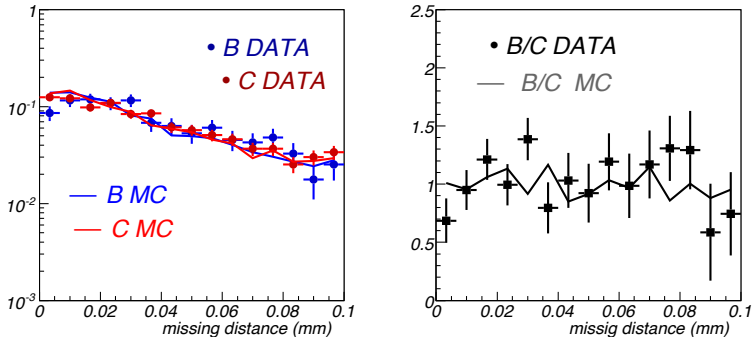

Figure 3.17: For each layer with no hits belonging to the track, the distance from the closest neighbour hit and the track extrapolation computed. Left: distribution of the *missing distance* Monte-Carlo (solid lines) and data (full circles) are superimposed for Boron (blue) and Carbon (red). Right: the ratio of above distributions for data (black squares) and MC (gray solid line).

3.2.6 Discussion

The cuts described above, developed with the help of a Monte-Carlo simulation for the detector reconstruction capabilities, remove all events whose kinematical parameters have been poorly determined. In Fig.3.18 the inverse rigidity distribution

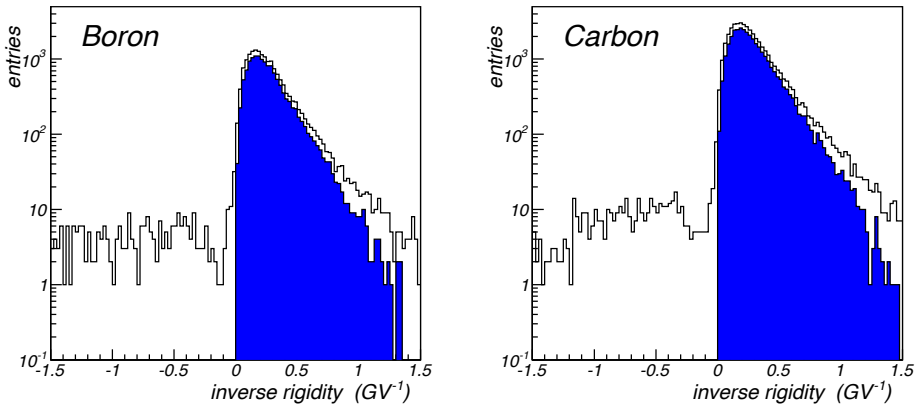

Figure 3.18: Inverse rigidity distribution before (black line) and after cuts (blue filled area) for events measured as Boron (left) and Carbon (right).

is reported before (black line) and after (blue filled area) the full selection. Intentionally, no requirement has been explicitly applied for the sign of the rigidity. The $R < 0$ events have been used as a control sample to estimate the effect of poorly reconstructed tracks or other background as secondary δ rays. Inverse rigidity is proportional to the track deflection, which is the measured parameter. The plot is made with Boron and Carbon nuclei detected from measured data. It can be notice that the initial $R < 0$ events are roughly uniformly distributed as a function of $1/R$; this suggests their random origin, namely from reconstruction failures. No Boron nor Carbon ions have been detected with $R < 0$ after the selection.

Selection efficiency for these cuts is shown in Fig.3.19, estimated with the Monte-Carlo as a function of the particle rigidity. The plots are made by applying cuts in the same order as presented in this section (a short list is reported in the panels). For each cut its efficiency curve is net of the overlying one, such that the last one applied (i.e. missing layer cut) expresses the overall efficiency of the whole selection. All cuts are net of the criteria exposed in the previous section, i.e. Paddle 10 of Layer 3 has been masked and only events within $\theta_{AMS} = 32°$ have been considered. A substantial uniform selection efficiency is observed after the full selection is applied, with similar behaviour for the two species. A sharp decrease at low rigidities (below $\sim 2\ GV$, corresponding to $\sim 0.4\ GeV/n$) is noticed, where a larger fraction

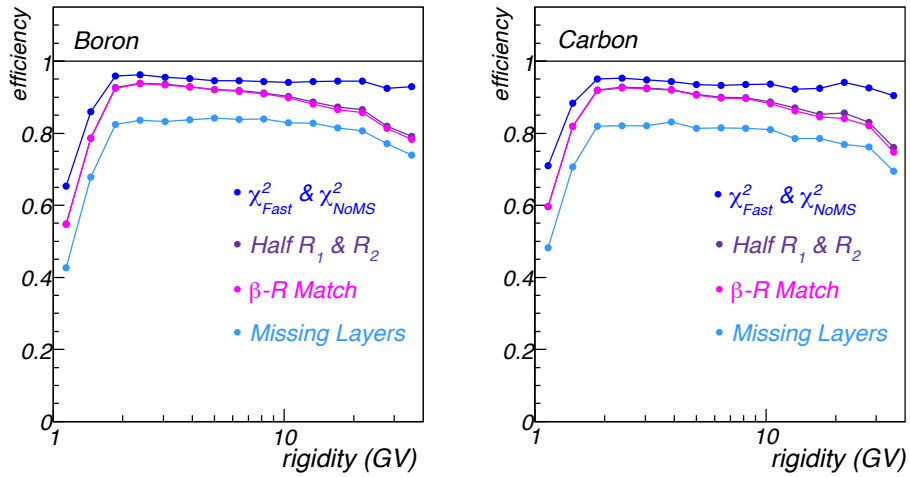

Figure 3.19: Cut efficiency as a function of rigidity for the tracking-based selection discussed in the text. The cuts are applied in the same order as listed and presented in this section. For each cut its efficiency is net of the overlying one, such that the last one applied (i.e. missing layer cut) expresses the overall efficiency of the selection. The left panel is referred to Boron, right to Carbon.

of charged particles underwent Coulomb scattering, i.e. the analysis cuts become more effective in that region. The slightly negative slope of the efficiencies reflects the worsening of the tracker resolution as the trajectory becomes more rigid.

For the determination of the differential energy spectra, and therefore the B/C ratio, the resulting measured rigidity distributions have to be be corrected for this efficiencies. Detector resolution, dead-time, inelastic interaction of CRs in the material and trigger efficiency will also be accounted for. All these issues are addressed in the next chapters.

3.3 Orbital Cuts

Finally global cuts dependent on the orbital conditions have been imposed to improve the quality of the measured data.
As described in section §1.3.2, the Earth magnetic field deflects charged particles and can prevent low energy nuclei from reaching the spectrometer. The minimal rigidity needed for a galactic cosmic ray to reach the spectrometer has been approximated by the Störmer vertical cut-off (§1.3.2), written as:

$$R_{VC} = \frac{M_0}{\mathcal{R}^4} \cos^4 \lambda \tag{3.4}$$

where λ is the geomagnetic latitude, $\mathcal{R}$ is the distance from the dipole center in terrestrial radii units and $M_0 = 15.0\ GV$ is related to the magnetic moment of the dipole. As the AMS-01 orbit spanned over all the latitudes within 51.7°, the cut-off rigidity value changed significantly during the orbit, from less than 1 GV in the higher latitudes, to nearly 15 GV along the magnetic equator. Thus, the fraction orbit at which a cosmic ray of given rigidity can reach the detector from outer space is a increasing function of rigidity, saturated at unity above $\sim 15\ GV$[6].

In this specific work there is no need to separate galactic component from trapped particles [111], as very few high Z nuclei are expected to be found sub-cutoff[7]. Since we are interested in measuring the ratio of the B and C galactic spectra a rejection of nuclei close to the cut-off has been performed with the aim to prevent the results from any charge/mass bias. Indeed, considering ion spectra in unit of kinetic energy per nucleon, the geomagnetic field introduces different distortions on the measured spectrum for different nuclear or isotopic species. In fact, during the AMS-01 orbit, only some geomagnetic regions were accessible by the detector for receaving CR particles in a given kinetic energy interval ΔE_{kn}; since the kinematic relation between R and E_{kn} is specified by the charge/mass ratio of the particle, the detector had different exposure for different isotopes.
On the other hand, the Störmer description (Eq.3.3) is a simplification of the real case.The spectrometer was not kept at fixed vertical directions during the flight, and its large aperture allowed detection of particles entering the detector with different inclinations. For these reasons a sharp, conservative, and orbit-dependent rigidity cut has been applied to the data: all the particle with rigidity smaller than $1.2 \cdot R_{VC}$ have been discarded. This criterion rejects a consistent fraction of data (nearly 30%).

[6] This *geomagnetic transmission function* will be derived in section §5.3 from flight data, as the fraction of time spent for each cut-off interval over the entire flight.

[7] Different case is for protons and leptons, which fill up the Van Allen belts.

In addition, as mentioned in Section §1.3.2, there are magnetic anomalies. The *South Atlantic Anomaly*, off the coast of Brazil, is a dip in the Earth's magnetic field which allows cosmic rays to reach lower altitudes into the atmosphere enhancing the particle flux. During the SAA crossing, the trigger saturated and the detector livetime could not be reliably calculated. Therefore, data collected above the SAA region have not been considered from the analysis. A geometrical cut on the geodetic coordinates has been imposed as shown in Fig.3.20

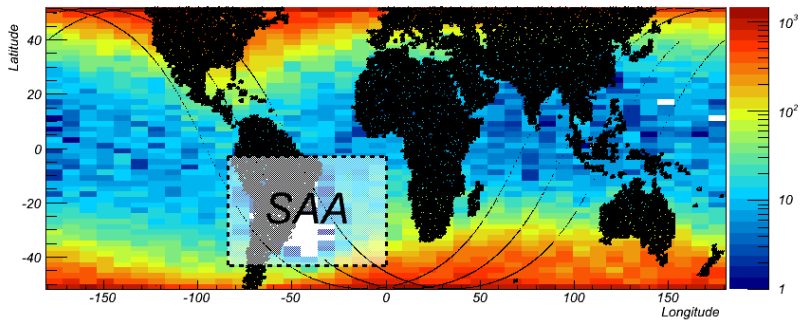

Figure 3.20: Distribution of CR events recorded by AMS-01 along the geodetic map. SAA exclusion region is defined by the white box.

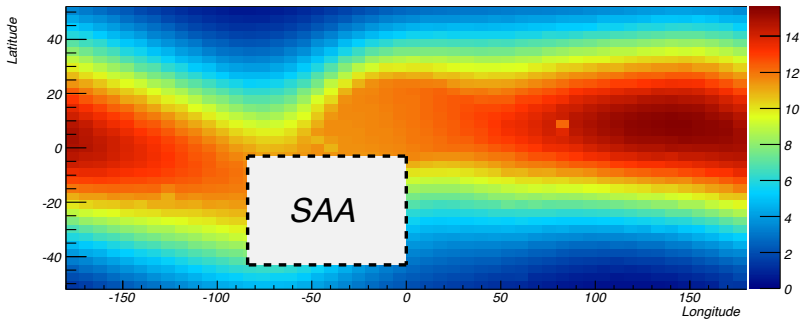

Figure 3.21: Value of the vertical Störmer cut-off plotted in the region covered by the STS-91 orbit. Depending on the geodetic coordinates, R_{VC} ranges from below $1\,GV$ (at high latitudes) to $\sim 15\,GV$ (along the equator). SAA data are excluded. It is interesting to note the anti-correlation between the CR rate (qualitatively from Fig.3.20) and the cut-off value.

3.4 The Shadow of the MIR Space Station

During the STS-91 mission, the space shuttle Discovery had a rendezvous with the MIR space station for about 4 days, while AMS-01 kept taking data. In the earlier AMS-01 data analysis, the data taken during the docking phase were excluded. Nonetheless, the effect of the MIR as a *source* of induced cosmic rays has been stud-

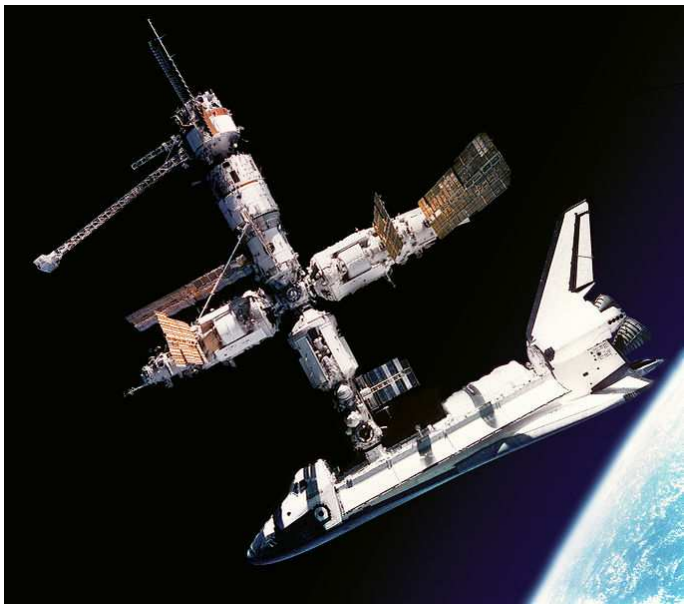

Figure 3.22: A shuttle-MIR rendezvous. This view of the Space Shuttle Atlantis docked to the Russian space station MIR was photographed by the MIR-19 crew on July 4, 1995. Cosmonauts Anatoliy Y. Solovyev and Nikolai M. Budarin, MIR-19 Commander and Flight Engineer, respectively, temporarily undocked their Soyuz spacecraft from MIR to perform a brief fly-around. They took pictures while the STS-71 crew, with MIR-18's three crew members aboard, undocked Atlantis for the completion of the joint activities. Figure courtesy of NASA and taken from [114].

ied and understood [115, 112]. This section presents a study of the effect of MIR as a *shield* for high charged cosmic rays. Indeed, the presence of the MIR space station in the AMS-01 field of view could affect the AMS-01 acceptance for Boron and Carbon. This study is interesting in itself and it is worthy of being discussed.

The arrival direction of a cosmic ray into AMS-01 $(\theta_{AMS}, \phi_{AMS})$ is determined to better than a degree. Here θ_{AMS} and ϕ_{AMS} are the azimuthal and the polar angle in the detector reference frame, referred to the first tracker layer, as computed by the fitting algorithm. To define an absolute direction (e.g. right ascension and declination), the major source of uncertainty is the shuttle's orientation, given by the knowledge of the flight attitude angles *yawn*, *pitch* and *roll* (§2.5.1), but in this particular case the two systems AMS-on-shuttle and MIR were co-moving together

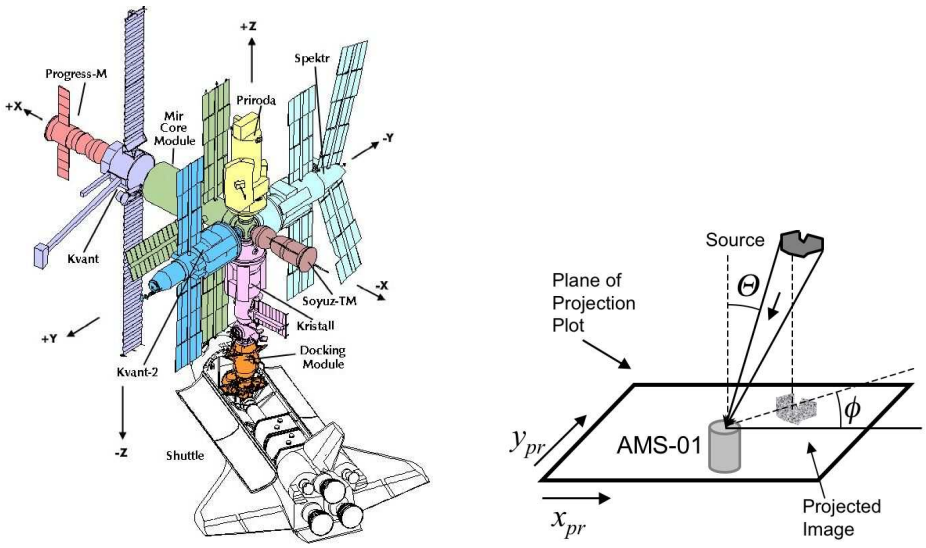

Figure 3.23: Left: the space station MIR and the shuttle are shown in a docked position. The distance from the top of the *Priroda* module to the shuttle payload bay is 30 m. The figure is to scale. Note that there is a non-zero angle between the shuttle x-axis and the *Mir* x-axis. Right: schematic explanation of the projection plots that are discussed in the text. Figure courtesy of NASA [104].

as a unique body, i.e. the space station was *seen* by the spectrometer as a fixed object. The part of MIR which entered in the AMS field of view consisted in some large modules ($\sim$ meters) located at close distances ($\sim$ 10 meters). Hence it should be possible to detect with high precision the influence of the large space modules in the cosmic ray flux rate and composition.
This task has been performed by recording the arrival directions of cosmic rays according to their projections on the (X_{pro}, Y_{pro}) plane, i.e. the way used by a common photocamera for creating an *image*, as sketched in Fig.3.23 (the right panel). The projection of the arrival direction onto a perpendicular plane (X, Y) is defined by the transformations:

$$X_{pr} = -\sin\theta\cos\phi \quad (3.5)$$

$$Y_{pr} = +\sin\theta\sin\phi \quad (3.6)$$

This study considers downward-going events. The projection plot on the left in Fig.3.24 indicates particles that have measured $Z > 2$ during the MIR docking phase. On the right panel the same projection plot is done for events collected after docking. It is clearly visible a depletion of events from a specific region in the MIR docking phase. It is interesting to note that, in the same region, an excess in the $|Z| = 1$ channel was observed [115]. This excess, shown in Fig.3.25, was due to secondary $\mu^{\pm}$ and $\pi^{\pm}$ produced by interactions of protons, helium and heavier nuclei

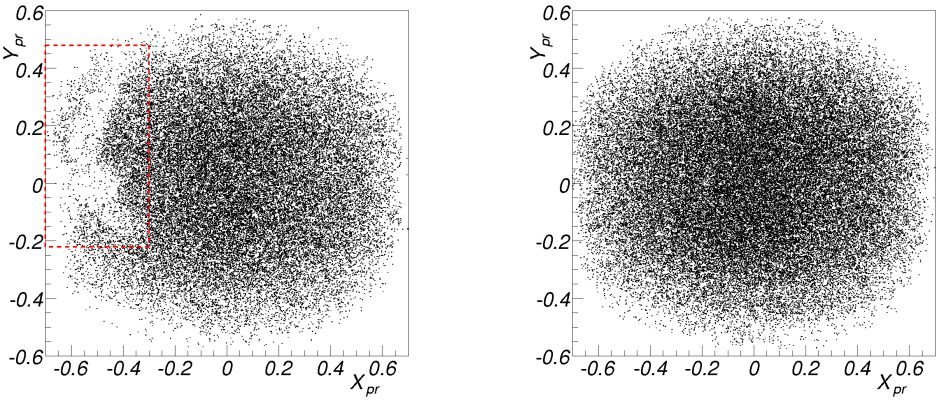

Figure 3.24: Projection plots of downward-going $Z > 2$ particles collected by AMS-01 during the MIR docking phase (left) and after docking (right). A relative depletion in the flux is clearly visible on the upper-left side of the MIR docking data. The left plot has 45000 events, corresponding to about 40% of the used data.

(i.e. *missing nuclei* of Fig.3.24) with the MIR modules. In Fig.3.26 the shadow is

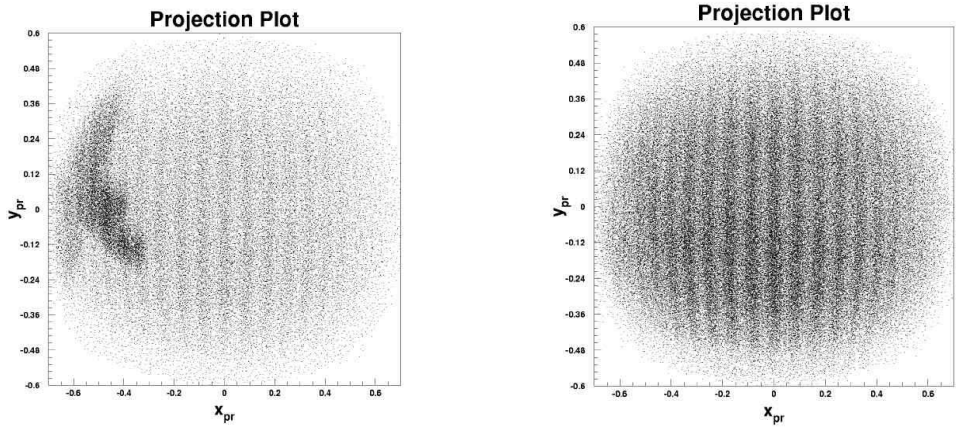

Figure 3.25: Projection plots of downward-going $|Z| = 1$ particles collected by AMS-01 during the MIR docking phase (left) and after docking (right). A relative excess in the events collected from MIR docking phase was found (left) and attributed to secondary cosmic rays (i.e. $\mu^{\pm}$ and $\pi^{\pm}$) induced by the presence of the MIR space station in the detector field of view[115].

compared with a picture of the MIR, taken in a previous rendezvous mission from a similar location as AMS-01 was placed. The correspondence between the two images is noticeable. Modules *Priroda*, *Kvant-2*, *Spektr*, and the *Soyuz* vehicle are recognizable in the data halo. It is also noticed that the solar panels had a little shadowing effect.

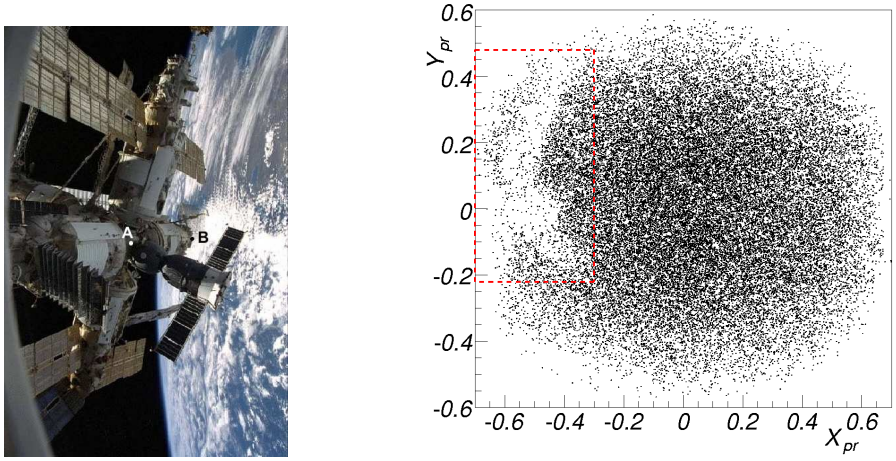

Figure 3.26: Left: MIR as seen from a porthole in a SpaceHab module during STS-89. Visible are the *Spectr* (pointing upward), *Priroda* (pointing to earth), *Soyuz* (pointing to right), *Kvant-2* (pointing down), and *Kristall* modules [115]. The picture is compared with the projection plot (right) described in Fig.3.24 to indicate the correspondence between the shadow and the modules' profiles.

In principle the intensity of this depletion may be different for Boron and Carbon nuclei, due to different interaction probabilities in the MIR modules, hence the B/C measurement is potentially affected by the data collected during this period. On the other side, once the region is identified, it is also clear that particles coming from MIR can be excluded by a simple geometric cut, as indicated from the dashed box in Fig.3.24. Since a cut on θ_{AMS} has been also imposed to the data (§3.2.3), part of the box is already excluded by the detector selection. This remaining cut reduces the geometric acceptance of only $\sim 5\%$, with exactly the same factor for Boron and Carbon. This cut allows to include in the analysis all the other data collected during the docking phase, that are a consistent fraction of the used data (41%).

Finally, events coming from the pre-docking phase have been also removed. During this phase, a different version of trigger was implemented in AMS-01 (§2.3) A tracker-based trigger condition provided a fast evaluation of the particle's sagitta and was used to removed low rigidity particles. The last phase, when AMS-01 was pointing to the Earth, must also be excluded for any study of galactic CRs. This cut turned to be not necessary: after the whole selection applied, no $Z > 2$ events are found during this *albedo* phase.

3.5 Summary

In this chapter a thorough description of the data selection have been presented. Various cuts have been implemented with the goal of obtaining a clean sample of CR nuclei. This sample has been be used as a basis to compute the galactic energy spectra and derive the B/C ratio. The most important source of mis-reconstruction is multiple scattering, that may alter the particle trajectory. Inelastic collisions may also be cause of undesirable events. Measurement of ions is also affected by a large amount of δ-rays, that can leave the silicon and produce secondary tracks. High Z events are therefore accompanied by many clusters and tracks.
Moreover, global cuts depending on the orbital conditions have been described. The orbit-dependent rigidity selection will be further discussed in Section §5.3 for the determination of the detector exposure time. An overview of all these cuts is given in Table 3.1; for each selection cut, the number of events which passed all the cuts are reported in the table. The columns indicate the whole preselected sample, nuclei detected as B and as C. The next chapter describes the charge reconstruction

SELECT	**DATA**	**Boron**	**Carbon**
Z>2 selection	232035	25888	62508
$\beta > 0$	181612	20253	49596
$\theta_{AMS} < 32°$	156315	17364	42814
Bad TOF Paddle	155965	17352	42800
χ^2_{Fast}	152096	16956	41754
χ^2_{NoMS}	136636	15788	39080
Half R_1	130490	15139	37526
Half R_2	122666	14365	35843
$\beta - R$ Match	121275	14232	35637
Missing Layers	96017	13572	33905
No Pre-docking	86815	12248	30603
No Albedo	86815	12248	30603
Geomagnetic cut	61339	8899	21838
No MIR Shadow	59288	8587	21142

Table 3.1: Selection summary table. Value shown is the number of events which passed all the analysis cuts above it in the table. These values are reported for the whole data sample and for events detected as Boron and as Carbon.

algorithm implemented to identify B and C nuclear species.

Chapter 4

Particle Identification

In this chapter the algorithm for the particle identification is presented. In the view of the B/C ratio measurement, the algorithm has been optimized for all the nuclear species ranging from Lithium (Z=3) to Oxygen (Z=8). The particle identification procedure has been performed by means of Z reconstruction. The mass number A was not directly measurable by AMS-01 for $Z > 2$, i.e. different nuclides belonging to the same isotopic family are indistinguishable. This uncertainty on the isotopic composition involves some consequences for this analysis that will be discussed in the next chapters.
In this work the charge of each nuclear species is determined by the energy losses recorded in the silicon layers of the tracker. The ionization charge generated by a charged particle in a silicon micro-strip detector is collected in a cluster of adjacent strips. Tracker clusters were recognized on-line an then re-processed with the reconstruction software.

A multi-step procedure of equalization of the cluster amplitudes is presented in the next sections. The method accounts for electronic response, saturation effects, particle inclination and velocity dependence. The charge identification algorithm, applied to the corrected signals, is then described in detail and the influence of charge contamination on the B/C ratio is finally discussed.

4.1 Energy Loss of Nuclei

Charged particles traversing the detector material loose energy by means of collisions with the atomic electrons. The amount of energy transferred in each collision is generally a very small fraction of the particle primary energy, but sufficient for its detection. When enough energy is transferred to the electron to detach it from the nucleus, it can cause secondary ionization in the material as δ-ray. The average rate

of energy loss (or stopping power) by a charged particle in matter generally depends on the properties of the particle and the material. This quantity is usually presented in path length units x (mass per unit area). Its theoretical description is known as the Bethe-Bloch (BB) formula [116] and reads:

$$-\left\langle \frac{dE}{dx} \right\rangle = K \frac{Z_m}{A_m} \frac{Z^2}{\beta^2} \left[\frac{1}{2} \ln \left(\frac{2m_e c^2 \beta^2 \gamma^2 T_{max}}{I^2} \right) - \beta^2 - \frac{\delta}{2} - \frac{C}{Z_m} \right] \tag{4.1}$$

where:

$K = 4\pi N_a r_e^2 m_e c^2$ ($\sim 0.31 MeV cm^2$)	Z = charge of incident particle
A_m = atomic mass of medium	C = shell correction factor
Z_m = atomic number of medium	N_a = Avogadro's number
T_{max} = max energy transfer per collision	m_e = electron mass
δ = density effect correction	r_e = classical electron radius
I = mean excitation energy	β = particle velocity

The maximum energy transfer is that produced in a head-on collision, $T_{max} \approx 2m_e c^2 \beta^2 \gamma^2$. The Bethe-Bloch formula shows a clear dependence of the energy loss on the traversing particle energy and charge. The MIP value ($\beta\gamma \sim 3.5$) separates two domains (see Fig.4.1): in the non-relativistic domain the dominant dependence is in β through the $1/\beta^2$ term; at higher $\beta\gamma$ values the energy loss increases quite weakly (relativistic rise). At more higher energies (above some TeV) radiative effects becomes to be important. Due to asymmetric fluctuation in the energy deposits, the most probable energy-loss in a detector is generally below the mean given by Eq.4.1. For thin absorbers, the energy loss probability distribution is adequately described by the Landau-Vavilov distribution [117, 118]. The charge of particles measured during the AMS-01 mission is determined through the energy deposited in the four scintillator paddles of the TOF system (up to $Z = 2$) and the up to six silicon layers of the tracker (up to $Z = 8$) (§2.4.1). Even though silicon detectors are thin ($300\mu m$), the number of collisions of a traversing nucleus and its energy deposition are large enough to treat its energy-loss distributions as gaussian for $Z > 2$.

4.2 Preselection

As discussed in Section §3.1, the search for light nuclei starts with a $Z > 2$ preselected sample. This first determination of the particle charge was performed by the standard reconstruction algorithm, described in Section §2.4.1. Since it was optimized for protons and helium nuclei identification [107, 110], the charge separation achieved is good enough for discriminating the $|Z| \leq 2$ sample from higher

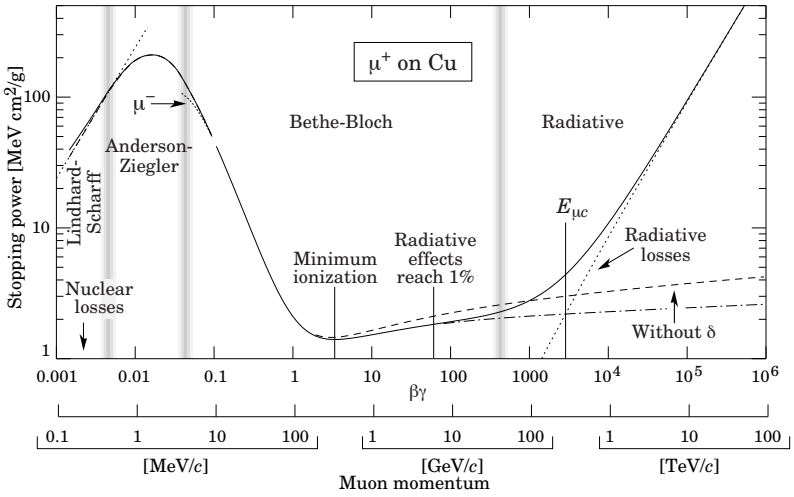

Figure 4.1: Stopping power $\langle dE/dx \rangle$ for positive muons as a function of $\beta\gamma = p/Mc$ over nine orders of magnitude in momentum (solid curve). Region between the 2^{nd} and the 3^{rd} vertical bar is the range of interest as discussed in the text.

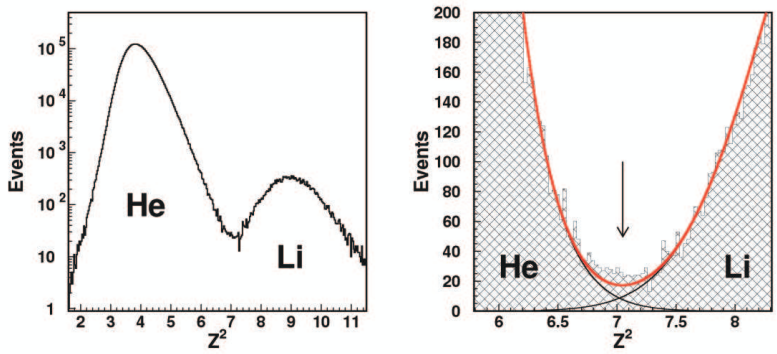

Figure 4.2: Charge separation provided by the tracker. The large helium sample contributes only marginally to the $Z > 2$ selection. Contamination to Lithium is estimated to be less than 3.1^{-4} of the Li sample [113].

charged ions. Indeed, $Z > 2$ data are well separated by heavier nuclei, thanks to the sound combination of information of TOF and tracker (§2.4.1). Previous studies [113] pointed out that contamination of He in the $Z > 2$ sample was estimated to be less than 3.1×10^{-4} of the Li sample, whereas the contamination from protons is completely negligible [110], so that no background is expected in Boron and Carbon channels. In fact, neither B nor C candidates are found in the deselected $Z < 3$ sample[1]. The dynamic range of the TOF scintillators does not permit to distinguish

[1] This check was done *a posteriori*, applying the present charge ID algorithm to the helium sample that was excluded at the preselection level.

higher charges with great accuracy [119]. Therefore, only the information from the silicon tracker has been taken into account for charge measurements.

4.3 The Equalization Procedure

The specific goal of this investigation is to provide the best possible relationship between the cluster characteristics and the mean energy-loss deposited by charged particles in the silicon.
The mean energy deposition by a charge Z with velocity β is described by Eq.4.1. Due to energy-loss fluctuations and broadening of the apparatus responses, the most appropriate way to describe the measured dE/dx distribution is by means of a set of probability density functions $P^Z(A)$, being the quantity A the best information that can be inferred on the particle energy loss on the basis of measured quantities.

Clearly A is related to the cluster *amplitude* α, defined as the sum of the cluster strip signals (α=$\sum_i S_i$). It is also clear that the most general relation between the intrinsic energy-loss and the readout signal involves other instrumental and physical effects. In particular, the following dependencies will be explored in this section:

- Impact point η. Since each silicon sensor is basically *sampled* by an array of implanted strips, the ionization charge collected by the strips in general depends on the point where the particle produces the deposit.
- Inclination θ. The total amount of energy deposition must be normalized to the effective path-length.
- Electronics response κ. Electronic devices that convert the physical signal into a readout pulse are characterized by specific gains (in the linearity range) and possible saturation (deviation from linearity).
- Velocity β. It is clear from Eq.4.1 that the energy-loss is velocity dependent.

The most general parametrization adopted to describe A is then:

$$A \equiv A(\alpha, \eta, \beta, \theta, \kappa) \tag{4.2}$$

being α the raw cluster amplitude as readout from the devices. Since at first approximation $A \sim \alpha$, the starting point is to express the effective amplitude as:

$$A = \alpha \cdot f(\alpha, \eta, \beta, \theta, \kappa) \tag{4.3}$$

where in general non-linear effects preserve a residual dependence of f from α.
The next sub-sections are devoted to establish the role of η (impact point), θ (inclination), β (velocity) and κ (chip number) in the relation between dE/dx and α by

means of the construction of the effective amplitude function $A \equiv A(\alpha, \eta, \beta, \theta, \kappa)$. A heuristic approach will be adopted in the exposition, as it was the iter actually undertaken in this study.

4.3.1 Tracker Clusters Selection

In order to ensure full energy collection, other strict requirements are imposed to the clusters of the reconstructed track. This selection is based on their morphology and the quality of their channels. The following criteria have been requested to the clusters:

- located far from the silicon wafer border;
- not containing dead strips or hot strips (see caption on Fig.4.3);
- containing more than one strip.

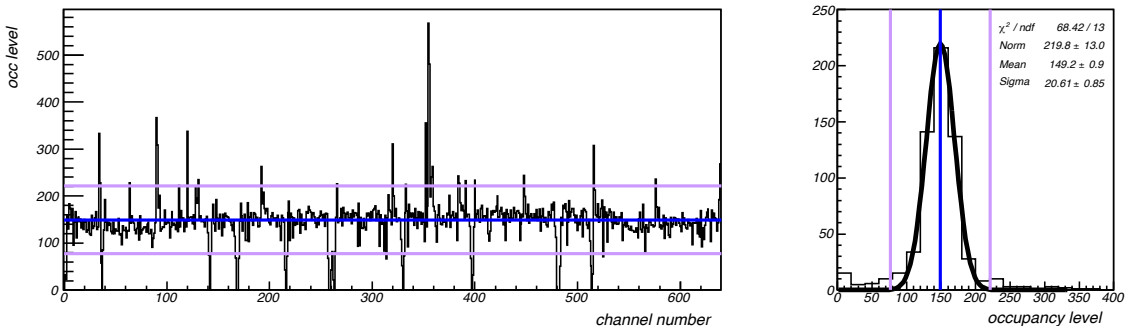

Figure 4.3: Channel occupancy distribution in Ladder `L4S7H1`. Left: occupancies N_L for all the 640 p-side channels from the $Z > 2$ data collected during the flight. Mean occupancy level μ is represented by the blue middle line. Channels with occupancy above (below) the upper (lower) purple line are declared *hot* (*dead*). Right: cumulative occupancy distribution from the same ladder.

Clusters which do not satisfy the above criteria are marked as *bad* and removed for the charge reconstruction procedure. A list of bad strips has been determined with a global study of the channel occupancy: for each ladder and side, strips which show an abnormally low or high response frequency were tagged as dead and hot strips. The occupancy level in a given side is defined as

$$OL^j = \frac{N_L^j - \mu_L}{\sigma_L} \tag{4.4}$$

where N_L^j quantifies how many times channel j triggered a cluster, μ_L and σ_L are the mean and RMS occupancy values of ladder L. Channel j is declared *bad* if its

occupancy level is $OL^j < -3.5$ (dead) or $OL^j > 3.5$ (hot) and clusters containing bad channels are declared bad clusters and ruled out. After this selection, events with at least three good clusters are used.

4.3.2 Impact Point Dependence

Due to the geometry of the strip implantation scheme on the ohmic side of the silicon sensors (n-side), the total collected charge on the readout strips turned out to depend on the impact parameter η. For two-strip clusters, it is defined as:

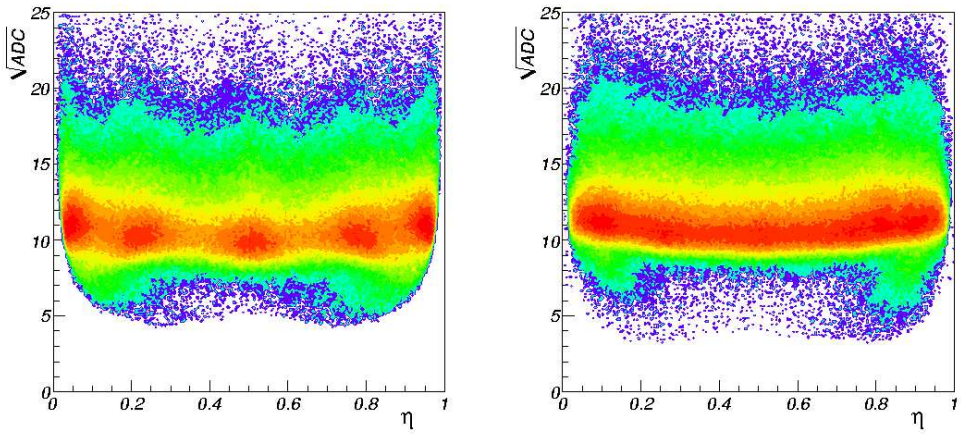

Figure 4.4: Charge amplitude of the n-side (left) and p-side (right) clusters as a function of the impact parameter η observed for Helium ions. The charge loss and the peaked η structure are clearly visible for the n-side signals, whereas a more uniform behaviour of charge collection id observed in the p-side.

$$\eta \equiv \frac{x - x_i}{x_i - x_{i-1}} \tag{4.5}$$

where x_{i-1} and x_i are the coordinates of the two contiguous strip and x is the impact point. Due to the strips capacitive coupling, an approximation of the impact parameter can be derived for the clusters center of gravity:

$$\eta \sim \frac{S_{right}}{S_{left} + S_{right}} \tag{4.6}$$

where S_{left} and S_{right} are the signals of the leftmost and rightmost strip respectively. In principle, this dependence can be extended to clusters with more strips and parametrized with an effective function. The total cluster amplitude can be corrected accordingly.

For ion data, with high charge depositions and inclined tracks, this statistic procedure turned out to be not necessary on the junction side (p-side), characterized by a smaller implantation pitch. On the other side, inefficiencies in charge collection persists in the n-side, making an inconsistent relation between energy deposition and cluster amplitudes[2]. In addition, it should be noted that the n-side signals do not provide a true independent information on the charge with respect those observed in the p-side. Hence it was decided to use only the p-side information to obtain the charge:

$$A(\alpha, \eta, \beta, \theta, \kappa) \equiv A(\alpha, \beta, \theta, \kappa) \tag{4.7}$$

4.3.3 Electronics Response

The first correction to the readout values involves the response of the front-end electronics. A signal, after passing the decoupling capacitor, is fed into a VA_{HDR}

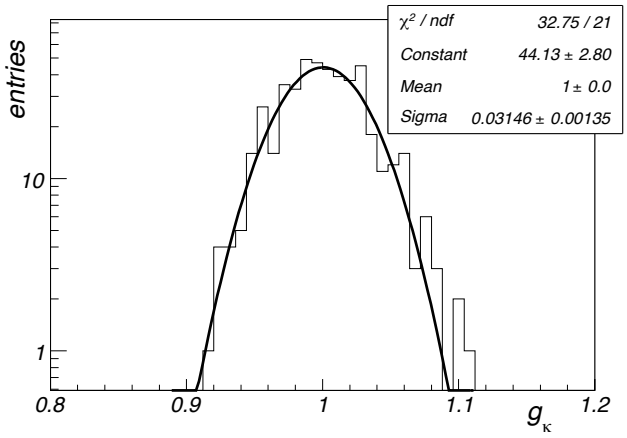

Figure 4.5: Distribution of the g_κ factors to be applied to the raw clusters amplitudes. A dispersion of $\sim 3\%$ has been found.

chip [120]. Each chip reads 64 read-out channels. After signal shaping and sampling, the chip is sequentially read out by means of an analog multiplexer and digitized by the Tracker Data Reduction (TDR) boards, placed outside the magnet in the electronic crates. For an ideal detector, the same responses are supposed to come from all the devices. In the real case, in general, different chips have different gains, and a equalization to a given reference amplifier has to be applied to the readout

[2] The interstrip charge collection in the n-side has been improved in the AMS-02 silicon tracker, where a new bonding scheme has been designed.

response:

$$A(\alpha, \beta, \theta, \kappa) = g_\kappa \cdot \alpha \cdot f(\alpha, \beta, \theta) \tag{4.8}$$

The factor g_κ, to be applied to a cluster observed in the κ-th chip, is defined as $g_\kappa = \frac{\langle \alpha_{k_R} \rangle}{\langle \alpha \rangle}$ and the κ_R index indicates the chip used as reference.
As shown in Fig.4.5, the g_κ distribution is approximately gaussian with $\sigma \approx 3\%$. This factor equalizes all the raw amplitudes α to a same common level α_{k_R}. This correction factor can be reasonably considered independent on Z, β and θ.

4.3.4 Particle Inclination

The individual measurements have to be corrected for different path-lengths in the silicon by means of a correction for the particle inclination. The effective cluster amplitude then becomes:

$$A(\alpha, \beta, \theta, \kappa) = |\cos\theta| \cdot g_\kappa \cdot \alpha \cdot f(\alpha, \beta) \tag{4.9}$$

being θ the incidence angle of the particle, determined by the track reconstruction. The product $|\cos\theta| \cdot \alpha \equiv \alpha_V$ is the reference value for vertical downward-going particles.

4.3.5 Velocity Dependence and Signal Saturation

Particles have been measured with β values as low as $\beta = 0.4$. Because of the β dependence of the energy deposition (see Eq. 4.1) a charge independent correction has to be taken into account. For a large number of energy deposits from a given charge Z, the expected functional behaviour should be indicated as:

$$\langle |\cos\theta| \cdot g_\kappa \cdot \alpha \rangle \propto BB(Z, \beta) \tag{4.10}$$

where the LHS is the best estimation so far of the mean energy-loss and $BB(Z, \beta)$ is the $\langle dE/dx \rangle$ expressed in Eq.4.1. Since saturation effects become important for low β or high Z, the measured energy deposition does not simply depend on β as predicted, and it is observed to be charge dependent. Indeed a parametrization $f = f(\alpha, \beta)$ had been hypothesized for A. Two distinct effects may generate a loss of linearity between the mean cluster amplitude and $BB(Z, \beta)$:

- since the on-line data reduction system considers at most five adjacent strips to build a clusters, it might be argued that some charge information get lost if the real cluster length is greater than five channels;
- for large energy depositions, the strips with the highest signal exceed over the dynamic range limit.

As a consequence, the deviations from the expected behavior should be only function of the collected charge. Hence, introducing some correction $b(\alpha)$ for the saturation, the following relation:

$$\langle b(\alpha) \cdot |\cos\theta| \cdot g_\kappa \cdot \alpha \rangle \propto BB(Z, \beta) \tag{4.11}$$

should be realized. Thus the $f(\alpha, \beta)$ that appears in Eq.4.9 can be modified into $b(\alpha)f(\beta)$ and a conclusive expression for A can be established:

$$A(\alpha, \beta, \theta, \kappa) = |\cos\theta| \cdot g_\kappa \cdot \alpha \cdot b(\alpha) \cdot f(\beta) \tag{4.12}$$

where the β dependence is now reduced to a is a unique functional behaviour to be determined as well as $b(\alpha)$.

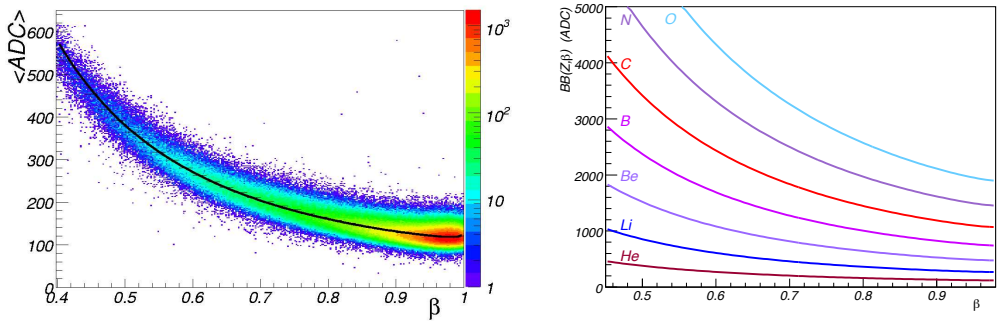

Figure 4.6: Left: Bethe-Block fit on Helium data from the flight. Right: functions $BB(Z, \beta)$ as obtained from He data and extrapolated up to Oxygen.

In order to obtain a phenomenological description of this effect, the following procedure has been conceived and carried out:

1. Determination of $BB(Z = 2, \beta)$ relation with helium data.
2. Building $BB(Z, \beta)$ functions for heavier nuclei ($Z = 3 \div 8$).
3. Comparisons with data.
4. Determination of the saturation function $s(\alpha)$.
5. Saturation and velocity corrections $b(\alpha)$ and $f(\beta)$.

Fig.4.6 shows the mean energy-loss distribution in ADC units as a function of the velocity β obtained with 900,000 events preselected as helium nuclei. A fit is superimposed according to the parametrization:

$$BB(Z, \beta) = p_0 \frac{Z^2}{\beta^2} \left\{ \log \left[\frac{2m_e}{I_{Si}} \left(\frac{\beta}{1-\beta^2} \right) \right] - p_1 \beta^2 + \frac{p_2}{2} \right\} \tag{4.13}$$

where $Z = 2$ (helium charge) and $I_{Si} = 165\ eV$ (silicon excitation energy) are fixed, and $p_0 = 1.0$, $p_1 = -0.48$, and $p_2 = -31.11$ are the parameter determined by the fit that specifies $BB(Z, \beta)$. Assuming that saturation does not occur for helium energy losses, this behaviour is expected to correctly describe the real energy-loss dependence even for higher charges. Higher Z predictions, $BB(Z > 2, \beta)$, are shown in Fig.4.6 up to $Z = 8$ (Oxygen). The same BB functions are reported in Fig.4.7

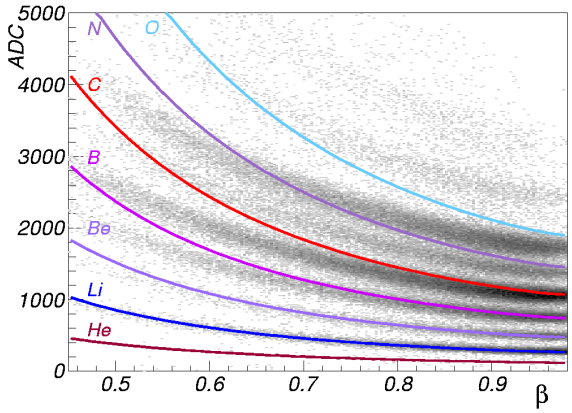

Figure 4.7: Beta functions up to Oxygen in comparisons with flight data.

in comparison with the cluster amplitude distributions observed from data: the average amplitudes $\langle |\cos\theta| \cdot g_\kappa \cdot \alpha \rangle$ are plotted versus the measured velocity. As an evidence of the inconsistency of Eq.4.10, it is clearly visible a significant discrepancy of the data points compared with the colored curves: data are systematically shifted toward lower cluster amplitude values. On the basis of this displacements, it is possible to determine the saturation curve $s(\alpha)$, provided that a guess on the particle charge is done. Though saturation does not depend on the particular charge Z that generated the signal, a sample with known Z and β is needed to perform a global parametrization for $s(\alpha)$. Since the goal of this task is to obtain a global trend, it is not necessary a high level of purity in the sample. Therefore, a coarse charge selection was done according to the graphical cuts illustrated in Fig.4.8[3]. The saturation function $s(\alpha)$ is described by the black curve in Fig.4.9: the mean cluster amplitude $\langle \alpha \rangle$ is plotted as a function of its *real* (predicted) energy-loss $BB(Z, \beta)$ for different ion species. The curve has been interpolated with a two-degree polynomial function. Once saturation is described by a know functional form $s(\alpha)$, it is possible to obtain an effective reproduction of the readout energy-loss for all the velocities: this is illustrated in Fig.4.10, where the energy-loss functions are shown before (solid) and

[3] Nevertheless, once the charge ID algorithm was accomplished, this task has been iterated using a more precise charge selection to refine $s(\alpha)$.

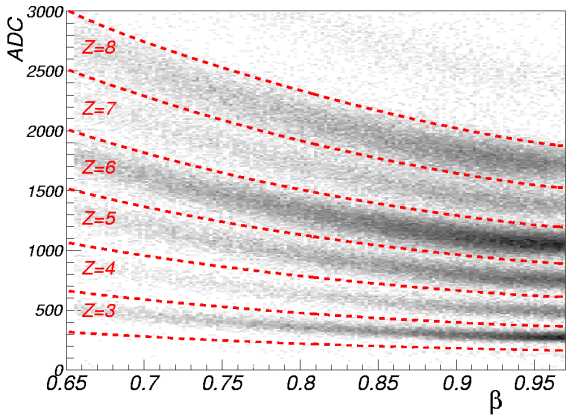

Figure 4.8: Coarse selection of the different nuclear species.

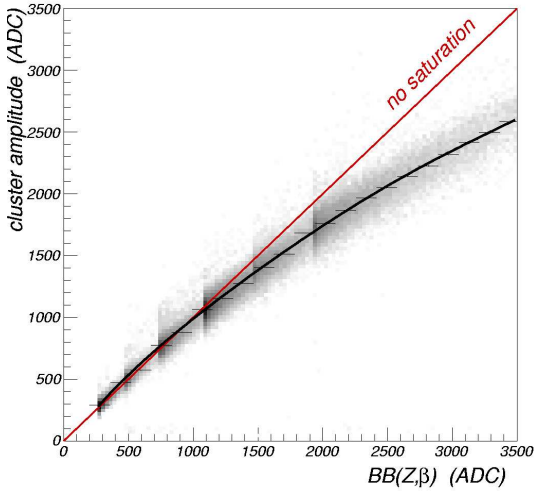

Figure 4.9: Saturation function determined by comparison of flight data with the predictions $BB(Z, \beta)$.

after (dashed lines) saturation $s(\alpha)$ is applied. Saturated BBs have functional form $BB(Z, \beta) \cdot s(BB(Z, \beta))$. Another possibility is to apply $b(\alpha) = s^{-1}(\alpha)$ directly to the data and to obtain an artificial de-saturation (or amplification) of the readout amplitudes. In the view of determining an effective cluster amplitude $A(\alpha, \beta, \theta, \kappa)$ to be described by a unique set of probability density functions $P^Z(A)$, the latter choice was adopted. Correcting data for saturation basically means to pull them up to the non-saturaction line (the identity function) as indicated in Fig.4.11. The result of this procedure is shown in Fig.4.12: after amplification $b(\alpha)$, the cluster

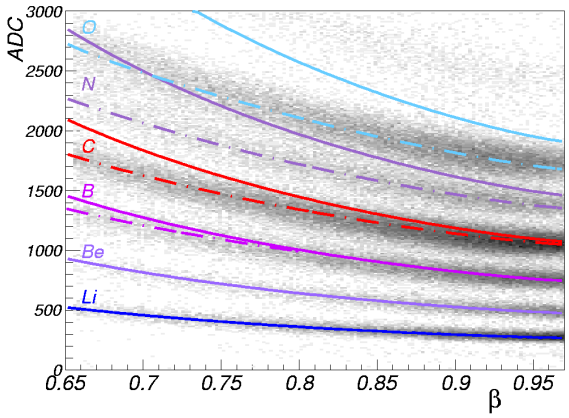

Figure 4.10: $BB(Z,\beta)$ functions for different nuclear families before (solid lines) and after correcting for saturation (dashed lines). These latter are calculated scaling $BB(Z,\beta)$ by $s(BB(Z,\beta))$.

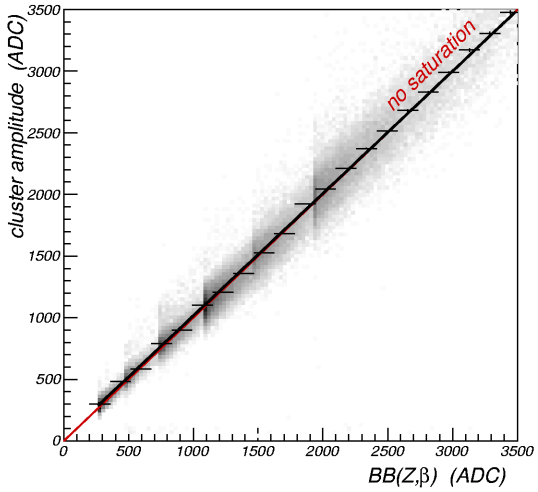

Figure 4.11: De-saturated data. This distribution is obtained after correcting for saturation.

amplitudes lie along the lines where they are expected, with good agreement up to $Z = 8$. It is interesting to note, however, that also few events with higher charges have been detected. From Fig.4.13, events corresponding to Neon ($Z = 10$), Magnesium ($Z = 12$) and Silicon ($Z = 14$) are clearly recognizable, as they are more populated than their odd-numbered neighbour Fluorine ($Z = 9$), Sodium ($Z = 11$) and Aluminium ($Z = 13$), due the odd-even effect in CR nuclear species abundances. Because of low statistics and a stronger saturation over $\sim 6,000$ ADC, these species are not well described with the model developed so far. These heavy nuclei are no

longer considered in this work.

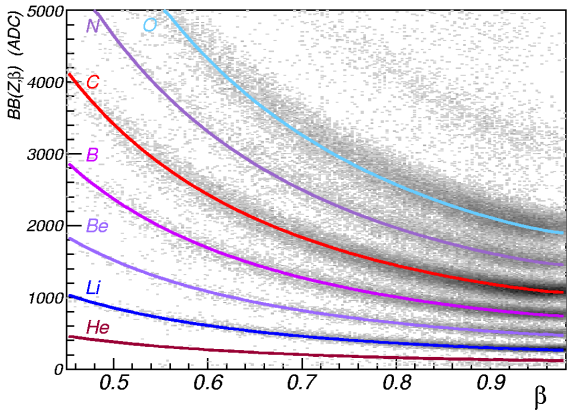

Figure 4.12: Beta functions up to Oxygen in comparisons with flight data after boosting.

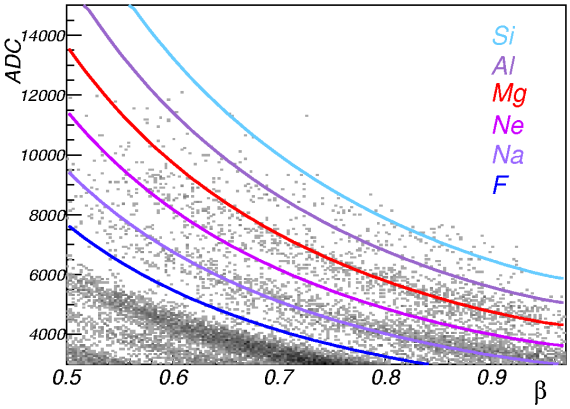

Figure 4.13: Beta functions for heavier nuclei (up to Silicon) in comparison with flight data after boosting.

The last step is determining the velocity correction. Indeed, the individual measurement after correcting for saturation is now given by the effective amplitude:

$$A(\alpha, \beta, \theta, \kappa) = |\cos\theta| \cdot g_\kappa \cdot \alpha \cdot b(\alpha) \cdot f(\beta) \tag{4.14}$$

where $b = s^{-1}(\alpha)$ and only $f(\beta)$ has to be determined. Since the β-dependence can be regarded now as a unique function $g(\beta)$ which does not depend on the charge, the following simplification can be done:

$$\langle b(\alpha) \cdot |\cos\theta| \cdot g_\kappa \cdot \alpha \rangle \propto BB(Z, \beta) = Z^2 g(\beta) \tag{4.15}$$

the correction for the velocity dependence turns out to be straightforward. After setting a reference value $\beta_0 \equiv 0.96$, $f(\beta)$ is defined as:

$$f(\beta) \equiv \frac{BB(Z, \beta = \beta_0)}{BB(Z, \beta)} = \frac{g(\beta = \beta_0)}{g(\beta)} \tag{4.16}$$

independently on the particle charge. After this last step the final amplitude

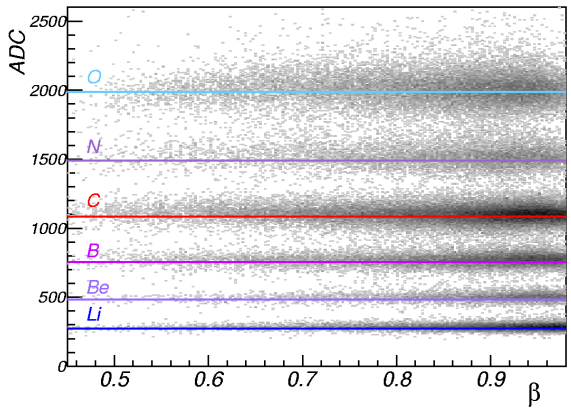

Figure 4.14: Flattened data after performing $f(\beta)$ correction for velocity dependence.

in completely specified. All the signals A are now referred to a common value β_0 (MIP level), and their distribution is completely independent from β. Results of this correction are shown in Fig.4.14. A review of the corrections performed so far is illustrated in Fig.4.15 where $\langle A \rangle$ is plotted as a function of β (left panels) and cumulatively (right panels). From top to bottom (a) raw amplitudes, (b) amplitudes after gain and inclinations corrections, (c) amplitudes after de-saturation and (d) flattened amplitudes after β corrections are shown. The special worth and utility of this multi-step procedure will appear more clear on the next section.

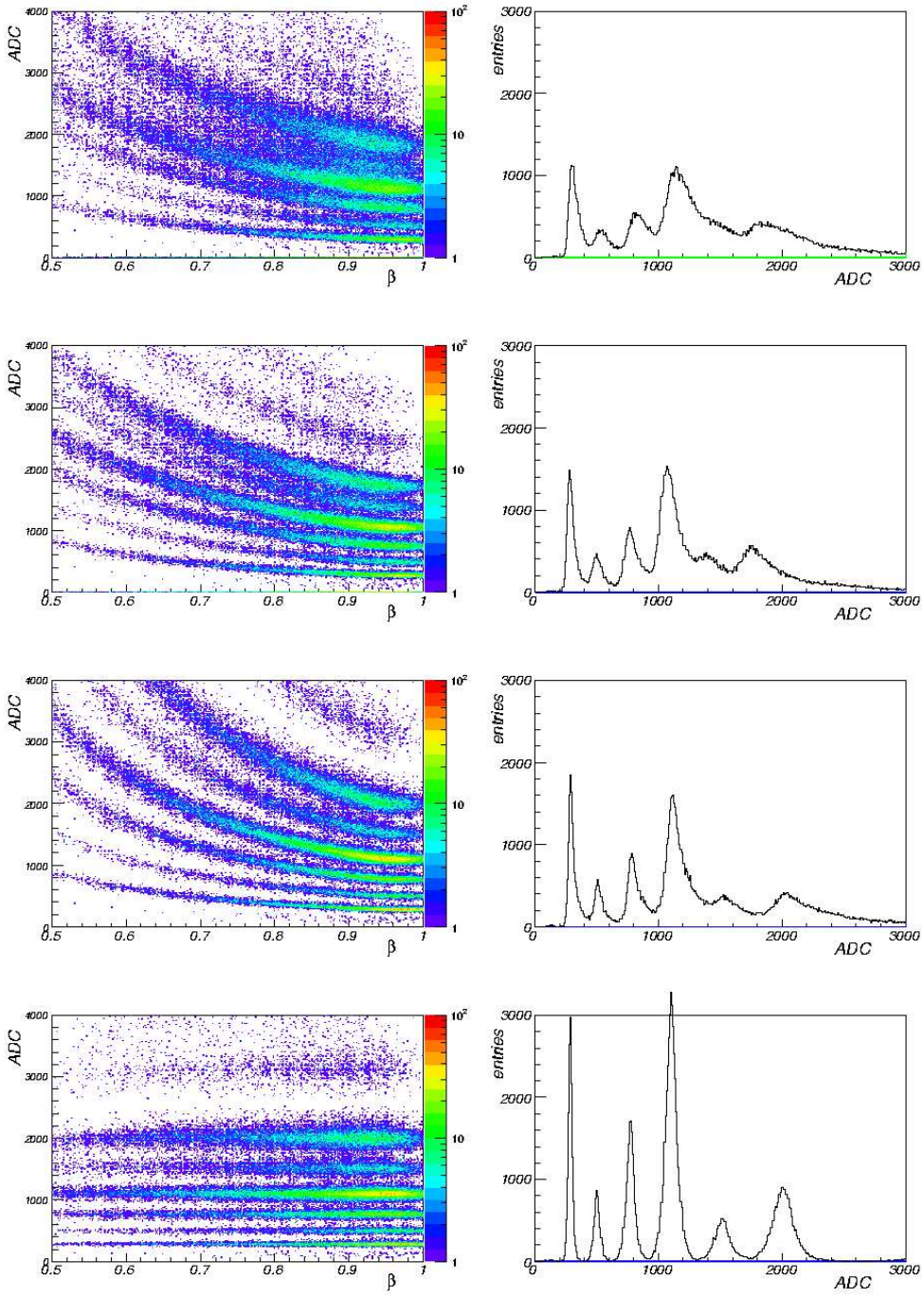

Figure 4.15: Review of the cluster amplitude corrections. The average amplitude $\langle A \rangle$ is plotted as a function of β (left panels) and cumulatively (right panels). From top to bottom: (a) raw amplitudes, (b) amplitudes after gain and inclinations corrections, (c) amplitudes after de-saturation and (d) flattened amplitudes after β corrections.

4.4 Determination of the PDFs

In the previous section, corrected cluster amplitudes have been determined. The energy-loss on the p-side is then described in terms of a unique parameter, i.e. the effective amplitude:

$$A \equiv A(\alpha, \beta, \theta, \kappa) \tag{4.17}$$

whose distribution $P^Z(A)$ is explicitly related to the charge of the particle. The variable $x \equiv \sqrt{A}$ will be adopted in the next stages.

This section is dedicated to the estimation of the probability, for a given Z, to be associated to the measured energy deposit x. A set of probability density functions (PDF) corresponding to different charges has been constructed from a clean sample of data with known charge. A combined likelihood function with the up to six track-clusters has then been used to provide the best estimation of the nuclear charge, needed to measure the composition the cosmic radiation.

The general parametrization usually adopted to describe energy-loss measurements E_{dep} is the gaussian-convoluted Landau function:

$$f(E_{dep}) = N \int_{-E_{dep}}^{E_{dep}} L(\mu, \nu, \epsilon) G_{\mu,\sigma}(E_{dep}) d\mu \tag{4.18}$$

being $G_{\mu,\sigma}(E)$ and $L(\mu, \nu, \epsilon)$ the Gaussian and Landau functions. However, due to large energy depositions released by $Z > 2$ ions in the silicon, it was found that the bulk of the charge distribution is quite symmetric and the corresponding x parameter is well described by a simple gaussian function:

$$G^Z = G^Z_{\mu_Z,\sigma_Z}(x) = N e^{\left(\frac{x-\mu_Z}{\sigma_Z}\right)^2} \tag{4.19}$$

Pure samples of different ions have been selected to determine the gaussian parameters μ_Z (mean energy-loss or maximum probability value) and σ_Z (standard deviation) that better describe the distributions. The charge selection method is illustrated in the scheme of Fig.4.16. For each layer under study, samples with well defined charges have been selected by means of the signal observed in the neighbour layers: in both of them, energy depositions x falling around each charge peak and belonging to specified ranges were required. This selection produces a low efficiency but high purity sample[4] per layer to characterize the detector charge response. Nonetheless, the largest difference in the amplitude distribution from ladder to ladder is reduced to a gain correction (already performed).

[4] Intra-charge contamination is smaller than 0.1%, as verified *a posteriori*

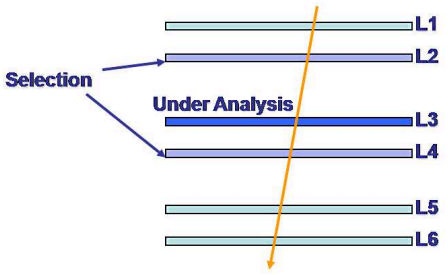

Layer under analysis	Layers used in selection
L1	L2 & L3
L2	L1 & L3
L3	L2 & L4
L4	L3 & L5
L5	L4 & L6
L6	L5 & L6

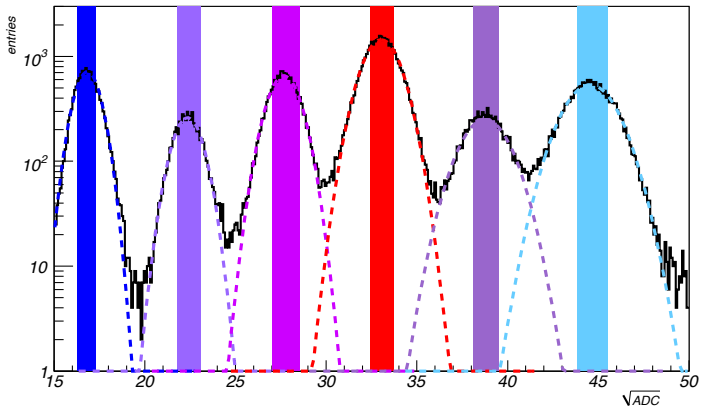

Figure 4.16: Charge selection. For each layer L under study, layers L+1 and L-1 were used to select a pure Z-sample by means of the six vertical bands around the charge peaks. To give an idea of the sample purity, gaussian functions as derived from Fig.4.17 are superimposed.

Hence, a common parametrization has been used to describe and fit the cluster amplitude distributions on all the ladders. Indeed, for a given Z, the μ_Z and σ_Z parameters of the gaussian distributions do not significantly differ from layer to layer[5].

[5]Not even from ladder to ladder; nevertheless, residual differences on the μ parameter have been used to refine the gain correction factor, e.g. defining it as $g_k^Z = \mu_k^Z / \mu_{k_R}^Z$.

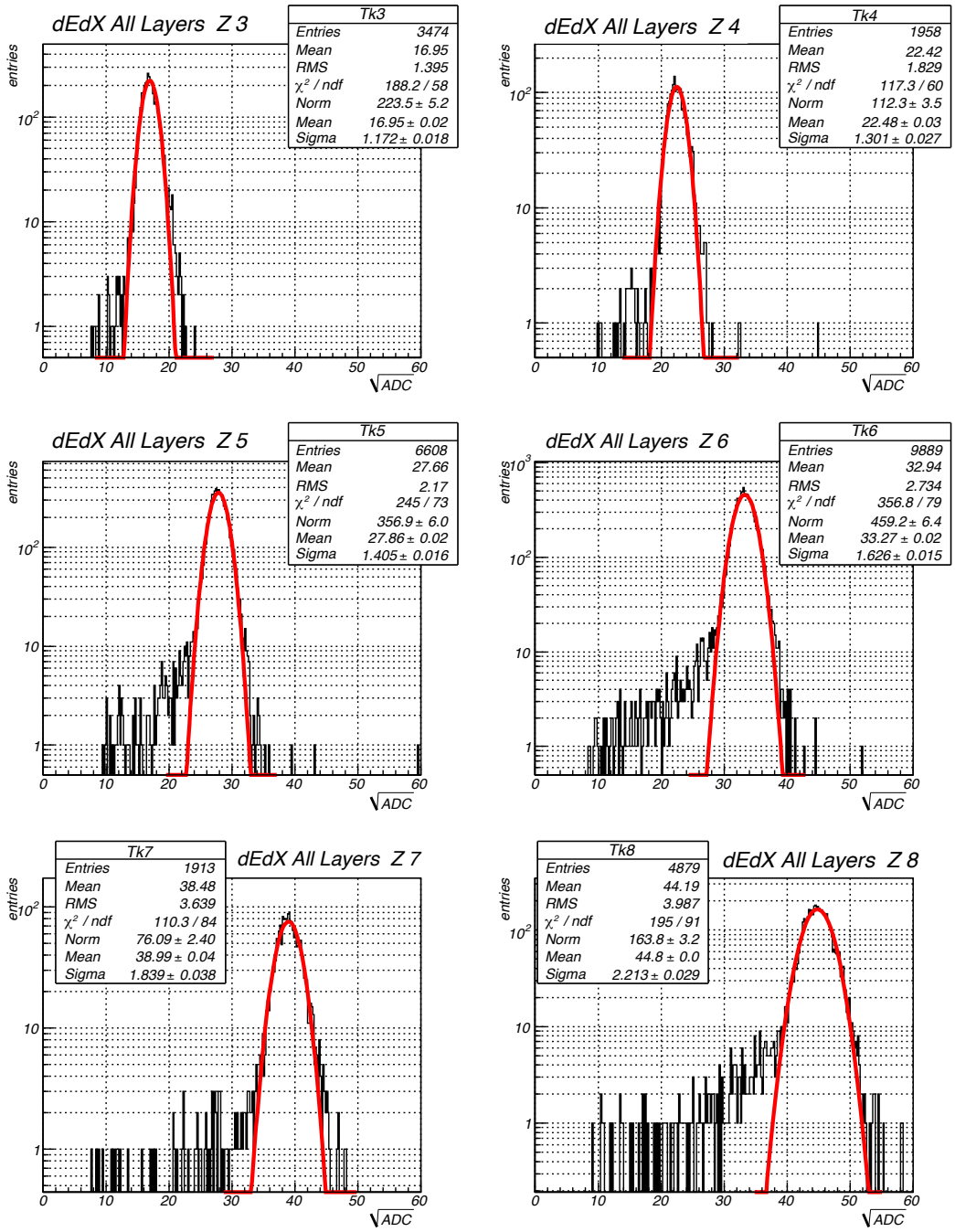

Figure 4.17: Square root of the corrected amplitude distributions for $Z = 3$ (top left) to $Z \div 8$ (bottom right). Gaussian fits are superimposed. A summary is presented in Tab.4.1.

Results of the fits are shown in Fig.4.17; all the single-layer information have been merged together to produce a unique set of cumulative histograms that depend only

on the charge. Gaussian fits have been performed each nuclear species. The non-gaussian tails on the left side of each peak are discussed on the next section; their influence on the fit results is insignificant. Fit results are summarized in Tab.4.1.

Ion	Z	μ	σ
Not Li	< 3	9.40	1.43
Li	3	16.95	1.17
Be	4	22.48	1.30
B	5	27.86	1.40
C	6	33.27	1.63
N	7	38.99	1.84
O	8	44.80	2.21
Not O	> 8	55.83	3.62

Table 4.1: Results from gaussian fits to the corrected amplitude distributions for $Z = 3 \div 8$.

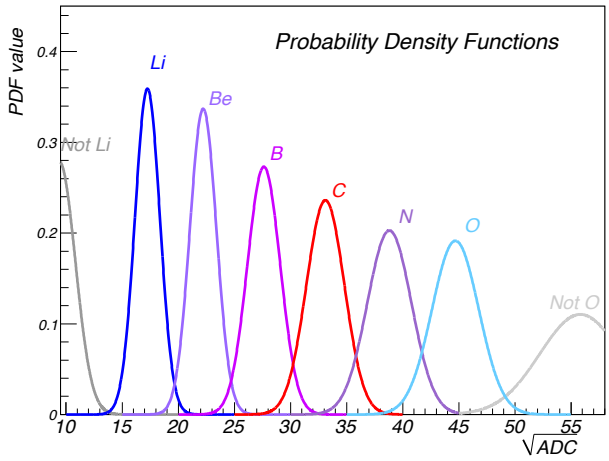

Figure 4.18: Probability density functions $P^Z(x)$ for $Z = 3 \div 8$. Parametrization of background to $Z = 3$ and $Z = 8$ is also considered.

The last step is the normalization of the fitted distribution:

$$P^Z(x) = \frac{G^Z_{\mu,\sigma}(x)}{\int_{-\infty}^{\infty} G^Z_{\mu,\sigma}(x)dx} \tag{4.20}$$

These normalized $P^Z(x)$ functions have to be viewed as PDFs: a charged Z particle has a probability value $P^Z_k(x)$ to generate a cluster with effective amplitude x.

$$P^Z(x) = P(x|Z) \tag{4.21}$$

The shapes of the resulting PDFs is shown in Fig.4.18 for all the species considered. Parametrization of $Z < 3$ and $Z > 8$ tails has also been performed. Even though these residual contaminations are found to be negligible in both sides, the determination of He and F tails is needed to avoid boundary effects in the charge identification algorithm that will be exposed in the next section.

4.5 The Charge ID Algorithm

The charge identification algorithm presented here is based on the *Maximum Likelihood* method (ML), a widely diffused statistical procedure used to fit a theoretical model to data. The general aim of this method is to estimate the parameter by finding the value which maximizes the probability that a given set of measurements is observed.

The general procedure consists in considering a family of probability distributions parametrized by an unknown parameter Z (the particle charge), associated with a known probability density function denoted as $P^Z(x)$. After drawing a sample $\{x_1, x_2, \ldots, x_n\}$ of n values from this distribution, using $P^Z(x)$, the algorithm consists in computing the multivariate probability density associated with the observed data $P(x_1 \ldots x_n|Z)$. As a function of Z with $(x_1, ..., x_n)$ fixed by the observation, the *likelihood function* is defined as:

$$\mathcal{L}(Z) = P^Z(x_1, \ldots, x_n|Z) \tag{4.22}$$

The method of maximum likelihood estimates Z by finding the value $\hat{Z}$ that maximizes $\mathcal{L}(Z)$:

$$\left.\frac{\partial \mathcal{L}(Z)}{\partial Z}\right|_{Z=\hat{Z}} = 0 \tag{4.23}$$

The outcome $\hat{Z}$ is the ML estimator of Z. Since in this case Z is a discrete parameter, the maximization of $\mathcal{L}$ involves a scan over the Z domain. After equalization, the data drawn from different energy deposits along the particle track are independent and identically distributed. This considerably simplifies the problem because the likelihood can be written as a product of n univariate probability densities, and since maxima are unaffected by monotone transformations, it is more comfortable to define $\mathcal{L}$ as the logarithm of the previous expression to turn it into a linear sum:

$$\mathcal{L}(Z) = \log_{10}\left[\prod_{j=1}^{j=n} P^Z(x_j)\right] = \sum_{j=1}^{j=n} \log_{10}\left[P^Z(x_j)\right] \tag{4.24}$$

In this particular study, n is the number of p-side clusters available for the test (for each event it varies from 3 to 6), $\{x_j\}$ is the set of cluster amplitudes after corrections, and the j-index runs over the six layers. $P^Z(x)$ are the probability density

functions $P(x|Z)$ estimated as explained in the previous sections.

From the fits in Fig.4.17, it is noticeable that not all the cluster amplitudes x are distributed according to a gaussian behaviour. Distributions exhibit asymmetric low-energy tails that originates from unavoidable inefficiencies in the charge collection. This residual population of *bad clusters* is quantified as a small fraction which survives after cuts and does not carry reliable information on the particle charge. As a consequence, the probability from Eq.4.24 may be heavily suppressed and then affected by a single wrong charge response which enters in the product[6]. Despite the overall fraction of bad clusters is quite small (from $\sim 1.4\%$ for Lithium up to $\sim 3.5\%$ for Oxygen), the probability to have at least one bad cluster out of six independent readouts (six layers) ranges from $\sim 9\%$ for Lithium to $\sim 18\%$ for Oxygen: a significant fraction of events may be involved. For this reason, a modified version of the ML method was used. The actual log-likelihood function used in the test is:

$$\mathcal{L}(Z,\Omega) = \log_{10}\left[P^Z_{l_1} \cdot P^Z_{l_2} \cdot P^Z_{l_3}\right] \tag{4.25}$$

where Z ranges from 2 to 9 and Ω runs over all the $\{l_1, l_2, l_3\}$ 3-fold combinations of the tracker signals. Ω is the best set of three clusters recognized by the ML test as well as Z. Two important features on this method are worthy of being noticed:

1. In events with more than 3 clusters, bad clusters are ruled out by the ML method itself.

2. Although the final estimation is given by a set of three best tracker clusters, all the selected cluster are processed in Eq.4.25: Z and Ω have both to be viewed as parameters to be maximized using all the available information.

As a test to provide the basic understanding of the algorithm characteristics and operation, in Fig.4.19, it is shown the average cluster amplitude distribution divided into four different β intervals. The average has been performed on the $\{x_{l_1}, x_{l_2}, x_{l_3}\}$ best cluster set recognized by the ML. Different colors are referred to different charge $\hat{Z}$ as identified by the algorithm. Ion peaks are well distinguished for all the nuclear species considered, from $\hat{Z} = 3$ (dark blue) to $\hat{Z} = 8$ (cyan). A smaller Neon peak (Z=10) is also recognizable around $55\sqrt{ADC}$. Finally, the linearity of the signals after corrections is pointed out in Fig.4.20; this feature allows to convert the amplitude distributions from $\sqrt{ADC}$ into charge unit (upper plot) and provide an estimation of the resulting discrimination power in terms of charge resolution. These results are summarized in Tab.4.2

[6]Note, however, that the presence of one bad cluster in the event does not always imply a systematic wrong outcome from the ML test.

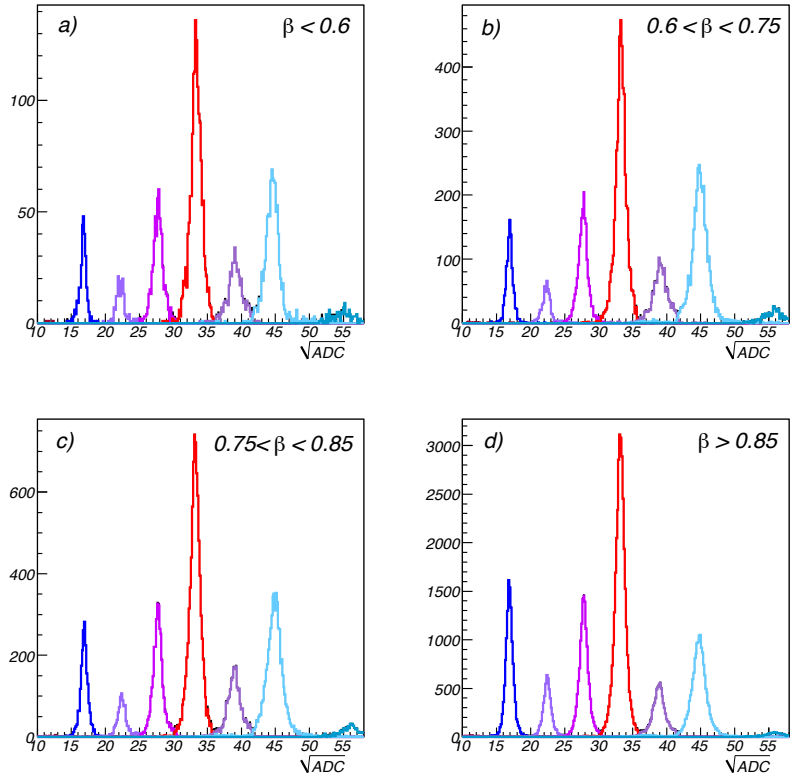

Figure 4.19: Square root of the average energy loss computed with the p-side of the silicon tracker, divided in four different increasing β intervals (top left to bottom right). Different colors are referred to different charge $\hat{Z}$ identified by the algorithm. Ion peaks are well distinguishable from $Z = 3$ (dark blue) to $Z = 8$ (cyan). Neon peak (Z=10) is also recognizable at around $\sim 55\sqrt{ADC}$.

Ion	Z	resolution
Li	3	0.09 c.u.
Be	4	0.10 c.u.
B	5	0.12 c.u.
C	6	0.14 c.u.
N	7	0.18 c.u.
O	8	0.19 c.u.

Table 4.2: Charge resolutions obtained by the width of the charge spectrum. Charge histogram was converted from $\sqrt{ADC}$ into charge unit as illustrated in Fig.4.20.

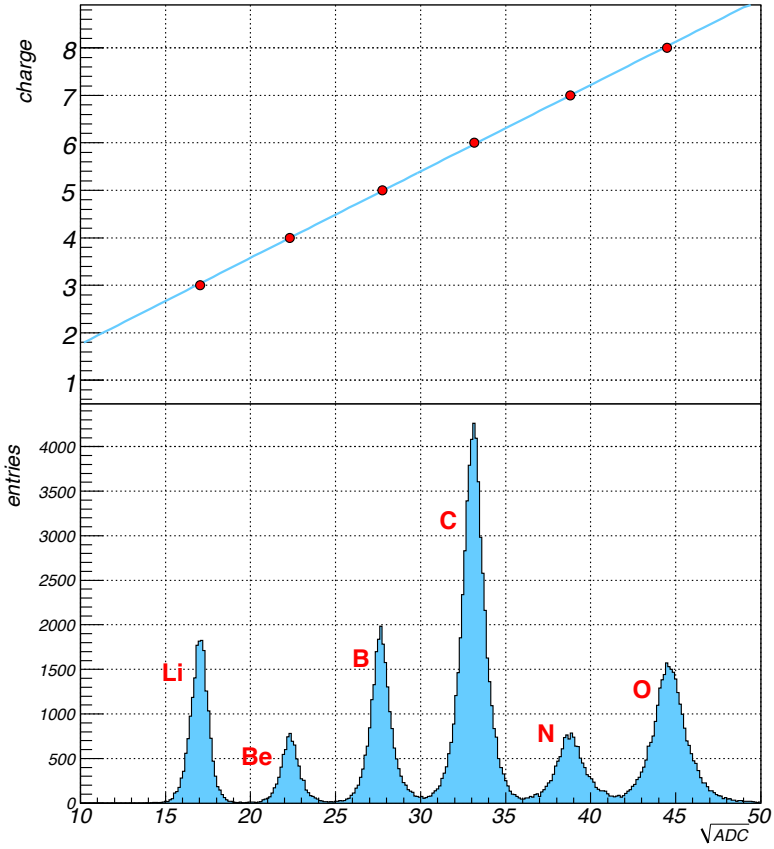

Figure 4.20: Final charge spectrum in $\sqrt{ADC}$ units. A noticeable linearity in the charge response is evident by the comparison with charge unit scale.

4.6 Algorithm Performances

The charge identification algorithm has been successfully applied to the flight data sample. Qualitatively, its capabilities are clearly visible from Fig.4.19, where a good discrimination has been observed in all the considered β intervals. In addition, according to Tab.4.2, the desired charge resolutions have been achieved .

The algorithm performances in terms of efficiency and contamination are now discussed. Since the particle reconstruction is based on the Maximum Likelihood method, it has the advantage of being an unbiased and efficient charge estimation for a large number of events. The method is 100% efficient (i.e. a charge estimation $\hat{Z}$ is always given) provided that at least three good clusters are usable (the minimal condition for applying Eq.4.25). Though the reconstruction software requires at least four p-side clusters to build a track, the mentioned selection on the

tracker clusters (strip occupancy mask and single-strip cluster rejection) produces a fraction of $\sim 2.5\%$ of events with $N_{cls} < 3$. This inefficiency is significantly charge-independent, as the charge distribution of these *missed* events[7] is comparable with those charges observed and determined with the algorithm; the final flux ratios (e.g. B/C ratio) have been estimated to be affected by a factor smaller than 0.5%.

In order to quantify the discrimination power in the charge recognition, a global test has been carried out. Due to energy-loss fluctuation and broadening of the charge response, an unavoidable overlapping of the measured dE/dx distributions produces a non-zero $Z \to Z'$ migration probability.
The overlappings of the PDFs are clearly visible in Fig.4.18: the underlying area between two contiguous charge curves gives an approximate idea of the single-cluster charge confusion probability ($\sim 2\%$ for Lithium to $\sim 10\%$ for Oxygen). The overall effect, after the algorithm was applied to the data, is not trivial to estimate with qualitative arguments. A dedicated Monte Carlo simulation has then been therefore performed.

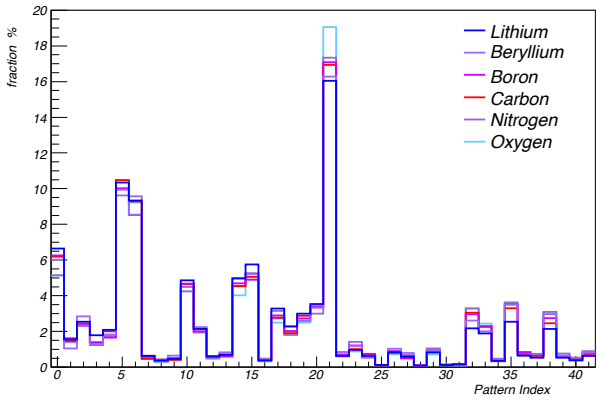

Figure 4.21: Distribution of the track patterns along the six layers observed with the data for $Z = 3 \div 8$. Each index is associated to a given combination of clusters arrangement along the six layer, as explained in Tab.4.3.

For each event, a set of n signals has been generated according to the cluster distributions along the six tracker layers observed from the data (Fig.4.17). For this purpose, the tracks are classified and a pattern index is assigned based on the combination of layers which hosts a good cluster. The meaning of the pattern index is explained in Tab.4.3. Distribution of the number of clusters after selection and the pattern distribution are shown in Fig.4.21 (its resulting layer occupancy is

[7] For their Z estimation, being ML not applicable, a less sophisticated charge ID method was used.

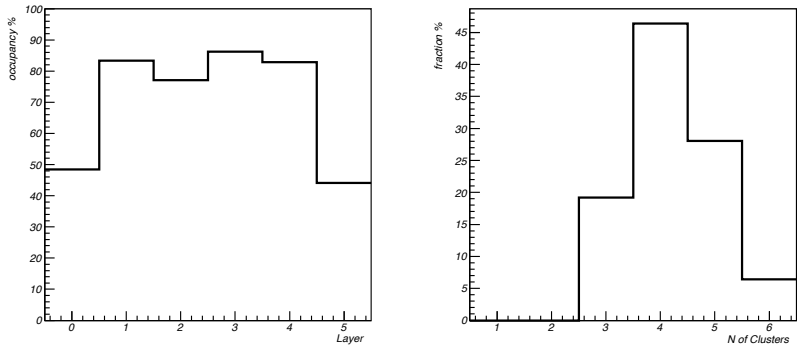

Figure 4.22: Distribution of layer occupancy fraction (left) and number of clusters used to determine the charge.

Pattern	L1	L2	L3	L4	L5	L6	Ncl		Pattern	L1	L2	L3	L4	L5	L6	Ncl
0	x	x	x	x	x	x	6		21		x	x	x	x		3
1	x	x	x	x	x		5		22	x	x	x				3
2	x	x		x	x	x	5		23	x	x		x			3
3	x	x	x		x	x	5		24	x	x			x		3
4	x		x	x	x	x	5		25	x	x				x	3
5	x	x	x	x	x		5		26	x		x	x			3
6		x	x	x	x	x	5		27	x		x		x		3
7	x	x		x		x	4		28	x		x			x	3
8	x	x	x			x	4		29	x			x	x		3
9	x		x	x		x	4		30	x			x		x	3
10	x	x	x	x			4		31	x				x	x	3
11		x	x	x		x	4		32		x	x	x			3
12	x	x			x	x	4		33		x	x		x		3
13	x			x	x	x	4		34		x	x			x	3
14	x	x		x	x		4		35		x		x	x		3
15		x		x	x	x	4		36		x		x		x	3
14	x		x		x	x	4		37		x			x	x	3
17	x	x	x		x		4		38			x	x	x		3
18		x	x		x	x	4		39			x	x		x	3
19	x		x	x	x	x	4		40			x		x	x	3
20			x	x	x	x	4		41				x	x	x	3

Table 4.3: Tracker patterns. For each pattern index, layers that contains a good cluster are marked with x. The resulting number of clusters is indicated in the N_{cl} column.

reported in Fig.4.22). Except for Oxygen, where a small excess of Pattern 21 tracks is observed, the pattern distribution is considerably charge independent. Fig.4.22 shows the layer occupancy distribution (i.e. the probability of a layer to have good cluster) and the number of clusters distribution. Inefficiencies on 1^{st} and 6^{th} layer are mainly due to their reduced active area and features of the track recognition algorithm.

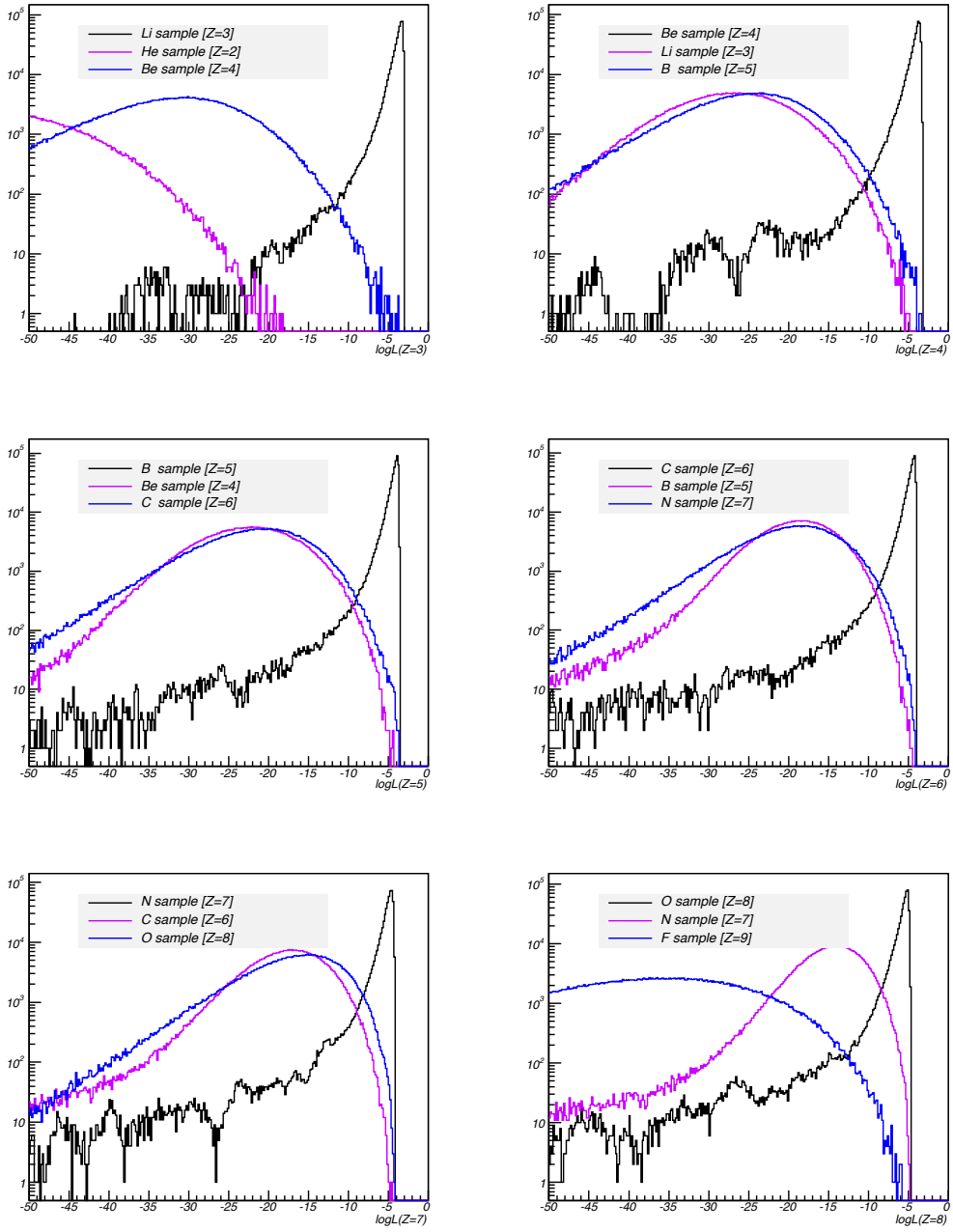

Figure 4.23: Distribution of the log-likelihood function $\mathcal{L}(Z)$ (Z fixed) for pure Z (black), $Z+1$ (blue) and $Z-1$ (purple) MC samples. For each injected species, Z is kept fixed in the $\mathcal{L}(Z)$ calculation. Mis-identification occurs when the colored lines dominate over the black one.

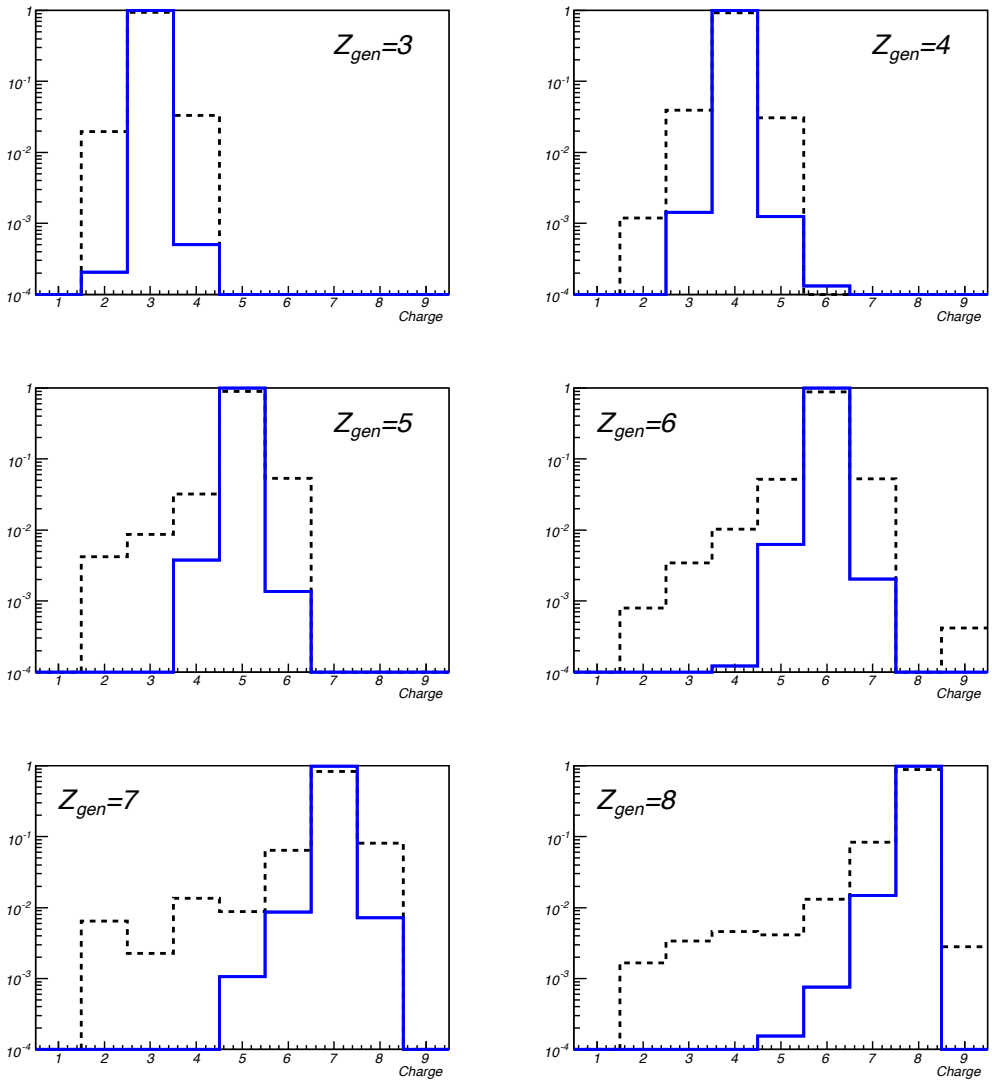

Figure 4.24: Charge identification algorithm capabilities. For each charge Z_{gen}, generated by the simulation, it is reported the charge response $\hat{Z}$ from the algorithm applied to the whole tracker (solid blue histograms). For the sake of comparisons, single layer performances (ML response from Layer 3) are also reported (dashed lines).

The influence of charge mis-identification on the differential fluxes impinging the detector is described by the following relation:

$$Y_{\hat{Z}}(E_{kn}) = \sum_{Z=3}^{8} C_{\hat{Z}}^{Z} Y_Z(E_{kn}) \tag{4.26}$$

where Y_Z is the CR abundance of the charge Z ion as a function of kinetic energy

per nucleon. Each nucleous with charge $3 \leq Z \leq 8$ produces a charge estimation $\hat{Z}$ which is related to its *true* charge Z by the coefficients $C^Z_{\hat{Z}}$. The C-matrix elements have then to be interpreted as the probabilities $P(\hat{Z}|Z)$ of a given charge Z to be (mis)identified as $\hat{Z}$. In this work the matrix $||C||$ is assumed to be energy independent and $Z < 3$ or $Z > 8$ species are not considered. As a matter of fact, contaminations $He \rightarrow \hat{Li}$ and $F \rightarrow \hat{O}$ are negligible, whereas $Li \rightarrow \hat{He}$ and $O \rightarrow \hat{F}$ are not matter of interest in this particular study[8].

Fig.4.23 shows the distribution of the log-likelihood function and gives an idea of the mis-identification: log-likelihood $\mathcal{L}(Z)$ distributions for assigned charge samples generated as Z, $Z+1$ and $Z-1$ are shown. Mis-identification occurs whenever $\mathcal{L}(Z)|_{Z_{gen}=Z\pm1} > \mathcal{L}(Z)|_{Z_{gen}=Z}$. More clear and understandable is Fig.4.24: the charge responses $\hat{Z}$ from the algorithm (blue lines) are shown for each Z_{gen} injected with the simulation. Performances are compared with the single layer identification capabilities (dashed lines), where the ML algorithm is applied using information from Layer 3 only (i.e. a single-layer $P^Z(x)$ has been maximized).

A summary of the contamination coefficients is reported on Tab.4.4. The 6×6 matrix $||C||$ is symmetric and diagonally-dominated; the off-diagonal elements are relevant only for $\hat{Z} = Z \pm 1$, i.e. contamination arising from neighbour charge peaks. An additional characterization of the charge discrimination power was also done with

%	Li	Be	B	C	N	O
$\hat{Li}$	**99.93**	0.14				
$\hat{Be}$	0.06	**99.73**	0.36	0.02		
$\hat{B}$		0.012	**99.51**	0.61	0.01	
$\hat{C}$			0.13	**99.20**	0.93	0.06
$\hat{N}$				0.16	**98.30**	1.51
$\hat{O}$					0.74	**98.40**

Table 4.4: Contamination matrix. Charge selection results from the algorithm (rows) are compared with the true charges (columns). Each column corresponds to the sample of given ion species (Z) generated with the simulation. For a given column, each cell reports the fraction of events identified by the algorithm as $\hat{Z}$ specified in the row. The values on the matrix diagonal correspond to the probabilities $P(\hat{Z} = Z|Z)$ of correct charge identification, whereas the off-diagonal elements describe the probability of mis-measurement $P(\hat{Z} \neq Z|Z)$.

the help of measured data. Whereas the MC simulation permits a thorough study

[8]Since we are not interested in Helium and Fluorine measurements, charge migrations $Li \rightarrow \hat{He}$ and $O \rightarrow \hat{F}$ are just considered as source of inefficiencies for Lithium and Oxygen abundances.

of the charge reconstruction applied to the whole tracker, this is unfortunately not the case for flight data, where the information on the *true* charge Z is obviously missing. Hence this study was done with a sub-sample of events containing six good

STS - 91	Li	Be	B	C	N	O
$\hat{Li}$	**99.99**	0.01				
$\hat{Be}$	0.01	**99.99**	0.1			
$\hat{B}$			**99.40**	0.88		
$\hat{C}$			0.5	**99.12**	1.64	
$\hat{N}$					**95.08**	1.84
$\hat{O}$					1.74	**98.16**

MC-SIM	Li	Be	B	C	N	O
$\hat{Li}$	**99.84**	0.14				
$\hat{Be}$	0.16	**99.78**	0.16			
$\hat{B}$		0.08	**99.45**	0.69		
$\hat{C}$			0.32	**99.14**	2.07	
$\hat{N}$				0.17	**97.38**	2.28
$\hat{O}$					0.55	**97.72**

Table 4.5: Contamination matrices: DATA-MC comparison for contamination probabilities estimated with four layers. In each table, charge selection results from the algorithm (rows) are compared with the true charges (columns). The values of each the matrix elements corresponds to the probability $P(\hat{Z} = Z|Z)$ that a Z-charged nucleus is reconstructed as $\hat{Z}$. For both the data sample (flight data on the top table, MC on the bottom), true charge was estimated with the two outer layers and the algorithm was applied to the four inner layers. Only six-clusters events were considered.

clusters: two of them have been used to select the true charge (selection is analog to Fig.4.16, using Layer 1 and Layer 6) and the algorithm has been applied to the four inner-layer clusters. Since the average number of good cluster is ~ 4.5 (see Fig.4.22) this conservative approach is not really far from the real case; the only weak spot is the lack of considerable statistics from flight data to have a reasonably pure sample: only some hundred $\div$ thousand events per charge were selected. Results are summarized on Tab.4.5 in terms of C-matrix elements, and a comparison with the Monte Carlo (under the same conditions) is also reported.

4.7 The Role of Inelastic Collisions

It is now considered an additional source of contamination which has nothing to do with the algorithm performance. After interacting in TOF material, an incoming Z-charged nucleus may fragment and physically turn into another species Z'. The

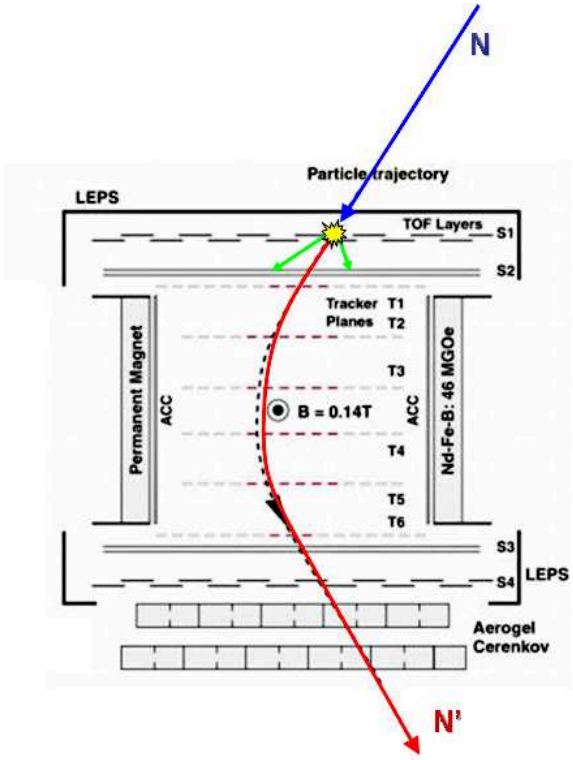

Figure 4.25: Scheme of a typical fragmentation event that produces contamination in the charge measurements. A nucleus N (eg. Oxygen) after interacting in TOF material, tuns its identity into N' (eg. Carbon). If the event is not discarded by trigger and selection, a correct charge estimation provides a wrong determination of the incoming particle species.

situation is illustrated in Fig.4.25. Since inelastic collisions are typically accompanied by a hadronic cascade of secondary particles, these multi-particle events are likely to be removed by the trigger system (*veto* on anti-coincidences and *one and only one hit* condition on each TOF plane). However, a fraction of them produces a clean track in the silicon tracker, passing trigger and selection. These effects have been studied with the Monte Carlo simulation `AMS-GBATCH` software, where detector response is fully reproduced and nuclear interaction are described under the `GEANT 3.21` interfaced `RQMD` hadronic package (§2.4.2 and §2.4.3). Unlike charge confusion arising from overlapping on the charge responses, inelastic collisions produce a systematic migration $Z \rightarrow Z'$ with $Z' < Z$, i.e. the corresponding *fragmentation*

%	Li	Be	B	C	N	O
Li'	**99.99**	0.12	0.06	0.02	0.01	0.01
Be'	0.01	**99.88**	0.36	0.20	0.08	0.07
B'			**99.58**	0.53	0.15	0.08
C'				**99.24**	5.31	4.07
N'					**94.44**	
O'						**95.77**

Table 4.6: Fragmentation matrix. Each column corresponds to the sample of given ion species Z generated with the simulation and injected in the detector. For a given column, each cell reports the fraction of charged Z' events observed in the tracker, i.e. after passing two upper TOF layers. The values on the matrix diagonal correspond to the probability $P(Z' = Z|Z)$ that the charge identity is conserved after traversing the TOF, whereas the off-diagonal elements are describes the probability $P(Z \neq Z'|Z)$ for that a process like $Z + TOF \rightarrow Z' + secondaries$ occurs and is detected. These probabilities are net of trigger and selection.

matrix $||F||$ is triangular. The coefficients $F^Z_{Z'}$ are reported on Tab.4.6 in percent units.

4.8 Test Beam Data

A comparison with data collected during the ion beam test is now presented. Test was performed at GSI facility, Darmstad, in September 1998. The detector was calibrated with helium and carbon beams.

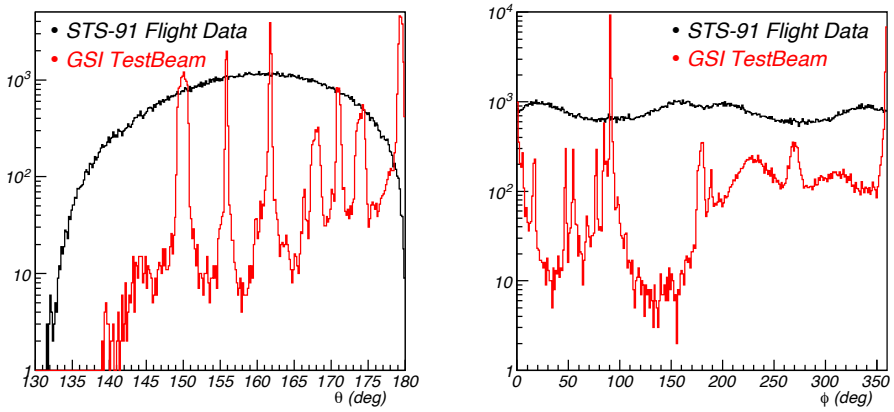

Figure 4.26: Distributions of θ_{AMS} and ϕ_{AMS} from carbon beam test data. Whereas flight data histograms reflect an almost isotropic distribution, GSI data are mainly beamed and more vertical on average, though a large set of incoming direction was probed.

About 30,000 events were detected and selected from the beam test made with pure ^{12}C ion beam. Kinetic energy of the carbon beam was fixed at 2.0 GeV/n. Beam spot on target had a Gaussian shape with characteristic width of 5 mm. A large area was scanned by the beam, as the detector was allowed to rotate into all the spatial and angular degrees of freedom. The distributions of the beam particles directions in the AMS-01 reference frame are shown in Fig.4.26 and compared with those recorded in the flight.
Fig.4.27 shows the mean cluster amplitude distribution obtained from these data together with the data from the flight. The same equalization above described is applied to the testbeam signals. The distribution is normalized in order to match the flight data histogram. It should be noted that in beam data the energy is fixed, i.e. corrections for the velocity dependence has not effect on the cluster signals. As expected, the charge responses of detector and algorithm are found to be identical for the two datasets.

Assuming a 100% purity in the carbon beam, an estimation of the charge determination capabilities can be obtained from the GSI data, As indicated in Fig.4.28, out of the 30,000 detected particles, 98.75% of then where identified as Carbon. 1%

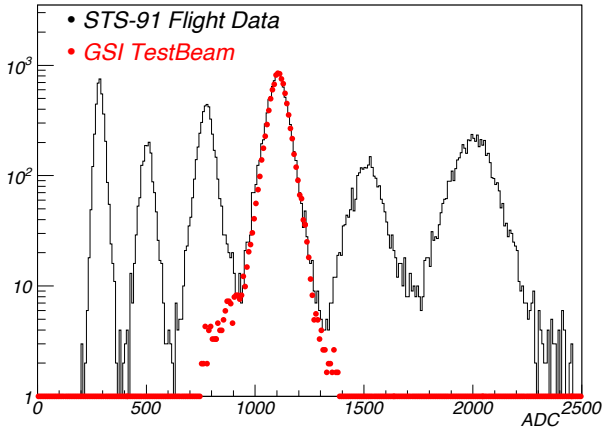

Figure 4.27: Beam test measurement for a carbon beam with kinetic energy $E_{kn} = 2$ GeV per nucleon. The mean cluster amplitude from testbeam data (red dots) is reported as well as for data measured from the flight (black line).

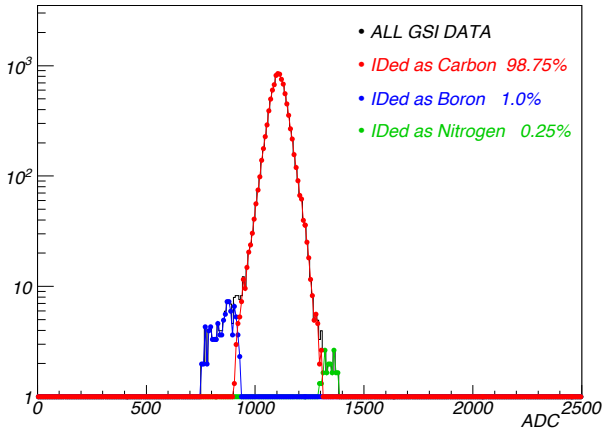

Figure 4.28: Charge identification results for a pure carbon beam with $E_{kn} = 2$ GeV/n. A small admixture of Boron (blue) and Nitrogen (green) nuclei has been detected.

Boron and 0.25% Nitrogen have been found. Whereas the few $\hat{Z} = 7$ data (green) can certainly be interpreted as a wrong charge assignment, it is reasonable that a certain fraction of the $\hat{Z} = 5$ population (blue) is composed of true Boron nuclei, i.e. produced after fragmentation before the tracker. However, it is difficult to separate the two contributions (fragmentation and mis-identification) that produced a $\hat{Z} = 5$ measurement, but the overall effect is measurable and it turned out to be in good agreement with the estimations made in the previous sections §4.6 and §4.7. Un-

fortunately, no beam tests have been performed for other ion species. Nonetheless, the various arguments exposed in this chapter proved that it is possible to build up a suitable charge determination study based on flight data only.

4.9 Discussion

A powerful algorithm has been presented for the charge determination of nuclei detected by AMS-01. It is also clear that, with the silicon tracker, noticeable charge separation capabilities have been achieved, allowing to draw a charge spectrum of the energy losses with the different nuclear families well distinguishable and separated. The discrimination power provides a final charge resolution of $0.09 \div 0.19$ charge units from Li to O.

The effects of inelastic collisions and charge contamination on the CR flux measurements are now discussed. It should be noted that $F^{Z}_{Z'}$ probabilities are assumed to be energy independent as well as the C-matrix coefficients. Common parametrizations of fragmentation cross sections above hundreds MeV/n are usually energy independent [23, 121]. The net effect of fragmentation in the CR flux measurements is expected to be mostly determined by their relative composition rather than any possible energy dependence on the F-coefficients. Indeed the relation between the external CR flux composition and the measurement is given by the relation:

$$Y_Z(E_{kn}) = \sum_{Z'=3}^{8} P(Z|Z')Y_{Z'}(E_{kn}) \tag{4.27}$$

where $P(Z|Z')$ is the probability of a given charge Z' to be identified as Z[9]. Fragmentation and mis-identification are both included in P:

$$P(Z|Z') = \sum_{Z''}^{8} C^{Z''}_{Z} \cdot F^{Z'}_{Z''} \tag{4.28}$$

In principle, by the exact knowledge of $C^{Z''}_{Z}$ and $F^{Z'}_{Z''}$ coefficients, it would be possible to correct the measured abundances Y_Z to get those corrected (eg. inverting the $||P||$ matrix). In practice some problems arise. Firstly the estimation of the coefficients are affected by uncertainties which do not trivially propagate on the deconvolution procedure. Moreover, even if the matrices are non-degenerate, a simple inversion method is usually not satisfactory and a more sophisticated deconvolution procedure should be adopted (§5.4). Finally, the general problem must be faced accounting

[9] Note that in this section a different notation for incoming, fragmented and detected particles is used.

for the resolution in the detector response. The energy (or rigidity) measurements are also affected by a migration probability (§5.4), given by the smearing matrix

$$S(E_{kn}|E'_{kn}) \sim P(\text{ended in bin } E_{kn}|\text{should be in bin } E'_{kn}\ ) \tag{4.29}$$

Thus, the general convolution problem involves a charge-energy disentanglement procedure, that has to be done by means of solving the following equation:

$$\phi_Z = \sum_{Z'}^{8} \int_0^\infty P(Z|Z')S_{Z'}(E_{kn}|E'_{kn})A_{Z'}(E')\phi_{Z'}(E'_{kn})dE' \tag{4.30}$$

Where $F_{Z''}^{Z'}$ migrations tent to conserve the kinetic energy per nucleon E_{kn}, whereas in $C_Z^{Z''}$ transitions the quantity which is conserved is the one directly measured by the detector (rigidity). Thus an additional energy migration arises from C-matrix corrections, and $||F||$ and $||C||$ should be considered separately. It is worthy of being noticed that an analog problem is found in the WSM description of cosmic ray propagation (§1.2.4). In Eq.1.19 the *nuclear part* $N_j(\mathbf{r})$ is governed by kinetic energy per nucleon (conserved in spallation), whereas the *astrophysical part* $G(\mathbf{r}, x)$ is the same for all species as long as rigidity is considered. This leads to problems in the description of different nuclear species with different A/Z ratio [26, 28].

For these reasons, it has been decided to estimate effects of inelastic collisions and charge contamination directly applying the convolution equation (Eq.4.27) to some theoretical prediction for the CR spectra. The idea is to give a quantitative estimation of the effects with the aim to keep them under control and eventually include them in the systematic errors of the B/C.

The primary spectra $Y_{Z'}(E_{kn})$ are obtained with the `GALPROP` code [20], a numerical model of particle propagation in the Galaxy which incorporates as much realistic astrophysical input as possible together with latest theoretical developments. Propagation calculations for nuclei are performed under a plain diffusion model[10] well tuned to describe existing data (e.g. ACE and HEAO [55, 38]). Influence for the solar activity has been accounted in the force-field approximation (§1.3.1). A modulation parameter $\phi = 450\,MV$ was used, consistent with the period of AMS-01 flight. Although this work is devoted to the measurement of the B/C ratio, all the nuclear species from $Z = 3$ to $Z = 8$ have been considered, as it is required for a thorough study of contamination in the charge reconstruction. Cosmic ray spectra are then calculated for Li, Be, B, C, N and O between $0.1\,MeV/n$ and $50\,GeV/n$, to cover the whole energy range considered in this analysis. The fluxes are illustrated in Fig.4.29 before (black solid curves) and after (blue dashed curves) applying the

[10] `GALPROP` setting $50p\_999726$, available in `http://galprop.stanford.edu/galprop_home`

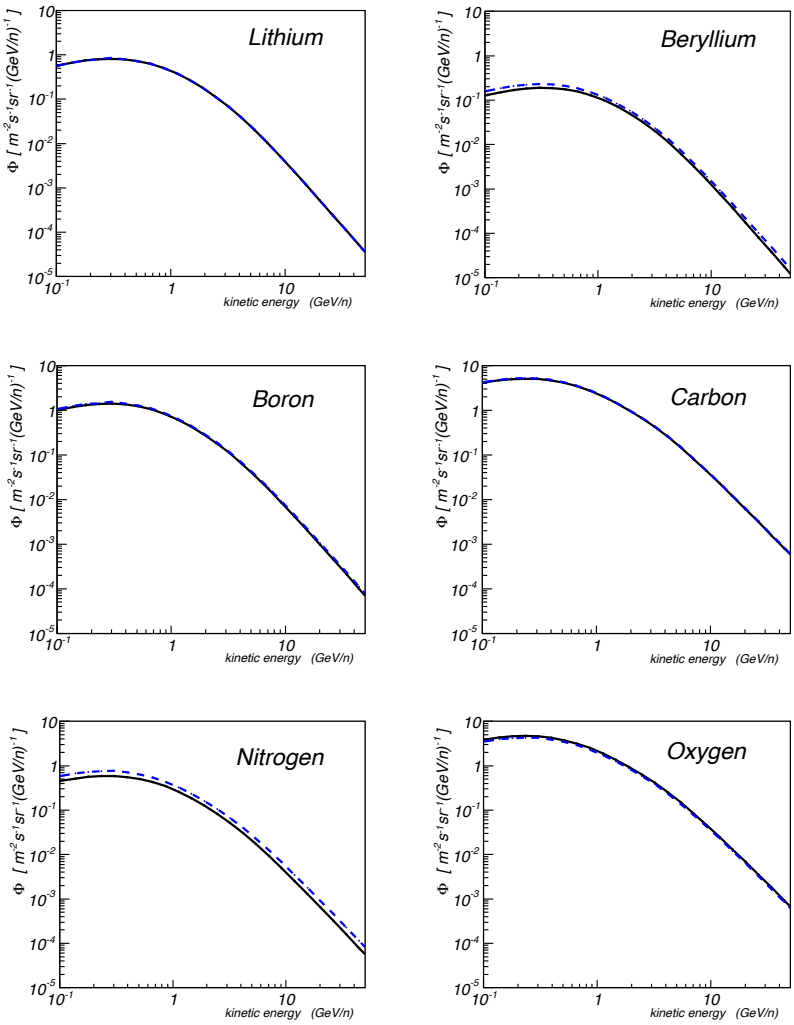

Figure 4.29: Differential energy spectra for Li, Be, B, C, N, O (top left to bottom right) obtained with the GALPROP software. Black solid lines are prediction for a solar activity consistent with the period of AMS-01 flight. Blue dashed lines represents the same distributions after contamination and fragmentation matrices are applied.

$||C||$ and $||F||$ parametrizations. The effect is more visible on the ratios Li/C Be/C, B/C, N/C and O/C. It is presented in Fig.4.30 and quantified in Fig.4.31, where the relative differences before and after contamination are illustrated. Whereas ratios like N/C or O/C result to be heavily influenced, for the B/C ratio the difference between before (labeled CR) and after convolution (labeled AMS) is:

$$\frac{(B/C)_{CR} - (B/C)_{AMS}}{(B/C)_{CR}} \sim 1 \div 9\% \tag{4.31}$$

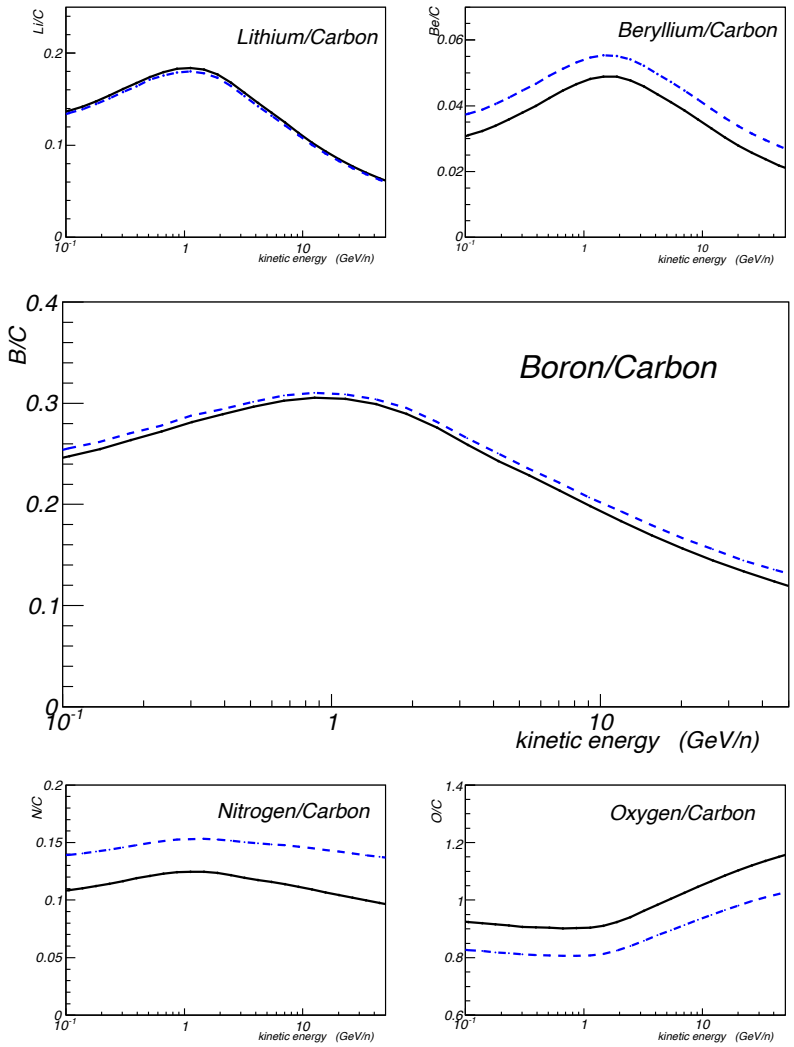

Figure 4.30: X/C ratios of differential energy spectra (X= Li, Be, B, N, O, from top left to bottom right) obtained with GALPROP. Black solid lines are prediction for a solar activity consistent with the period of AMS-01 flight. Blue dashed lines represents the same distributions after contamination and fragmentation matrices are applied.

in the whole energy interval of the AMS-01 measurement. It is not dramatic, but appreciable. In the next chapter (§5.5.2) a thorough analysis of uncertainties will be presented, and the role of contamination in the charge identification will be included and compared with other contributions.

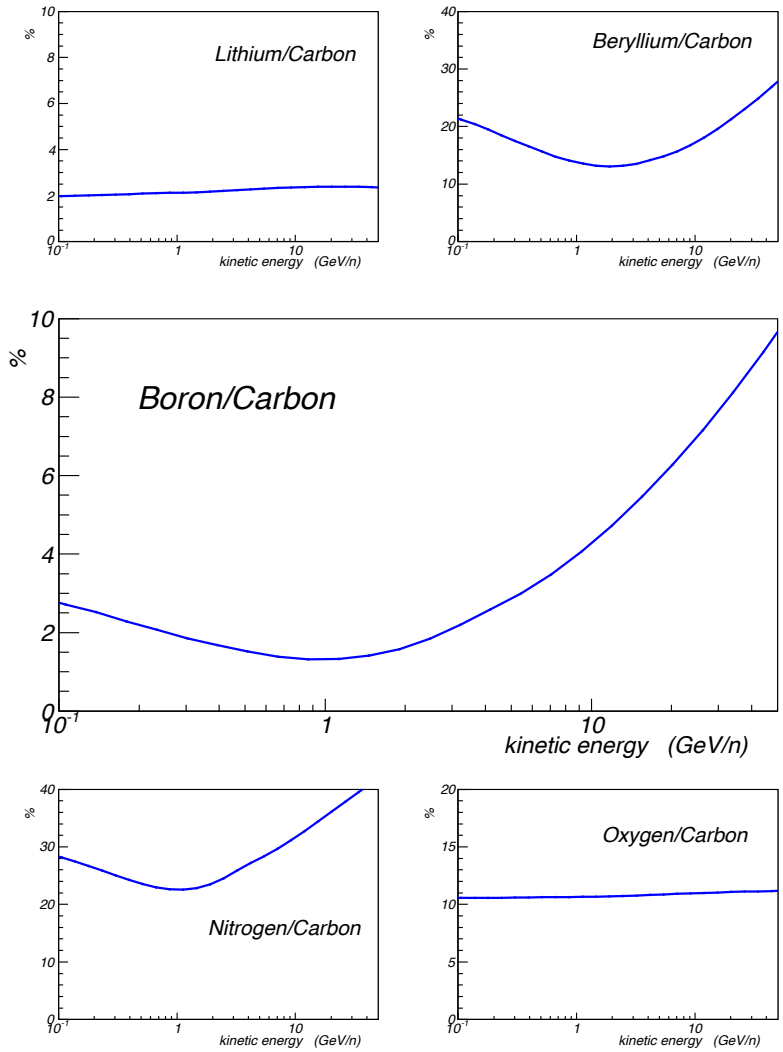

Figure 4.31: Relative differences to the ratios X/C (X= Li, Be, B, N, O, from top left to bottom right) between theoretical distributions provided by GALPROP and expected measured values after application of contamination and fragmentation matrices.

Chapter 5

Flux Determination

In this chapter the B/C flux ratio as a function of kinetic energy per nucleon will be derived. The B/C ratio is simply defined as the ratio of the two differential fluxes:

$$B/C = \Phi^B(E)/\Phi^C(E) \tag{5.1}$$

The measured number of particles entering the AMS-01 spectrometer is defined by recording the energy count histogram ΔN^Z, i.e. the numbers of particles of a certain species Z with kinetic energy per nucleon within the range ΔE around E.
The goal of the cosmic-ray measurements is to convert these detector counts into a spectrum intensity $\Phi^Z(E,\theta,\phi)$ $(s^{-1}cm^{-2}sr^{-1}GeV^{-1})$ as a function of the primary energy E and the incident directions (θ,ϕ) of a specific type of particle. In the following the kinetic energy per nucleon will be called tout-court *energy* E, and Z will be used to indicate the particle charge as well as an index for the particle identity.
In order to reconstruct the cosmic rays intensities on the basis of the particle counts, the following tasks have been undertaken:

- Determination of the detector acceptance $A^Z(E,\theta,\phi)$, which the measured flux has to be corrected for.
- Determination of the detector exposure time in orbit $T^Z(E)$, defined as the overall time spent by the spectrometer for measuring cosmic-ray particles Z in the energy interval ΔE.
- Compensation for the energy losses in the detector material and finite resolution in the measurement of the cosmic-ray primary energies, i.e. spectrum unfolding.

As the primary purpose of this work is to obtain the ratio of the two differential energy spectra Φ^B and Φ^C, all the quantities to be estimated enter in the calculation

as a ratio (i.e. ratio of counts, acceptances, times...) without need to estimate the absolute fluxes. Nevertheless, for sake of clarity, a more general exposition of the flux calculation method will be adopted. In the general case, the equation that relates the detector counts to the external impinging flux is given by:

$$\frac{dN^Z}{dt} = \int_T \alpha(t) H^Z(t,E) dt \int_\Sigma d\hat{\sigma} \cdot \hat{r} \int_\Omega d\omega \int_E S^Z(E_m; E, \omega) \Phi^Z(E, \omega) dE \qquad (5.2)$$

where:

E = true particle energy
E_m = measured energy affected by the spectrometer resolution;
$\hat{d\sigma}$ = oriented element of surface area to be traversed;
Σ = total area of the detector;
$d\omega$ = element of solid angle = $d\phi dcos\theta$ (θ polar angle, ϕ azimuth);
Ω = range of ω, limited by the detector geometry;
$\hat{r}$ = unit vector in direction ω;
$\hat{\sigma} \cdot \hat{r}$ = effective element of area looking into ω;
$\Phi(E, \omega)$ = true impinging flux;
$S(E_m; E, \omega)$ = detector response function;
$\alpha(t)$ = detector live-time (§2.3);
$H^Z(t, E)$ = geomagnetic transmission function;
Z = particle identity.

Although many approximations considerably simplify Eq.5.2, an analytic solution of equation would be extremely difficult to work out. The AMS-01 geometry is complicated by the different sensor arrangements in different tracker planes. Furthermore the particle trajectories are not straight lines due to the bending in the magnetic field. In addition, inefficiencies in the detector responses and interactions of particles with the detector materials produce hard predictable particle-dependent responses. The Monte-Carlo simulation method is the most appropriate way of solving the equation and determining the final spectrum $\Phi^Z(E, \theta, \phi)$ by taking in consideration all the aspects of the problem. These issues are deeply discussed in the next sections, together with the estimation of the different sources of uncertainties that affect the B/C measurement.

5.1 Acceptance Calculation

The detector response function $S^Z(E_m; E, \omega)$ that appears in Eq.5.2 is proportional to the probability of an incoming particles with true kinetic energy E and direction ω to be detected and measured with energy E_m. For an incident distribution of CR particles, the counting rate of any particle detector depends upon the effective dimensions and relative positions of its active sensors as well as the intensity of the radiation in the surrounding space. The proportionality factor between the cosmic-ray intensity and the amount of detected events is called *acceptance*. It represents the gathering power of the instruments.

The acceptance is related to the geometric constraints and the trigger requirements of the apparatus, with no regards to the particular values of the reconstructed quantities, i.e. it must be obtained by summing S over all the measurements:

$$\mathcal{A}^Z(E, \omega) = \int_{E_m} S^Z(E_m; E, \omega) \cdot dE_m \tag{5.3}$$

Thus, the response function S can be split in two distinct parts:

$$S^Z(E_m; E, \omega) = \mathcal{A}^Z(E, \omega) \cdot \mathcal{R}^Z(E_m; E) \tag{5.4}$$

being $\mathcal{R}^Z(E_m; E)$ the detector resolution function, i.e. the normalized probability for a detected particle with energy E to be measured as E_m:

$$\mathcal{R}^Z(E_m; E) = P^Z(E_m|E) \tag{5.5}$$

However, the detection probability of a cosmic ray passing through AMS-01 is also related to non-geometric quantities, as its trajectory in the magnetic field, detector efficiencies, trigger constraints and particle interactions in the material. Everything must be accounted in $\mathcal{A}^Z$.
The integrated acceptance $A^Z(E)$ is determined by the following integration over all the trajectories that satisfy the instrumental constraints of the apparatus:

$$A^Z(E) = \int_\Omega \mathcal{A}^Z(E, \omega) d\omega = \int_\Sigma d\hat{\sigma} \cdot \hat{r} \int_\Omega f\left(\vec{x}_0, \hat{r}, Z, E\right) d\omega \tag{5.6}$$

where $f(\vec{x}_0, \hat{r}, Z, E)$ is a function which takes value $f = 1$ if a particle with energy E and trajectory defined by origin $\vec{x}_0$ and direction $\hat{r}$ crosses the detector producing a trigger ($f = 0$ otherwise). It should be noted that, in Eq.5.6, an explicit dependence on the energy[1] E is shown.

[1] By a geometric point of view, the most appropriated quantity would be the rigidity R, that rules the particle dynamics in the spectrometer. However, all the relevant calculations will be presented in units of kinetic energy per nucleon E.

An efficient approach to integrate Eq.5.6 is to use a Monte-Carlo technique by taking in consideration all the physical aspects that determines $f(\vec{x}_0, \hat{r}, Z, E)$ for each incident particle. It is then necessary to simulate the energy and spatial distribution of the incoming cosmic rays that produce responses in the apparatus.

5.1.1 The Simulation Setup

The general procedure for computing $A^Z(E)$ with a Monte-Carlo simulation is outlined as follows [122]:

1. Choose a random trajectory in the opening aperture according to the intensity of the expected cosmic radiation.
2. Follow this trajectory to see if it passes through the apparatus. All the relevant physical processes must be included in this step.
3. Repeat above steps enough times to let a statistical pattern emerge.
4. The acceptance is given by the ratio between the detected counts and the generated flux.

The simulation is obtained enclosing AMS-01 in a *generation cube* and choosing a random point on its top surface for generating particles according to some momentum and angular distributions. The choice of the volume is arbitrary, so a cube concentric and coaxial with the detector was used, with the edges set in such a way that its top plane covers the entire field of view of AMS-01, i.e. achieving the maximum generation efficiency. This setup is sketched in Fig.5.1. The geometrical acceptance of one cube face for a given aperture Ω is analytically evaluated as:

$$A_0 = \int_\Sigma \int_\Omega d\hat{\sigma} \cdot d\hat{\omega} = \left(\cos^2\theta_2 - \cos^2\theta_1\right) \pi L^2 \tag{5.7}$$

being $L = 3.9\,m$ the cube length and $(\theta_1, \theta_2) = \left(\frac{1}{2}\pi, \pi\right)$ the angular extrema that define the aperture (full hemisphere). The top plane acceptance is then $A_0 = \pi L^2 = 47.78\ m^2 sr$.
Provided that the generated distribution is isotropic in angle, the integrated acceptance $A^Z(E)$ is determined by the ratio between the accepted particles $N_D(E)$ and the generated ones $N_G(E)$:

$$A^Z(E) = \int_{\Delta E} dE \int_\Sigma d\sigma \int_\Omega f\left(\vec{x}_0, \hat{r}, Z, E\right) cos\theta d\theta d\phi = A_0 \frac{N_D(E)}{N_G(E)} \tag{5.8}$$

where a particle is accepted and N_D is incremented whenever $f = 1$. In order to obtain an isotropic intensity, the starting point (x_0, y_0, z_0) and the incoming direction

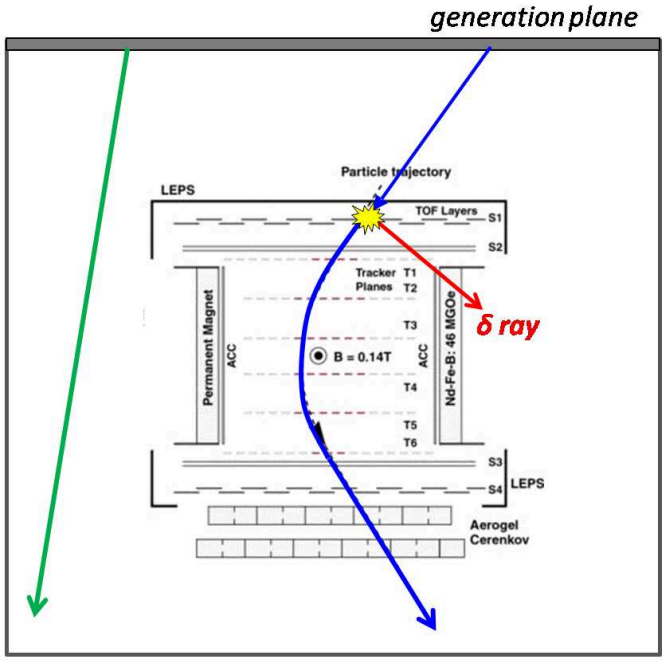

Figure 5.1: Generation cube containing the AMS-01 spectrometer. In the Monte-Carlo simulation, particles are generated on the top surface ($L = 3.9\ m$) toward the downward hemisphere with an isotropic angular intensity. Two not-accepted trajectories are sketched. The green one is clearly out of acceptance. The blue trajectory matches the detector geometry, but the event is rejected by the anti-counter system.

(θ, ϕ) are generated according to the following distribution:

$$\begin{aligned} g(\theta) &= N_\theta sin\theta cos\theta \\ g(\phi) &= \frac{1}{2\pi} \\ g(x) &= g(y) = \frac{1}{L} \end{aligned} \tag{5.9}$$

where $\theta \in \left[\frac{1}{2}\pi, \pi\right]$, $\phi \in [0, 2\pi]$, and $x, y \in \left[-\frac{1}{2}L, \frac{1}{2}L\right]$. The normalization on θ is given by $N_\theta = 2/\left(sin^2\theta_2 - sin^2\theta_1\right)$.
As discussed in §3.2.1, the detector response has been studied with a *probe spectrum* which follows an inverse power law in momentum $dN/dP \propto P^{-1}$. This provides enough high statistics at high energies without overproducing unmanageable size of low-energy events. Different simulations have been run with the program `AMS-GBATCH` (§2.4.2). Details on the MC production are found in Tab.2.2. The

probe spectrum distribution can be then written as:

$$\frac{dN^Z}{d(log_{10}P)dcos^2\theta d\phi} = K^Z \tag{5.10}$$

where the generation constant K^Z is determined for each simulation run from Tab.2.2.

Trigger simulation and reconstruction

Since the number of particle actually detected N_D^Z does not simply relies on the determination of whether a particle crossed the detector or not, the criterion cannot be simply a geometrical one. In fact various effects determine the detector response. The detector acceptance has been studied by simulating offline the full trigger chain from `Level-1l` up to `Level-3` (§2.3), and the higher stages of the event reconstruction (§2.4.1) and detector selection cuts (§3.2). Hence, different acceptances are defined, depending on different conditions:

- **Trigger Acceptance $\mathbf{A_T}$**: accepted events N_D^Z are those surviving the full trigger chain requirements.
- **Reconstruction acceptance $\mathbf{A_R}$**: events accepted by trigger and successfully reconstructed are accounted.
- **Selection acceptance $\mathbf{A_S}$**: trigger, reconstruction and selection cuts are required.

Clearly these three acceptances are related through efficiency factors, i.e.:

$$\begin{aligned} A_R^Z(E) &= \epsilon_R^Z(E) \cdot A_T^Z(E) \\ A_S^Z(E) &= \epsilon_S^Z(E) \cdot A_R^Z(E) \end{aligned} \tag{5.11}$$

where ϵ_R^Z and ϵ_S^Z are the reconstruction and selection efficiencies. The trigger acceptance A_T^Z cannot be simply decoupled in the geometric part A_G^Z and the trigger efficiency ϵ_T^Z, due to the complicated role of interactions in the spectrometer response[2]. These three acceptances are shown in Fig.5.2 for Boron and Carbon nuclei. Acceptances are found to depend on charge and to decrease with increasing energy. This behaviour is mainly due to the trigger conditions against multi-particle events (e.g. ACC veto), that are influenced by secondary emission, as δ-rays or fragmentation products. Fig.5.1 gives the idea of such events (blue trajectory). Next section is devoted to shed light on this effects. It should also be noted that the quantity that

[2]For example, for a particle trajectory that does not satisfy the geometric constraints of the detector, the particle is able to produce a trigger.

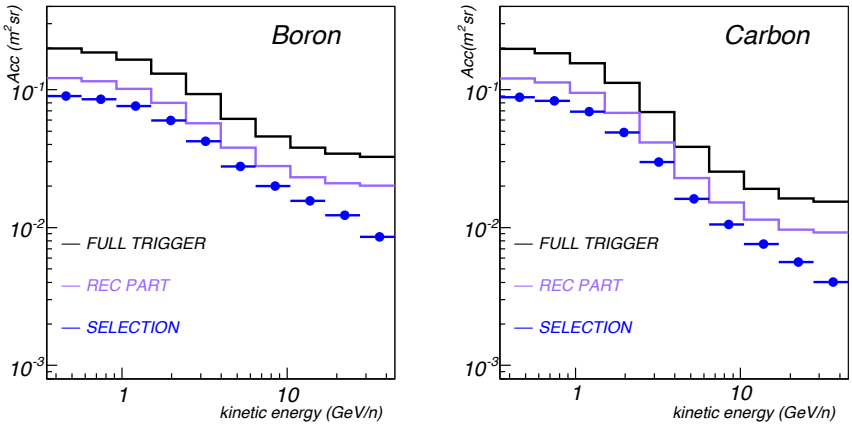

Figure 5.2: Detector acceptances for Boron (left) and Carbon (right) as a function of kinetic energy per nucleon E. For each simulation, the trigger acceptance A_T (black), reconstruction acceptance A_R (purple) and selection acceptance A_S (blue) have been computed. Only particles within 32° of aperture from the negative z-axis have been considered.

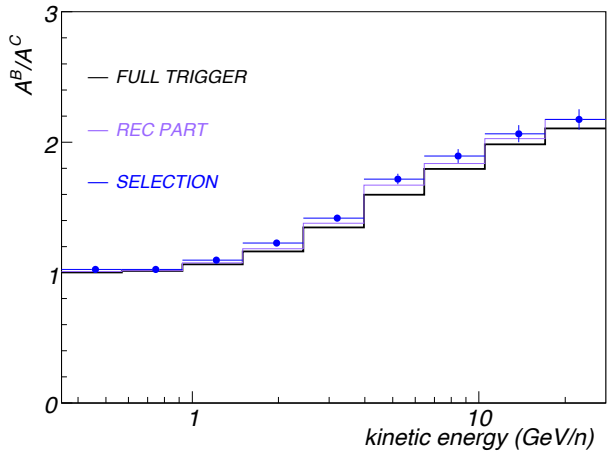

Figure 5.3: Ratio of acceptances A^B/A^C as a function of kinetic energy per nucleon E at the trigger (black), reconstruction (purple) selection level (blue). Only particles within 32° of aperture from the negative z-axis have been considered.

enter in the B/C is the ratio of the acceptances A^B/A^C, shown in Fig.5.3, rather than their absolute values. The deviation of this ratio from unity, more pronounced at high energy, is already visible at the trigger level. This behaviour is clearly due to the non-geometrical part of the acceptances, i.e. on the trigger efficiencies. In the

fluxes calculation, the selection acceptance (hereafter just acceptance) will be used:

$$A_S^Z(E) = \epsilon_S^Z(E) \cdot \epsilon_R^Z(E) \cdot A_T^Z(E) \tag{5.12}$$

Indeed the reconstruction as well as the selection efficiencies must be considered in the flux calculations.

5.2 Trigger Efficiency

The efficiency of the trigger system is included in the acceptance A^Z, which is estimated by the Monte-Carlo program `AMS-GBATCH`. For a more solid estimation, this task should be ideally done with the help of measured data. For this purpose, during the data taking, a certain fraction of *prescaled events* is collected with the application of a dedicated *unbiased trigger* (§2.3). Clearly a full acceptance estimation is impossible to work out using only measured data (as the incident flux is unknown a priori), and even the *unbiased data* are obviously net of the unbiased trigger (whose efficiency is not directly measurable). Nonetheless, these data are particular helpful for validating the Monte-Carlo simulation or performing corrections to the higher trigger levels, if needed

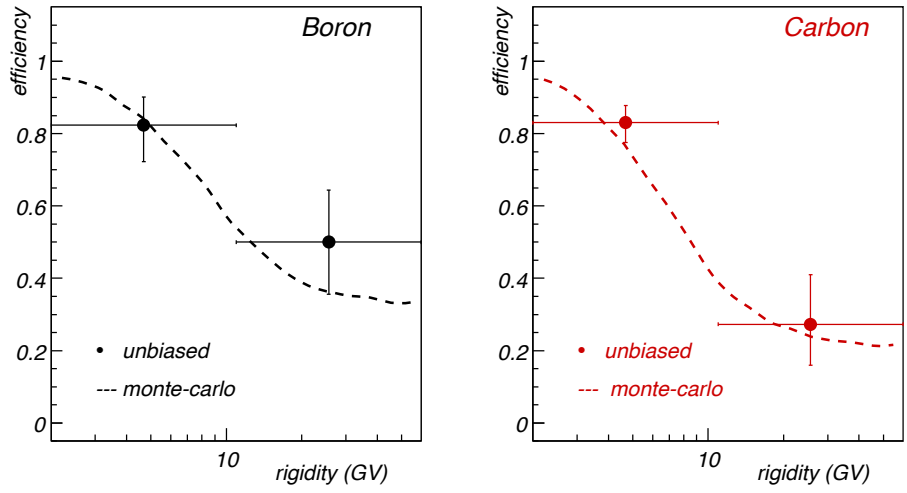

Figure 5.4: Estimation of the total trigger efficiency as a function of the rigidity for Boron (left) and Carbon (right). Within statistical errors the Monte-Carlo simulation (dashed lines) describes the behaviour of the data (solid markers). A sharply decreasing efficiency with increasing rigidity and increasing charge is observed. 27 (60) unbiased Borons (Carbons) events have been used.

The efficiency calculations are based on the comparisons of two histograms, the former representing the distribution of the quantities of interest for a reference sample of data Y, the latter plotting the same quantity but only for those events satisfying the selection criterion under study X. The general strategy is to define a set of efficiencies $\epsilon = P(X|Y)$, where the reference sample imposed by Y must satisfy the fulfillment according to the quantities that are accessible to the unbiased trigger. In order to explore energy or charge dependence of the detector efficiencies, reconstruction must also be requested on Y. These efficiencies have then to be compared with the same as obtained with the MC simulation, with the aim to perform a global tuning of the whole acceptance.
During the STS-91 flight, one out of 1000 fast trigger events was entirely recorded by AMS-01 regardless to the fulfillment of the remaining trigger conditions (§2.3). Whereas these events permitted a thorough study of the various efficiencies in case of protons, electrons, and helium nuclei, this is unfortunately not the case for higher charges. Indeed, only 237 downward-going particles are recorded as unbiased and properly reconstructed for $Z > 2$. This statistics is clearly insufficient for a charge by charge determination of any efficiency. For instance, Fig.5.4 shows the efficiency of the full trigger ϵ^{TRIG} for detected Boron (left) and Carbon (right) nuclei as a function of the rigidity. Unbiased data (solid markers) are shown together with the corresponding MC efficiencies (dashed line). This efficiency is net of `TOF` trigger conditions (§2.3) and reconstruction (§2.4.1):

$$\epsilon^{TRIG} = P(\text{TRIGGER} \mid \text{TOF} + \text{REC}) \tag{5.13}$$

The error bars are assigned based on applying Bayes theorem [123]. Within errors the Monte-Carlo simulation describes the behaviour of the data. A decreasing efficiency with increasing rigidity and increasing charge is clearly observed. However, due to the poor statistics for unbiased data (only 27 B and 64 C enter in the plot) no quantitative conclusions can be inferred. For this reason, in this work the B and C trigger efficiencies have to be estimated by means of the simulation only.
In order achieve a more realistic description of the ion interactions in the spectrometer, the MC simulation program has been interfaced with the `RQMD` hadronic package [95], a transport code specifically designed to describe nuclear interactions. Fig.5.4 indicates a rigidity and charge dependence of the total trigger efficiency that can be understood qualitatively in some details. For instance, the `Level-3` veto on the Anti-counter system is clearly charge and rigidity dependent. Indeed the number of δ-rays emitted from an incident nucleus along its path is proportional to Z^2 (Fig.5.5).The higher energetic tail of these secondary electrons leave the detector hitting the anti-coincidence wall. The role inelastic collisions of CR nuclei might also be an additional cause of the inefficiencies in the trigger response. It is then apparent that the resulting acceptances/efficiencies are affected by the physical processes that depends on the nuclear species.

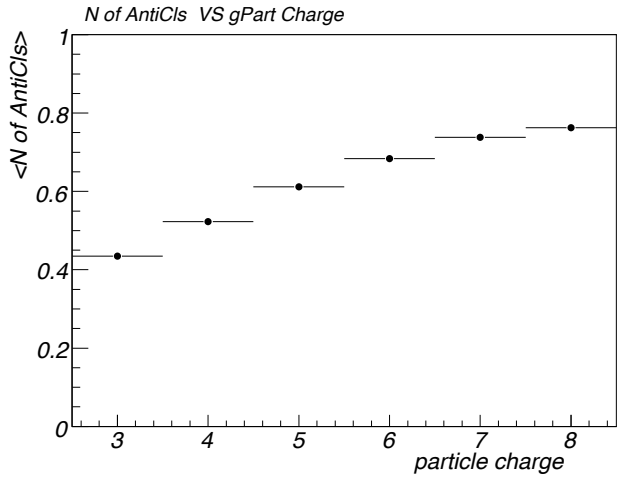

Figure 5.5: Average number of ACC clusters as a function of the injected charge. An increasing behaviour with increasing charge is observed, as the number δ-rays emitted from an incident particle along its path rises with increasing charges.

5.2.1 A Virtual MC Application for AMS-01

The interactions of cosmic-ray nuclei with the detector material play an important role in the observed behaviour of the trigger efficiency. Since it has been completely estimated with the Monte-Carlo simulation `AMS-GBATCH`, this estimation is clearly model dependent. Therefore, this study has been reinforced by running additional simulations, with the aim to validate the acceptance estimation under different physics models of particle interactions. The general aim of this work has been to reach a deeper knowledge of the AMS-01 trigger in order to keep under control the systematic errors related to its efficiency. The specific goal is to quote the systematic errors on the trigger efficiency. For this reason, a Virtual Monte-Carlo application has been implemented for AMS-01.

The concept of Virtual Monte-Carlo (`VMC`) has been developed in order to allow different Monte-Carlo simulation programs to run without changing the user code [97], such as the geometry definition, the detector response simulation and the input/output formats. `AMS-VMC` software has been developed into the `ROOT` framework [98]. The three most popular particle transport codes `GEANT3`, `GEANT4` and `FLUKA` have been implemented under `AMS-VCM` (§2.4.2).

The simulated detector responses under different interaction models have then been compared and better understood. The relevant points of this work are the following:

1. Detector geometry and materials.

2. Primary particle generation.
3. Physics processes.
4. Digitization and detector response.
5. Trigger setting.

The detector geometry design and the material list have been imported from `AMS-GBATCH` and converted in a suitable format. The magnetic field map, as well as the support structure and the shuttle airframe have also been implemented. The generation of

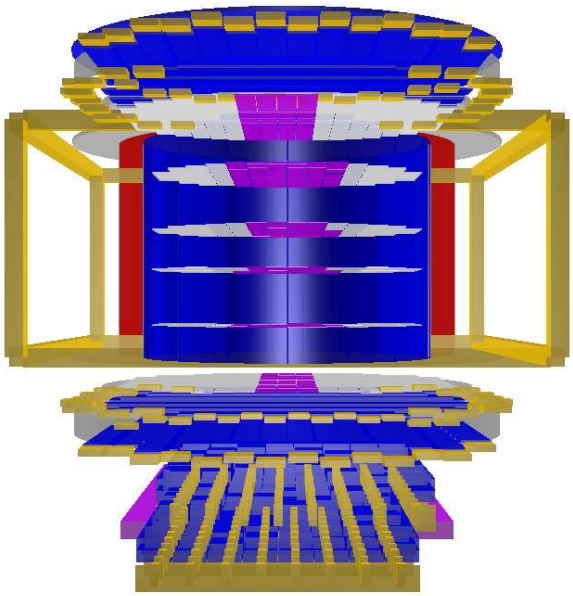

Figure 5.6: AMS-01 geometry under VMC. The whole spectrometer design and the corresponding material list have been imported under VMC geometry classes, as well the support structures and the shuttle airframe.

incident nuclei has been defined under the `MC-Stack` interface, using the PDG encoding [5] for the particle static properties (Z, A). The simulation setup and the generation features of the primary particles are exactly the same as described in §5.1. The propagation of charged particles in the matter under is described under `AMS-VMC` in the usual way through the stepping functions method, whereas the details of the physical processes included in the simulation (multiple scattering, ionization, fragmentation, etc.) are specific of each particular transport code (§2.4.2). Under `VMC-GEANT3`, the electromagnetic processes (e.g. ionization, δ-ray emission)

are well described, but the description of heavy ion fragmentation ($Z > 2$) can be introduced only by interfacing other physics packages (e.g. RQMD, used in GBATCH). The virtualized GEANT4 simulates the hadronic processes through the Binary Cas-

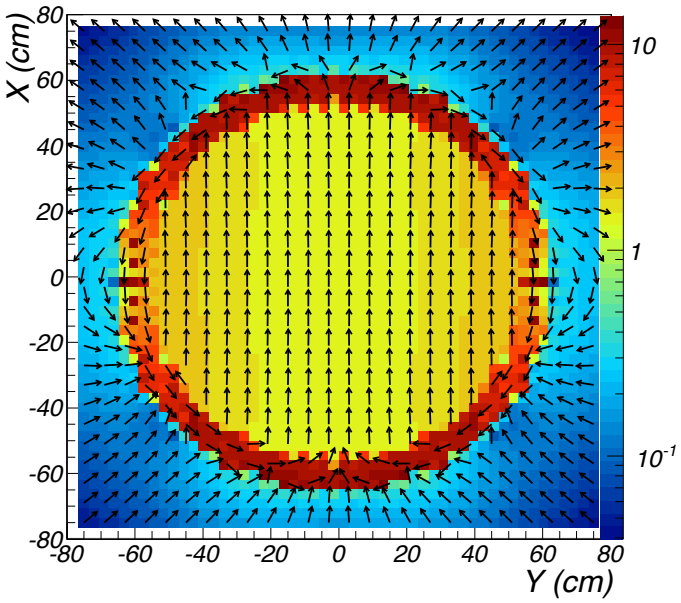

Figure 5.7: Horizontal cross section of the magnetic field distribution in KG unit.

cade interaction model [100]. FLUKA uses RQMD between 0.1 and 5 GeV/n, and the DPMJET hadronic package above 5 GeV/n [101].
An effective digitization of the signals has been modeled in the active material of the TOF and ACC scintillators. The transition between the ionization processes and the formation of the charge clusters in the various sub-detectors has been described by performing an integration over all the energy depositions of the particles in the materials. The attenuation of the fluorescence light along the scintillator paddles has been described as indicated in Fig.5.8 (left), and the relation between the energy loss and the photon yield (Birks' law) has also been considered (right). The relevant parameters that define these behaviours have been chosen as in AMS-GBATCH. These functions are based on experimental calibration measurements performed on the detector during the pre-flight testing phase. The mechanism of photon detection and the subsequent multiplication of the photo-electrons up to the formation of the electrical pulse have not been simulated: the attenuated signal has been simply converted in a read-out response. The response of the silicon tracker has not simulated in this work, and the event reconstruction is therefore missing, as the primary goal of this study is to understand the AMS-01 response at the trigger level. The lack

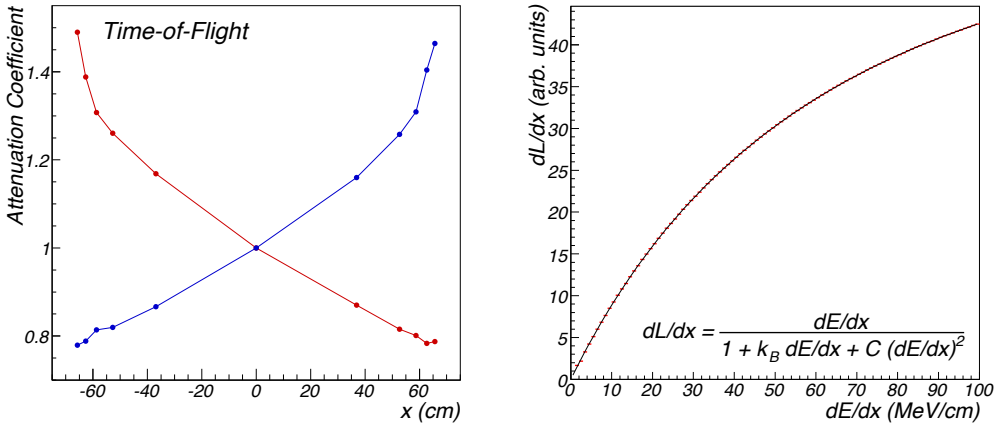

Figure 5.8: Left: attenuation factors of the TOF light signals as a function of the coordinate along the scintillator paddle x. For each paddle, two distinct functions have been used to describe the signals in each of the two read-out. These parameters are based on experimental calibration measurements performed on the detector during the pre-flight testing phase (solid markers). Right: the relation between the energy loss in the scintillators and the fluorescence photon yield has been described according to the Birks' law. The adopted parameters are imported from `AMS-GBATCH`.

of these parts and the simple assumptions in the digitization are the limits of this work, that is planned to be improved in the future developments.

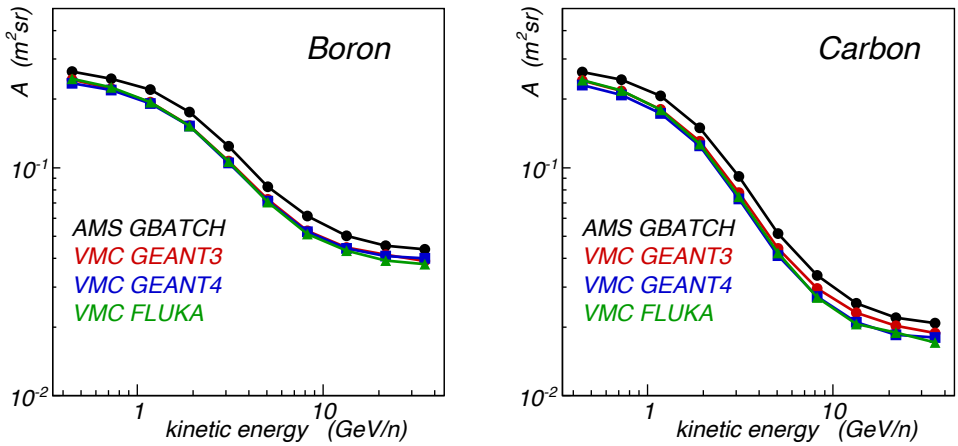

Figure 5.9: Trigger acceptances A_T^B and A_T^C obtained with `GEANT3` (red points), `GEANT4` (blue squares) and `FLUKA` (green triangles) under the `VMC` simulation and compared with `AMS-GBATCH` (black points).

After the responses of the various sub-detector are generated, the read-out signals have been combined to reproduce the trigger logic (§2.3). This part is identical to

the simulated one by AMS-GBATCH[3].

Since VMC-GEANT3 was built using the same physics engines as AMS-GBATCH (i.e. GEANT-3.21 and RQMD-1.07), the two programs would lead in principle to the same detector response and in particular the same trigger acceptances, up to intrinsic differences related to the digitization. In fact VMC-GEANT3 has been used as a control interface for tuning the VMC digitization parameters according to the response produced by AMS-GBATCH. This procedure was very CPU-time consuming: in order to reach a reasonable agreement in the response (i.e. within the errors of the finite MC statistics), a large amount of simulated data have been produced[4] and repeatedly processed.

The resulting trigger acceptances A_T^B and A_T^C are shown in Fig.5.9. The black curves on the top are those obtained with AMS-GBATCH (§5.1). The colored curves are estimated with GEANT3 (red points), GEANT4 (blue squares) and FLUKA (green triangles) under the VMC simulation. The virtualized VMC-GEANT3 acceptances are computed using the same transport codes as AMS-GBATCH (both of them interfaced with RQMD-1.07), i.e. the black and red curves, in principle, should be identical. The observed differences are due to the digitization performed in this work, that does not consider inefficiencies and fluctuations in the photo-multiplication mechanism. This is particularly important in the Anti-counter detectors, where the amount energy deposition is generally small[5] (i.e. produced by $|Z| = 1$ secondary particles). As a consequence, the efficiency of the Anti-counter becomes overestimated, i.e. the efficiency of the whole trigger is underestimated, being the ACC signals used as veto. This is not particularly relevant for the aim of this work. In fact this inefficiencies are charge independent, and they play no role in checking the stability of the detector simulation under different interaction models.
The ratio of the trigger acceptances $\eta \equiv A_T^B/A_T^C$ is the most appropriate quantity for our purposes. A good level of description has been reached in reproducing η under the VMC framework. Fig.5.10 shows the ratio η_{G3}/η_{GB}, i.e. between η calculated under VMC-GEANT3 and that obtained with AMS-GBATCH. The two are consistent within $\sim$2 %. As η is the real quantity that enters in the measured B/C, the systematics on the trigger efficiency can be evaluated observing its distribution among the different models. This is shown in the right panel for VMC-GEANT3 (red), VMC-GEANT4 (blue) and VMC-FLUKA (green). The envelope of the three considered curves defines an uncertainty band related to our estimation of the trigger efficiency (§5.5.2).

[3]With the exception of the Level-3 tracker-trigger that has not been simulated under AMS-VMC

[4]VMC statistics for B and C is comparable with that on Tab.2.2, as the goal was to obtain similar acceptance responses within the statistical errors.

[5]On the contrary, this is less important in the TOF paddle, where the energy depositions are typically larger, as they come from primary nuclei.

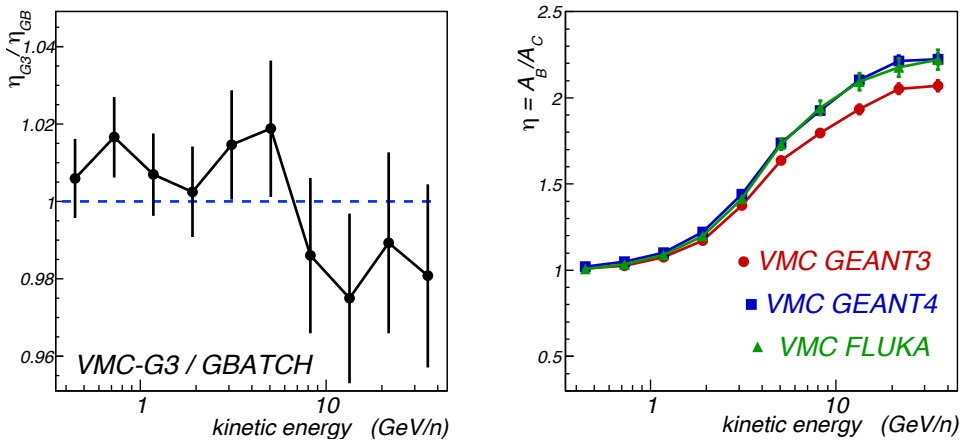

Figure 5.10: Left: ratio between η_{G3} (computed with `VMC-GEANT3`) and η_{GB} (from `AMS-GBATCH`). The desired level of agreement between the two simulation ($\sim$ 2%) have been reached for the quantity η. Right: Distribution of η estimated with `VMC-GEANT3` (red point), `VMC-GEANT4` (blue squares) and `VMC-FLUKA` (green triangles) under the `AMS-VMC` application. η is defined as the ratio A_T^B/A_T^C. The simulation is described in the text.

5.3 The Exposure Time

The exposure time is defined as the effective data-taking duration with AMS-01 operational and ready for receiving a new trigger. In the computation of the exposure time in orbit, it has to be taken into account the *dead time* of the instrument as well as any orbit-dependent feature that may affect the accessibility of the detector to cosmic rays. This is the case for the geomagnetic field (GMF) modulation (§1.3.2) that screens the low energy charged particles depending on the detector position along the orbit.

According to Eq.5.2 and assuming an isotropic cosmic-ray flux (integration over the solid angle has been performed as discussed in §5.1), the total number of detected and selected particles of a given species (labeled Z) collected over the data taking is expressed by the following relation:

$$N^Z = \int_T \alpha(t) H^Z(t,E) dt \int_E \Phi^Z(E) A^Z(E) \Re^Z(E_m, E) dE \tag{5.14}$$

Assuming an ideal detector resolution in the energy determination, i.e. $R(E_m, E) \equiv \delta(E_m - E)$ (the real case is discussed in Section § 5.4), for a finite energy binning, the differential energy spectrum is:

$$\Phi^Z(E) = \frac{\Delta N^Z(E)}{\Delta E \cdot A^Z(E) \cdot \Delta T^Z(E)} \tag{5.15}$$

where $\Delta T^Z(E)$ is the exposure time for the particle Z in the energy bin ΔE. All the orbit-dependent conditions that influence the detection must be included in ΔT^Z, i.e. the DAQ live-time fraction (α) and the GMF modulation that prevent low energy particles from reaching the spectrometer (H^Z):

$$\Delta T^Z(E) = \int_T \alpha(t) H^Z(t, E) dt \tag{5.16}$$

Time integration to evaluate the exposure time is not trivial due to the rigidity cut-off that varies continuously along the orbit. Particles have been selected after imposing a minimal rigidity threshold $R^{Th} = 1.2 \cdot R_{VC}$, with $R_{VC} = (15\,GV)/\mathcal{R}^2 cos^4\lambda$ (§3.3). This cut is qualitatively illustrated in Fig.5.11, where the distribution of

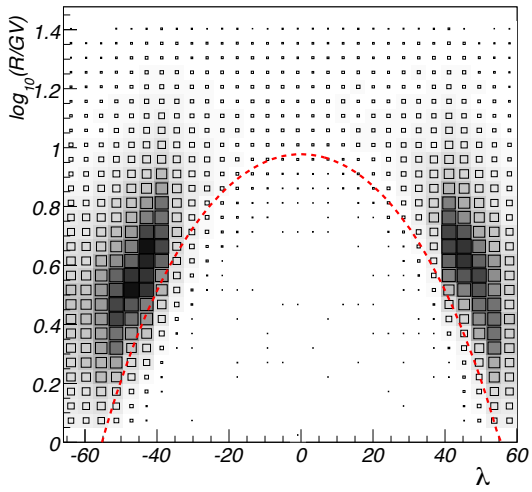

Figure 5.11: Distribution of the measured rigidity R as a function of the detector position along the geomagnetic latitude λ. The $cos^4\lambda$ dependence of the Störmer cut-off (Eq.3.3) is represented by the dashed line. For sake of clearness, $\mathcal{R}$ is kept fixed to unity.

the measured rigidity R is plotted as a function of the detector position along the geomagnetic latitude λ. The $cos^4\lambda$ dependence of the Störmer cut (Eq.3.3) is represented by the dashed curve (for sake of clearness, $\mathcal{R}$ is kept fixed to unity)[6].

The effect of the GMF modulation in the measured fluxes can be better understood by dividing the orbit in geomagnetic bins $(\lambda_i, \mathcal{R}_j)$ with associated rigidity thresholds $R^{Th}_{i,j}$. Thus, a corresponding set of fluxes $\Phi^Z_{i,j}(E)$ can be obtained. As an

[6] It is important to remember that this rigidity cut-off is naturally imposed by the Earth magnetosphere, but it is reinforced in this analysis to compensate for the limited GMF description in the vertical Störmer model.

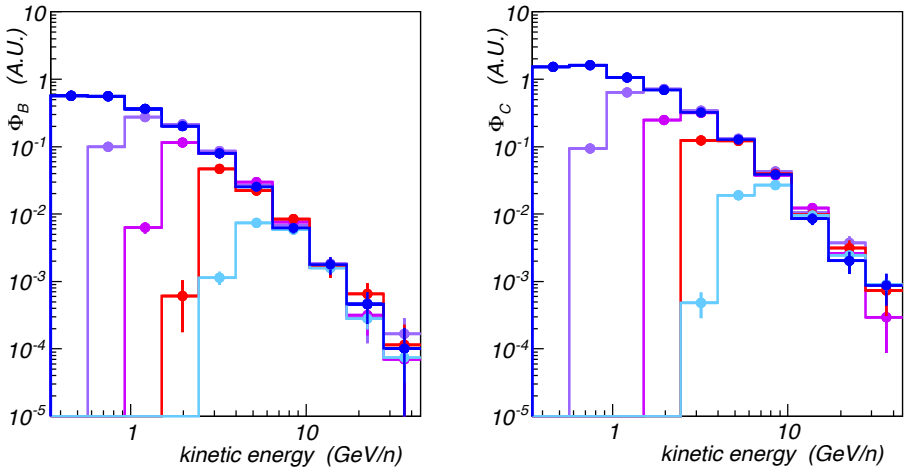

Figure 5.12: Differential energy spectra Φ_i^B at different geomagnetic latitudes λ_i. Moving from the geomagnetic poles ($|\lambda| > 30°$, french blue) toward the equator ($|\lambda| < 9°$, light blue), it is apparent the effect of the geomagnetic cut-off on the energy distribution.

example of this procedure, Boron and Carbon fluxes Φ_i^B and Φ_i^C for five intervals of geomagnetic latitude λ_i are shown in Fig.5.12 (the weaker dependent binning on the radius $\mathcal{R}$ is not considered in this example). The five geomagnetic intervals considered are defined by the following sequence:

$$|\lambda| \in \{0°,\ 9°,\ 15°,\ 22°,\ 30°,\ 60°\} \tag{5.17}$$

Moving from the geomagnetic poles ($|\lambda| > 30°$, french blue) toward the equator ($|\lambda| < 9°$, light blue), it is apparent the effect of the geomagnetic cut-off on the energy distribution, as a consequence of the geomagnetic modulation.

However, the goal of this analysis is to obtain the galactic fluxes Φ^B and Φ^C. The approach consisted in computing $\Delta T^Z(E)$ according to its definition (Eq.5.16). The procedure is outlined as follows:

- The entire orbit has been divided in $45,000$ time intervals of $\delta t \sim 10s$.
- For each time bin δt_k, a mean value of R_k^{Th} is computed.
- For each time window δt_k, the trigger live-time fraction α_k is also known.
- The exposure time $\Delta T^Z(E)$ is then calculated for each particle Z, rigidity R and energy $E \in \Delta E$ as:

$$\Delta T^Z(E) = \sum_k \alpha_k \cdot H_k^Z(R, R_k^{Th}) \cdot \delta t_k \tag{5.18}$$

where $R = \left(\frac{A}{Z}\right)\sqrt{E^2 + 2M_pE}$, $H = 1$ for $R > R^{Th}$, and $H = 0$ for $R < R^{Th}$, i.e. the sum is extended to only the time windows *above cut-off* according to the Störmer formula. The trigger live-time α_k is the fraction of time when the AMS-01 spectrometer is operational for triggering. α_k is affected by the incident rate of cosmic-ray, i.e. it depends on the geomagnetic region; however its value is directly measured by the detector DAQ system (Fig.2.12 in §2.3). Following the above prescription for

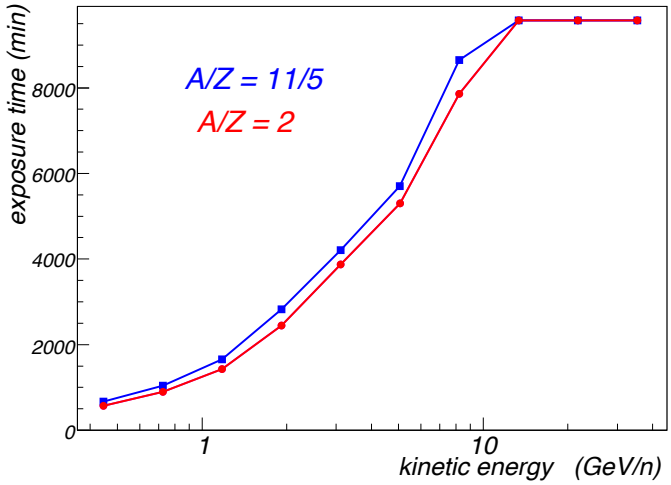

Figure 5.13: Exposure time above cut-off as a function of kinetic energy per nucleon of the incident particles with $A/Z = 2$ (e.g. ^{10}B and ^{12}C, red points) and for particles with $A/Z = 11/5$ (^{11}B, blue squares).

each species, the energy spectra can be normalized directly from Eq.5.15.

It is clear from Eq.5.18 that the resulting exposure time in units of kinetic energy per nucleon is different for different A/Z isotopes[7]. The exposure time above cutoff as a function of the kinetic energy E is shown in Fig.5.13 for the $A/Z = 2$ particles (like ^{12}C and ^{10}B, red line) and for $A/Z = 11/5$ (^{11}B, blue line). This behaviour is easily understandable: during the total data taking period T, the time $\Delta T^Z(E)$ for which a cosmic ray of given rigidity (energy) can reach the spectrometer from the outer space is a continuously increasing function of the rigidity (energy), saturating at $\sim \overline{\alpha} \cdot T$ ($\sim 0.8 \cdot 175h \sim 8,500\ min$) for particles above $R \approx 1.2 \cdot M_0 = 18\ GV$ ($\sim 15\ GeV/n$).

[7] See discussion in §5.5.1.

5.4 Energy Losses and Resolution

The relation between the measured energy of a detected particle and its true energy is one aspect which one has to deal with in order to keep under control all elements that determine the differential energy spectrum of the cosmic-ray nuclei.

A method to correct for this effect has therefore to be devised. Different algorithms exist in literature [124, 125], that consist in the deconvolution of the detector resolution function $\mathcal{R}(E_m, E)$. This issues belong to the class of ill-posed problems, and the chance to yield a suitable solution occur as long as the measured energy E_m is reasonably close to the true energy E.
Since energy losses produce systematic shifts toward lower energies, i.e. the corresponding matrix elements may be found off the diagonal, it was decided to split this problem in two distinct tasks.
First, a statistical correction to the measured energy is performed to compensate for the energy loss, regardless the resolution in the measurement. Successively, a closer inspection on the smearing effects due to the instrumental resolution have been done. This second aspect has been treated using unfolding techniques.

5.4.1 TOI Corrections

As a particle traverses the spectrometer, it gradually looses energy due to interactions with the active and passive material. The reconstructed rigidity (or energy E_{REC}) is therefore systematically lower than the rigidity (or energy E_{TOI}) at the Top Of the Instrument (TOI). The exact amount of energy loss for a given nucleus

detector element	**description**	**composition**	$\langle X_0 \rangle$
MLI thermal blanket	composite (e.g. mylar)	$C_5H_4O_2$	0.7 g/cm^2
LEP shield	carbon fiber	C	1.3 g/cm^2
TOF scintillator	Bicron BC0408	$C/H = 1$	2.1 g/cm^2
TOF support structure	alluminium honeycomb	Al	1.0 g/cm^2

Table 5.1: List of material above the silicon tracker [113]. In the last column the surface density is averaged over the angle of incidence.

depends on the integrated amount of matter traversed by the particle along its trajectory. The matter located above the silicon tracker is summarized in Table 5.1. The estimation of the energy loss has been performed through the Monte-Carlo simulation, by means of comparison between the measured energy E_{REC} with the true energy E_{TOI}. Since this correction turned out to be important only for low energy particles, the comparison is done using velocity β measured with the TOF, since it

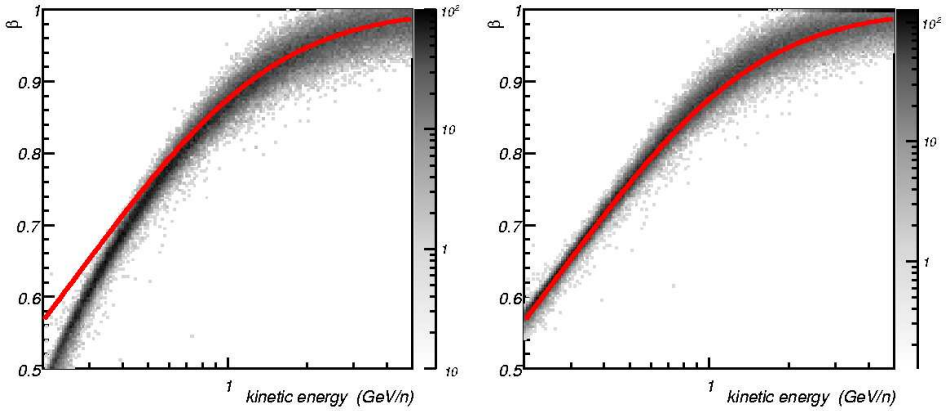

Figure 5.14: Distribution of the measured velocities β against the TOI kinetic energy per nucleon for a Carbon MC sample. The red line represents the ideal relation between E_{TOI} and β_{REC} for an ideal *transparent* detector. The distribution is shown before (left) and after (right) the TOI corrections. The corrected distribution lies along the ideal line with an unavoidable dispersion due to the finite resolution on the system.

is more precise than the tracker in measuring energy[8] below few hundred MeV/n. Fig.5.14 shows the distribution of the measured velocities β against the TOI kinetic energy per nucleon for a Carbon nuclei sample. The red line represents the TOI velocity as a function of the kinetic energy E_{TOI}

$$\beta_{TOI} = \frac{\sqrt{E_{TOI}^2 + 2M_p E_{TOI}}}{E_{TOI} + M_p} \tag{5.19}$$

i.e. what an ideal detector would measure if no energy losses occurred. It is apparent, on the left panel, a systematic shift toward lower velocities that has been corrected statistically through an effective function. The right picture shows the same distribution after compensation of the energy loss is performed. The corrected distribution lies along the ideal line with an unavoidable dispersion due to the finite resolution on the system.

5.4.2 Resolution Smearing

After the correction to the measured energy presented in the previous section, a deeper investigation will now performed. Due to the finite rigidity and velocity resolution of the instrument, a particle with a given energy E is generally detected at a different energy E_m with a probability P.

[8] This particular is not important in this specific task, as the correction is applied for the energy losses with no regard to the instrumental resolution.

$P = P^Z(E_m|E)$ is given by the resolution function $\mathcal{R}^Z(E_m, E)$ (§5.1), that parametrizes our knowledge of the detector response. Fig.5.15 gives an idea of the problem. The

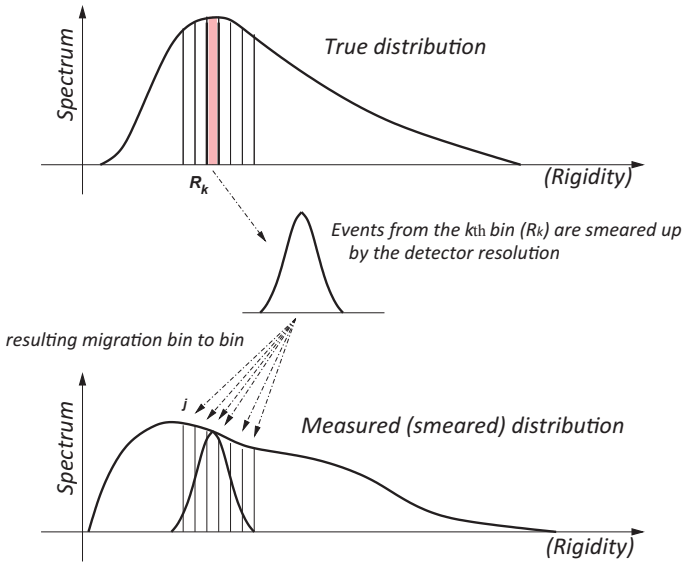

Figure 5.15: The scheme illustrates the effect of the finite resolution in the measurement of a generic spectrum [126]. The events coming from each given energy bin are smeared up in several bins, affecting the measured distribution.

original spectrum $g(E) = dN/dE$ is obtained from the observed spectrum $f(E_m)$ by solving the Fredholm equation:

$$f(E_m) = \int_E \mathcal{R}^Z(E_m, E) g(E) dE \tag{5.20}$$

In this work the data counts are histogrammed with a uniform logarithmic binning in energy from $E_0 = 0.35\ GeV/n$ and $E_1 = 45\ GeV/n$. The Fredholm equation is then reduced to a algebraic equation:

$$\epsilon_m^i = \sum_j M_{i,j}^Z \epsilon^j \tag{5.21}$$

where $\epsilon_{\mathbf{m}}$ and ϵ are the energy vectors corresponding to the measured and original spectra to be determined, and $\mathbf{M^Z}$ is the resolution matrix, i.e. the discretized resolution function $\mathcal{R}^Z$, whose elements express the probability of a bin-to-bin migration. The matrix elements have been estimated with the Monte-Carlo simulation program, which applies the events reconstruction procedures to an initial probe spectrum of particles. $\mathbf{M^B}$ and $\mathbf{M^C}$ (for Boron and Carbon) are shown in Fig.5.16, where the kinetic energy E_m is measured with the silicon Tracker. Since the energy-loss correction have been already performed, the energy smearing is found to be substantially

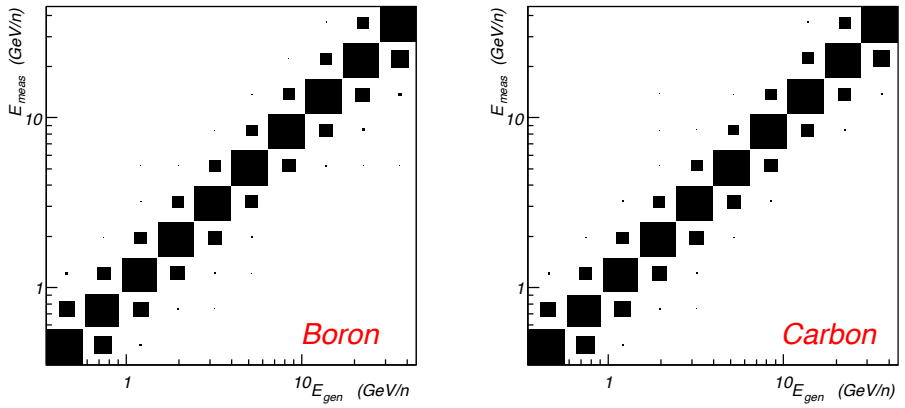

Figure 5.16: Matrix representation of the Tracker resolution function $\Re^Z(E_m, E)$ in kinetic energy units for $Z = 5$ (left) and $Z = 6$ (right). Each matrix element gives the migration probability between the *true* energy and the measured energy affected by the spectrometer resolution. These matrices are normalized such that $M_{i,j} = P(E_i|E_j)$. Quite symmetric and diagonally-dominated responses have been found from the Tracker.

symmetric around the diagonal. As it was already pointed out in a previous study [113], the shape of the resolution function is log-rigidity and charge independent for all the $Z > 2$ ions. Finally, off-diagonal elements are small compared to those on-diagonal, since the energy bin withs have been chosen large with respect to the detector energy resolution.
This is not the case for measurements with the TOF system. In Fig.5.17 the same resolution matrices are shown, with the E_m computed from measured time of flight (i.e. β^{-1}). It is clear that the velocity is not a good parameter for determining the energy spectra above $\sim 2\ GeV/n$, as $\beta \to 1$ and the time resolution becomes dominating.

The procedure of correction of the distortion in the spectrum (solving equations 5.20 and 5.21) is known as *unfolding*. Even if the matrices $\mathbf{M}$ are invertible, a simple inversion is not satisfactory in general, because of the presence of negative bin contents which are physical meaningless.
Thus, an unfolding algorithm has been developed. The method is based on the Bayes approach and consists in an iterative *forward folding* procedure. It is outlined as follows:

1. Start with an arbitrary $g^0(E)$.
2. Apply Fredholm equation (Eq.5.20) to get $f^1(E_m)$.
3. Compare $f^1(E_m)$ with the measured $f^0(E_m)$; define $w^1 \equiv \frac{f^0}{f^1}$

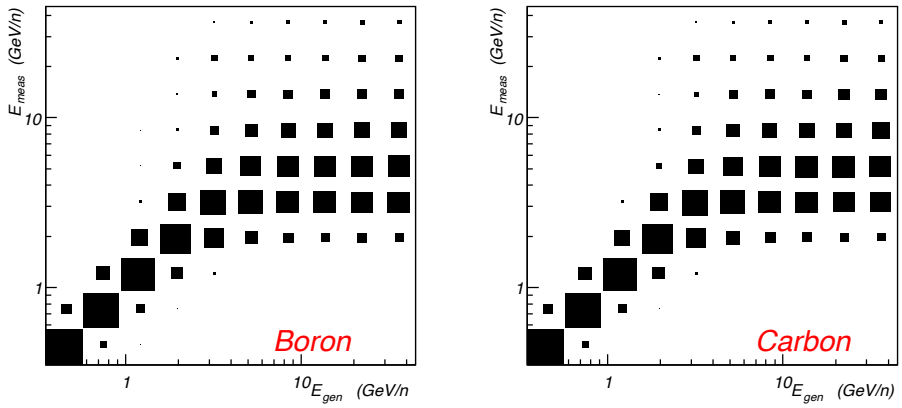

Figure 5.17: Matrix representation of the TOF resolution function $\mathcal{R}^Z(E_m, E)$ in kinetic energy units for $Z = 5$ (left) and $Z = 6$ (right). Each matrix element gives the migration probability between the *true* energy and the measured energy affected by the spectrometer resolution. These matrices are normalized such that $M_{i,j} = P(E_i|E_j)$. It is clear the limitation of the TOF system in measuring relativistic particles.

4. Scale g^0 accordingly: $g^1(E) = w^1(E) \cdot g^0(E)$.

5. Repeat the above steps using the new $g(E)$.

The procedure has to be repeated as long as the convergence is observed. After n iterations:

$$\begin{aligned} f^n(E_m) &= \int \mathcal{R}(E_m|E) \cdot g^{n-1}(E) \cdot dE \\ g^n(E) &= g^0(E) \cdot \frac{[f(E_m)]^n}{\prod_{j=0}^{n} f^j} \end{aligned} \tag{5.22}$$

For a large number of iterations ($n \to \infty$):

$$\begin{array}{ll} f^n(E_m) \to f(E_m) & \text{(measured spectrum)} \\ w^n(E) \to 1 & \text{(convergence)} \\ g^n \to G(E) & \text{(solution)} \end{array} \tag{5.23}$$

As a test, the algorithm as been validated with simulated spectra for Boron and Carbon. Fig.5.18 shows the unfolded energy distribution (blue points) superimposed to the generated spectra (dashed line) together with those reconstructed (solid line). The algorithm has been applied to the measured B and C energy spectra individually (measurements come from Tracker). The result is shown in Fig.5.19, where the unfolded spectrum is indicated with the red markers and compared with the

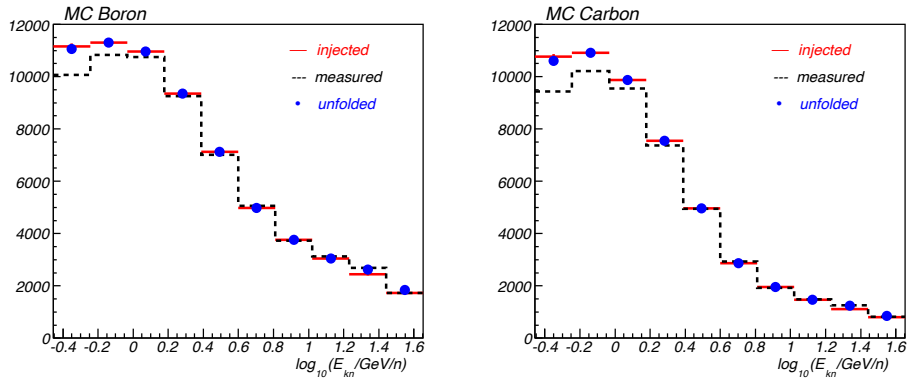

Figure 5.18: Validation of the unfolding algorithm with simulated power-law spectra for Boron (left) and Carbon (right). The unfolded energy distributions (blue markers) are plotted together with the injected spectra (dashed line) and those reconstructed (solid line).

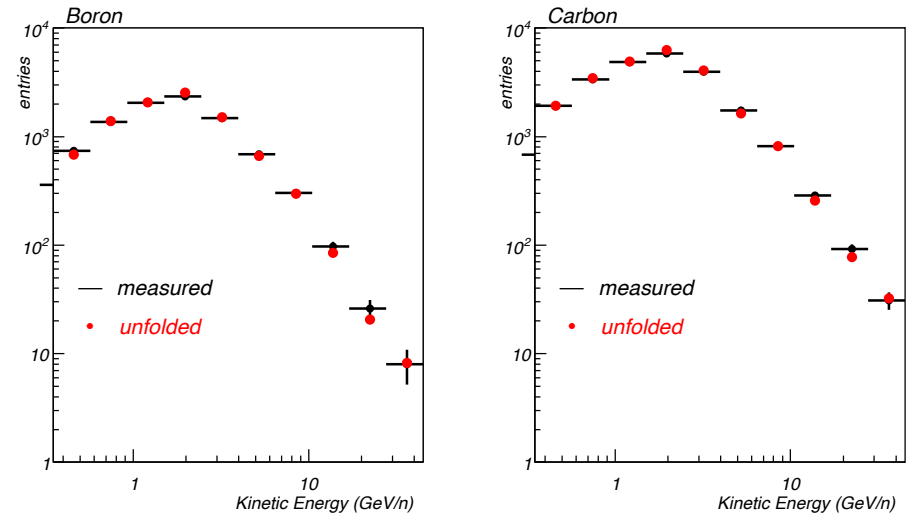

Figure 5.19: Measured spectrum before (black histogram) and its corresponding unfolded spectrum (red markers) with the AMS-01 flight data. Due to the relatively large energy binning used in this study, the final smearing effects are small.

measured energy spectrum (black histogram). Due to the large binning used in this study, the final smearing effects are barely appreciable after the unfolding.
Furthermore, the corrections act in a very similar way for the two species, i.e. the overall effect is mostly canceled out in the ratio: the relative differences before and after corrections turned out to be smaller than the statistical errors on the B/C (§5.5.2).
Since there are no methods of compensating for this smearing effect without intro-

ducing errors of the same order of magnitude as the corrections, the effect is quoted as a systematic uncertainty instead of performing a correction. The relative difference between measured and unfolded B/C ratio is then regarded as a source of systematic error (§5.5.2).
It should be noted that the convergence properties of this algorithm are not mathematically warranted, but, as a matter of fact, it is satisfactory after few (~ 12) iterations. On the other hand, the algorithm fails with the energy spectrum obtained with the time of flight, due to the abnormal response on the high energetic bins (Fig.5.17).

5.5 The B/C Ratio

All the relevant quantities that enter in the calculation of the cosmic ray differential energy spectra have been described. The last step is putting all together in order to obtain a the B/C ratio and its corresponding uncertainties. This is the subject of the present section.

5.5.1 The Isotopic Composition

The particle identity has been specified so far by the charge Z. The role of the isotopic composition on the B/C measurement is now discussed. The Boron to Carbon ratio is meant as the distribution of their isotopes:

$$B/C = \frac{\phi^{10B} + \phi^{11B}}{\phi^{12C} + \phi^{13C}} \approx \frac{\phi^{10B} + \phi^{11B}}{\phi^{12C}} \tag{5.24}$$

since the abundance of ^{13}C is thought to be negligible component of the cosmic-ray Carbon. On the contrary, a more consistent fraction of ^{10}B is expected in the cosmic rays compared with its isotopic composition at Earth, so that a $^{10}B - {}^{11}B$ isotopic mixture must be considered in B/C. This can be understood regarding cosmic-ray Borons as a direct product of Carbon spallation over the interstellar hydrogen. Fragmentation cross sections of ^{12}C on a proton target at $E \sim 4\ GeV/n$ are estimated as [121, 127]:

$$\begin{aligned} \sigma(\,^{12}C + p \rightarrow\ ^{10}B + ...) &= (12.3 \pm 3.0)\ mb \\ \sigma(\,^{12}C + p \rightarrow\ ^{11}B + ...) &= (27.7 \pm 0.7)\ mb \end{aligned} \tag{5.25}$$

For the following, it is convenient to define the Boron isotopic fraction:

$$Y_B = \frac{\phi^{10B}}{\phi^{10B} + \phi^{11B}} \tag{5.26}$$

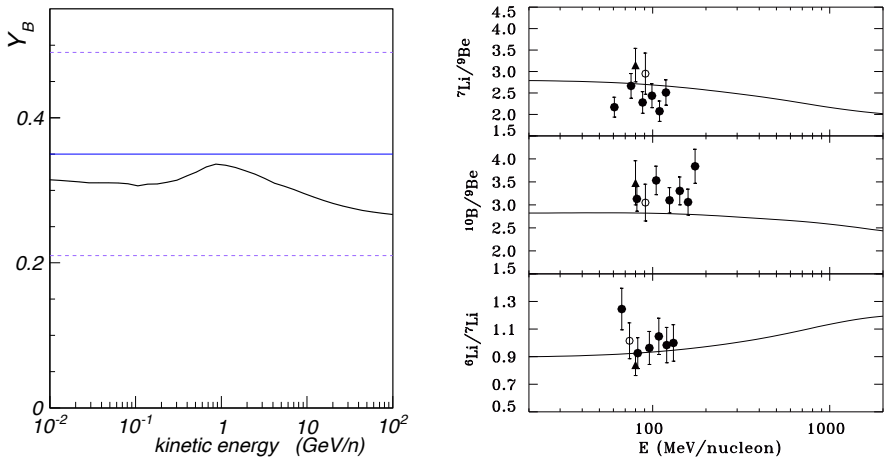

Figure 5.20: Left: Boron isotopic composition Y_B as predicted with GALPROP. The composition assumed in this work is indicated by the blue solid line, together with the uncertainty band, defined by the dashed lines. Right: isotopic ratios of $^6Li/^9Be$, $^{10}B/^9Be$ and $^6Li/^7Li$ in the sub-GeV region from GALPROP and compared with existing data [128, 129, 63].

The presence of an isotopic mixing ^{10}B - ^{11}B in the cosmic rays has to be accounted in the measurement. Indeed, this is the first measurement of the B/C made with a magnetic spectrometer, for which the physical quantity directly measured is the rigidity R. In order to compare results with other experiments and theoretical models, it has been decided to present the B/C ratio in units of kinetic energy per nucleon E. Thus, in the computation of the boron spectrum, the measured rigidities R must be converted into energies E using:

$$E(R) = E^{A,Z}(R) = \sqrt{\left(\frac{Z}{A}\right)^2 R^2 + M_p^2} - M_p \tag{5.27}$$

where the exact conversion is fully specified by the knowledge of the nuclear charge Z and the mass number[9] A. Since the isotopic separation is not achievable by the AMS-01 spectrometer, the exact value of A is not available event by event. Thus, an opportune conversion $R \rightarrow E$ has to be done according to some necessary assumption on Y_B. The uncertainty on its knowledge has also to be accounted in the final measurement. For instance, starting from a rigidity power-law spectrum $\phi(R) \equiv kR^{-\gamma}$, the converted kinetic energy spectrum $\phi(E)$ results:

$$\phi(E) = k\left(\frac{A}{Z}\right)^{1-\gamma}(E + M_p)\left[E^2 + 2EM_p\right]^{-\frac{\gamma+1}{2}} \approx \left(\frac{A}{Z}\right)^{1-\gamma} E^{-\gamma} \tag{5.28}$$

[9] In Eq.5.27 it was assumed $M = A \cdot M_p$, being M_p the proton mass.

thus, for $Z = 5$ and $\gamma = -2.6$, the assumption $A \equiv 10$ (pure ^{10}B) instead of $A \equiv 11$ (pure ^{11}B) produces a relative difference of $\sim 20\%$ on the spectrum intensity. According to the existing literature on measurements of cosmic-ray isotopes and theoretical models (e.g. [130, 63, 128]), it has been used $Y_B \equiv 0.35 \pm 0.15$, that is a quite conservative assumption over all the energy range of interest. Fig.5.20, left, shows the isotopic ratio Y_B as a function of the energy as predicted with `GALPROP`. The horizontal lines represent value assumed here with and the related uncertainty level.

This problem does not only deal with the presentation of the results. The mass number A enters also in the exposure time ΔT^Z, which has to be determined as a function of the kinetic energy per nucleon: in Eq.5.18 the mass number A must be specified for the computation of the rigidity. In principle, even the acceptance $A^Z(E)$ is isotope-dependent, as the nuclear interactions in the detector material affect the chances of a given nucleus to be detected and measured, and some physical processes (e.g. fragmentation) depend on the mass number A, i.e. on the particular isotope[10]. Therefore, in order to account for this effect in the measurement a statistical procedure has been devised. The method is explained as follows.
Given an isotopic fraction Y_B, the Boron energy spectrum can be written as $\phi^B = \phi^{10} + \phi^{11}$, where:

$$\begin{aligned} \phi^{10} &= Y_B \cdot \phi^B \\ \phi^{11} &= (1 - Y_B) \cdot \phi^B \end{aligned} \tag{5.29}$$

The number of Boron nuclei detected by AMS-01 in the energy bin ΔE is then the sum of the isotopes $\Delta N^B = \Delta N^{10} + \Delta N^{11}$, with:

$$\begin{aligned} \Delta N^{10} &= \phi^{10} \cdot A^{10} \cdot \Delta T^{10} \cdot \Delta E \\ \Delta N^{11} &= \phi^{11} \cdot A^{11} \cdot \Delta T^{11} \cdot \Delta E \end{aligned} \tag{5.30}$$

where A^{10} and A^{11} are the selection acceptances for the two species (§5.1), ΔT^{10} and ΔT^{11} the corresponding exposure times (§5.3). The isotopic fraction of *detected* Boron events can be defined as:

$$\alpha_B = \frac{\Delta N^{10}}{\Delta N^{10} + \Delta N^{11}} \tag{5.31}$$

Provided that Y_B reflects the composition of Boron in the cosmic radiation, α_B is the corresponding composition convoluted with the measurement made by AMS-01,

[10] As a matter of fact, the detector acceptance is isotope-independent. Extensive simulations have been performed with ^{10}B and ^{11}B Boron isotopes and no significant differences in the corresponding acceptances have been found.

i.e. after the modulation of the geomagnetic field and the detector response.

Even though ^{10}B and ^{11}B isotopes are not directly identifiable by the spectrometer, an estimation of α_B can be computed from Y_B by substituting Eq.5.30 in Eq.5.31:

$$\alpha_B = \frac{Y_B \cdot A^{10} \cdot \Delta T^{10}}{Y_B \cdot A^{10} \cdot \Delta T^{10} + (1 - Y_B) \cdot A^{11} \cdot \Delta T^{11}} \tag{5.32}$$

As a matter of fact, $\alpha_B \approx Y_B$ with good approximation.

For a single particle detected as Boron ($Z_{rec} = 5$), α_B can be interpreted as the probability to be a ^{10}B isotope:

$$\begin{aligned} P(\,^{10}B | Z_{rec} = 5) &= \alpha_B \\ P(\,^{11}B | Z_{rec} = 5) &= 1 - \alpha_B \end{aligned} \tag{5.33}$$

The method used for the calculation of the Boron spectrum $\Phi^B(E)$ taking into account the isotopic mixing $^{10}B - {}^{11}B$ is illustrated as follows.

1. An assumption on Y_B is made together with its uncertainty δ_{Y_B} (0.35 ± 0.15). The corresponding α_B and δ_{α_B} are derived (Eq.5.31).

2. For each energy interval ΔE, two rigidity windows ΔR^{10} and ΔR^{11} are defined according to the relationship:

$$R(E) = R^{A,Z}(E) = \left(\frac{A}{Z}\right) \sqrt{E^2 + 2M_p E} \tag{5.34}$$

3. Nuclei selected and identified as Boron ($Z_{rec} = 5$) are counted in ΔR^{10} and ΔR^{11}, so that two distinct count histograms $\Delta\tilde{N}^{10}$ and $\Delta\tilde{N}^{11}$ are defined.

4. According to Eq.5.33, the numbers of detected ^{10}B and ^{11}B are:

$$\begin{aligned} \Delta N^{10} &= \alpha_B \cdot \Delta\tilde{N}^{10} \\ \Delta N^{11} &= (1 - \alpha_B) \cdot \Delta\tilde{N}^{11} \end{aligned} \tag{5.35}$$

5. The differential energy spectra for ^{10}B and ^{11}B are then computed:

$$\begin{aligned} \phi^{10} &= \frac{\Delta N^{10}}{A^{10} \cdot \Delta T^{10} \cdot \Delta E} = \alpha_B \tilde{\phi}^{10} \\ \phi^{11} &= \frac{\Delta N^{11}}{A^{11} \cdot \Delta T^{11} \cdot \Delta E} = (1 - \alpha_B)\, \tilde{\phi}^{11} \end{aligned} \tag{5.36}$$

where selection acceptances $A^{10}(E)$ and $A^{11}(E)$ have been estimated (§5.1) using Monte-Carlo samples of pure ^{10}B and pure ^{11}B isotopic sample. The exposure times above cut-off $\Delta T^{10}(E)$ and $\Delta T^{11}(E)$, given by Eq.5.18 (§5.3), are those illustrated in Fig.5.13 (ΔT^{10} in blue and ΔT^{11} in red).
The Boron energy spectrum is then given by $\Phi^B = \phi^{10} + \phi^{11}$. The Carbon spectrum is calculated in the usual way assuming $\Phi^C \equiv \phi^{\,^{12}C}$, i.e.:

$$\Phi^C(E) = \frac{\Delta N^C}{A^C \cdot \Delta T^C \cdot \Delta E} \tag{5.37}$$

so that the B/C ratio is finally obtained.

5.5.2 Error Breakdown

The uncertainties on the measurement will now be presented in terms of relative errors on the B/C ratio. For each energy bin, the quantity:

$$\epsilon_{B/C} = \frac{\delta_{B/C}}{B/C} \tag{5.38}$$

has been computed. A set of distinct error sources contribute to the overall uncertainty:

1. Statistics from measured data.
2. Monte-Carlo statistics in the acceptance estimation.
3. Contamination due to particle mis-identification.
4. Smearing due to detector resolution.
5. Uncertainty on the trigger efficiency.
6. Uncertainty on the Boron isotopic composition.

Statistical uncertainties arise from fluctuations in the counts recorded in each energy interval associated to E. The corresponding error for each energy bin is poissonian:

$$\begin{aligned} \delta^B_{STAT} &= \sqrt{\Delta N^B} \qquad \delta^C_{STAT} = \sqrt{\Delta N^C} \\ \epsilon_{STAT} &= \sqrt{\left(\frac{\delta^B_{STAT}}{\Phi^B}\right)^2 + \left(\frac{\delta^C_{STAT}}{\Phi^C}\right)^2} \end{aligned} \tag{5.39}$$

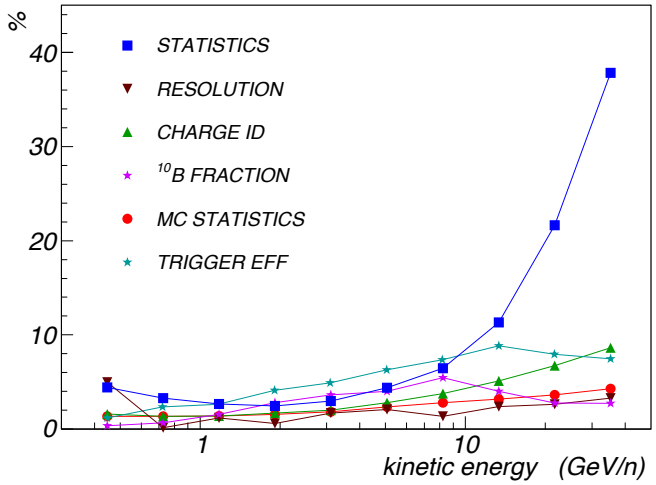

Figure 5.21: Relative errors on the B/C ratio. The contributions from statistics from data, Monte-Carlo statistics, contamination on the charge ID, resolution smearing, isotopic composition and trigger efficiency are shown as a function of the kinetic energy per nucleon.

The Monte-Carlo statistics contributes with a systematic error according to the binomial distribution:

$$\delta^B_{MC} = \sqrt{\frac{\eta^B\left(1-\eta^B\right)}{N^B_G}} \qquad \delta^C_{MC} = \sqrt{\frac{\eta^C\left(1-\eta^C\right)}{N^C_G}}$$
$$\epsilon_{MC} = \sqrt{\left(\frac{\delta^B_{MC}}{\Phi^B}\right)^2 + \left(\frac{\delta^C_{MC}}{\Phi^C}\right)^2} \tag{5.40}$$

being $\eta^Z = N^Z_D/N^Z_G$ the ratio between detected and injected particles (§5.1).
The systematic due to the contamination on the particle identification is given from Eq.4.31:

$$\epsilon_{PID} = \frac{|(B/C)_{CR} - (B/C)_{AMS}|}{(B/C)_{CR}} \tag{5.41}$$

as discussed in §4.9, where the effects of the contamination and fragmentation in the identification of B and C have been investigated in the whole energy range.
The uncertainties introduced by the finite spectrometer resolution (§5.4.2) are also given by the relative differences between the B/C ratio values obtained before and after correction for the spectrum unfolding.
A similar method has been used to compute the systematic error on the trigger efficiency. Trigger efficiency enters in the B/C in term of acceptance ratio η (§5.1.1). Correction on η have been presented in Section §5.2.1 for two different interaction

models. Hence, the two corresponding acceptances have been used to estimate the deviation produced in the B/C ratio under different interaction models:

$$\epsilon_{TRIG} = \max\left(\epsilon_{G4},\ \epsilon_{FL}\right) \tag{5.42}$$

with

$$\epsilon_{G4} = \frac{\left|(B/C)_{G4} - (B/C)_{G3}\right|}{(B/C)_{G3}} \quad \epsilon_{FL} = \frac{\left|(B/C)_{FL} - (B/C)_{G3}\right|}{(B/C)_{G3}} \tag{5.43}$$

where $(B/C)_{G3}$ is obtained using the acceptances from the `GEANT3`-based simulation program. $(B/C)_{G4}$ and $(B/C)_{FL}$ are those obtained with `VMC-GEANT4` and `VMC-FLUKA` applications developed for the purpose (§2.4.3). The resulting error on the B/C reflects the uncertainty band in the acceptance ratio η defined by the envelope of the three curves (Fig.5.10, right).
The systematic errors coming from the assumption on the isotopic composition on the Boron spectrum are estimated by varying the isotopic mixing parameter Y_B between $Y_1 = Y_B - \delta_{Y_B}$ and $Y_2 = Y_B + \delta_{Y_B}$ and calculating the corresponding spread in the B/C.
Since the Boron energy spectrum has been defined as the mixing of ^{10}B and ^{11}B spectra, the above error contributions have been evaluated for both the isotopes and then combined together for a unique uncertainty δ^B. The quantities $\tilde{\phi}^{10}$ and $\tilde{\phi}^{10}$ that appear in Eq.5.36 are affected by uncertainties $\tilde{\delta}^{10}$ and $\tilde{\delta}^{11}$, to be computed with the above prescriptions. Since the estimated ϕ^{10} and ϕ^{11} are obtained from exactly the same data-set (under a different assumption), they are strongly correlated and the combined error on the sum Φ^B is to be given according to:

$$\left(\delta^B\right)^2 = \left(\delta^{10}\right)^2 + \left(\delta^{11}\right)^2 + 2\rho\delta^{10}\delta^{11} \tag{5.44}$$

being ρ the correlation coefficient, $\delta^{10} = \alpha_B\tilde{\delta}^{10}$ and $\delta^{11} = (1-\alpha_B)\tilde{\delta}^{11}$. Thus, assuming maximum correlation $\rho \equiv 1$, the isotopic-mixed error is finally given by:

$$\delta^B = \alpha_B\tilde{\delta}^{10} + (1-\alpha_B)\,\tilde{\delta}^{11} \tag{5.45}$$

The overall uncertainty ϵ_{TOT} is obtained as the squared sum of all the contributions[11] ϵ_i. All the uncertainties are summarized in Fig.5.21, where each ϵ_i is plotted as a function of kinetic energy per nucleon from 0.35 GeV/n up to 45 GeV/n. The overall uncertainty ranges from $\sim 4\%$ to $\sim 38\%$ of the B/C. Its behaviour is substantially increasing with energy, and mostly dominated by the statistical errors, especially at high energy.

[11] Note that some contributions (3 and 5 in the list) lead to asymmetric uncertainties on the B/C. Asymmetric errors will therefore be quoted in the final measurements.

5.5.3 Results and Discussion

The B/C nuclear ratio is finally presented in ten data points between 0.35 and 45 GeV/n. For the transition from energy bin to data point, since data are binned uniformly in $\log E$, the reference value $\langle E_i \rangle$ for each energy bin $[E_i, E_{i+1}]$ has been chosen as the geometric mean of each the energy interval:

$$\langle E_i \rangle \equiv \sqrt{E_i \cdot E_{i+1}} \tag{5.46}$$

and the B/C values are consequently defined for each energy interval as the ratios $B/C = \Phi^B(E_i)/\Phi^C(E_i)$.
The high energy limit has been set according to the requirement of reasonable statistics. At low energy, the limit is imposed by the selection acceptance, that exhibits a sharp decrease below 0.35 GeV/n (§3.2.6).

As a consistency check of the results, in Fig.5.22 the B/C measurement obtained with the tracker (red) is superimposed to a distinct estimation[12] made with the TOF (blue). This is extended up to few GeV/n of energy, due to the limited TOF reso-

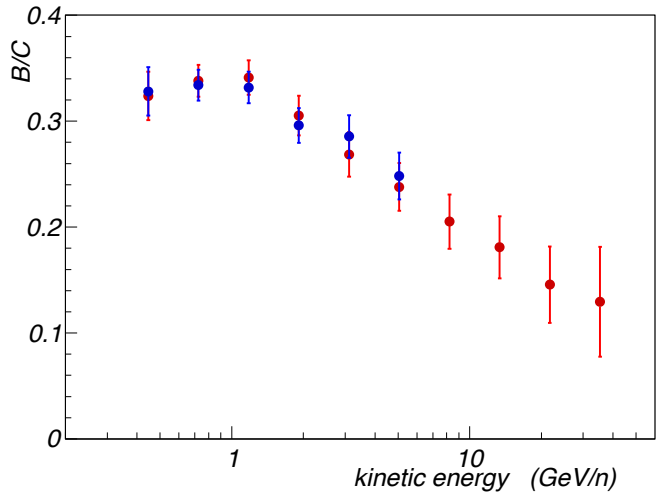

Figure 5.22: B/C ratio obtained with Tracker measurements between 0.35 and 45 GeV/n (red) in comparisons with that measured with the TOF between 0.35 and 5 GeV/n (blue) The two measurements are in substantial agreement.

lution as $\beta \to 1$, and no resolution errors are included, as the unfolding procedure did not converge for this kind of measurement (§5.4.2). It is also worthy of being

[12] The two measurements, made with Tracker and TOF, are not strictly independent as they come from the same data sample obtained by imposing the same selection. Nonetheless the two distinct measurements represent a significant consistency check.

noticed that this measurement is barely affected by the isotopic composition, as the TOF performs a direct measurement of kinetic energy per nucleon.

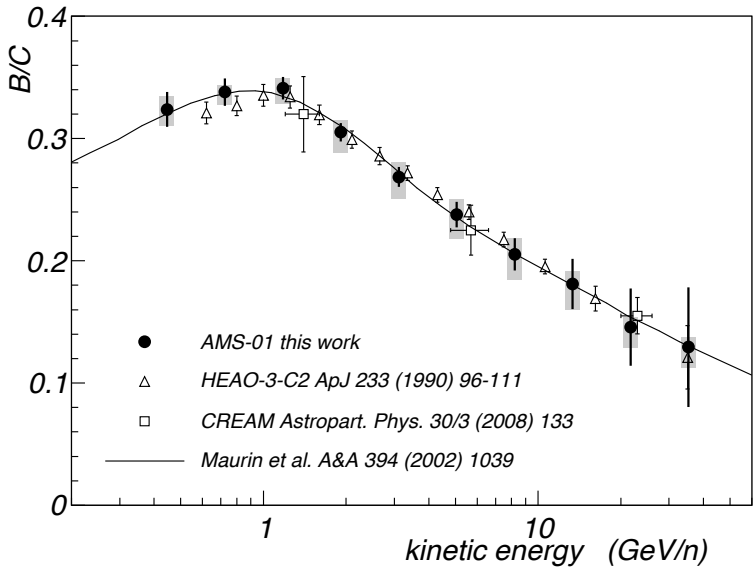

Figure 5.23: Results for the B/C ratio measurement between 0.35 and 45 GeV/n (red markers). The statistical (error bars) and systematic errors (shaded squares) are shown separately. The B/C is compared with HEAO-C2 experiment (open triangles) and CREAM (open squares).

The measurement is shown in Fig.5.23 together with those collected from the HEAO3-C2 experiment [38] from October 1979 and June 1980 (open triangles). AMS-01 data and errors are also summarized in Tab.5.2.
Both the detectors AMS-01 and C2 operated in space during periods of similar solar activity and polarity; altitude and inclination of the orbit were also comparable. The recent result measured by the CREAM collaboration [52] are also reported (open squares). The two measurements are in substantial agreement with the results from this work.

The continuous line describes the B/C distribution in a diffusion halo model (D. Maurin *et al.* [22]) where the magnetic diffusion is considered in terms of a rigidity-dependent diffusion coefficient:

$$D(R) = D_0 \beta \left(\frac{R}{1GV} \right)^{\delta} \tag{5.47}$$

The parameter D_0 is related to the small-scale structure of the galactic magnetic field, and δ specifies the rigidity power-law behaviour of the magnetic diffusion. The

model assumes a rigidity power-law spectrum at the source, resulting from some acceleration process:

$$\frac{dQ}{dR} \propto R^{-\alpha} \tag{5.48}$$

with $\delta = 0.6$ and $\alpha = 2.2$; the solar modulation is described in the force-field approximation using $\Phi = 500MV$ [30], consistent with the period of the AMS-01 flight. As discussed in §1.2.3, many analysis of cosmic rays nuclei assume power laws for the diffusion and acceleration dependencies; these assumptions are supported by the Fermi acceleration models and the theory of scattering in turbulent magnetized plasma. Though the quantities α and δ have in principle to be fixed by the theory, as pointed out by authors, in effective models they may be determined directly from the data, in particular from the B/C. This particular model was cross-checked with HEAO3-C2 data. Including this results will then allow a more precise evaluation of the diffusion coefficient.

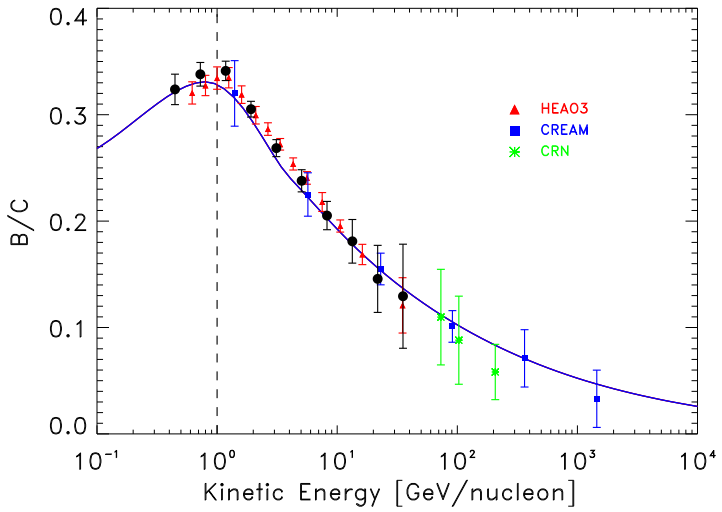

Figure 5.24: B/C Ratio with AMS-01 (black markers), CREAM and CRN. Solid line describe a prediction with DRAGON transport code, where Kolmogorov spectrum ($\delta = 1/3$) has been hypotesized.

Interpretation of the results in terms of propagation parameters is beyond the purpose of this thesis. It is interesting however to compare the measurement with other propagation frameworks. Fig.5.24 shows a B/C computation made with the DRAGON code [131] in a wider energy range, including AMS-01, HEAO, CREAM and CRN data [50]. DRAGON is a numerical model of particle propagation which incorporates all the astrophysical inputs described in §1.2.3, allowing the possibility of using a space-dependent diffusion operator $D = D(E, \mathbf{r})$. Parameter values are $H = 4$ *kpc*

(halo heigh), $\delta = 0.33$ (diffusion spectral index), $V_A = 30\ km \cdot s^{-1}$ (Alfvén velocity). Diffusion is threated assuming $D = D_0 R^{\delta} e^{z/H}$ (with $D_0 = 2.6 \cdot 10^{28} cm^2/s$) that provides a natural escape of cosmic rays at the boundaries of the halo. Data suggest that the Kolmogorov spectrum ($\delta = 1/3$) cannot be excluded, if opportune reacceleration V_A is introduced. Together with more precise high energy data, more realistic descriptions of the cosmic-ray transport are therefore wished. Degeneration of propagation parameters is one of the major issues to be clarified, in order to obtaining conclusive answers on the fundamental questions of the cosmic-ray transport in the galactic medium.

ΔE	**⟨E⟩**	**B/C**	**STAT**	**SYS**
$0.35 \div 0.57$	0.45	0.324	0.014	$^{+0.017}_{-0.018}$
$0.57 \div 0.92$	0.72	0.338	0.011	$^{+0.005}_{-0.010}$
$0.92 \div 1.50$	1.18	0.341	0.009	$^{+0.008}_{-0.013}$
$1.50 \div 2.44$	1.91	0.305	0.007	$^{+0.001}_{-0.017}$
$2.44 \div 3.97$	3.11	0.269	0.008	$^{+0.012}_{-0.018}$
$3.97 \div 6.45$	5.06	0.238	0.010	$^{+0.012}_{-0.020}$
$6.45 \div 10.5$	8.22	0.205	0.013	$^{+0.013}_{-0.021}$
$10.5 \div 17.0$	13.4	0.181	0.020	$^{+0.010}_{-0.021}$
$17.0 \div 27.7$	21.7	0.146	0.031	$^{+0.008}_{-0.017}$
$27.7 \div 45.0$	35.3	0.129	0.049	$^{+0.008}_{-0.017}$

Table 5.2: Results for the B/C ratio between 0.35 and 45 GeV/n of kinetic energy per nucleon. The columns indicate: energy intervals, reference values, B/C values, statistical errors, upper and lower systematic errors.

Conclusions

A new comprehensive measurement of the cosmic-ray B/C ratio has been carried out in this thesis. This study adds to the knowledge that has been obtained during the last decades, from the pioneer balloon-borne experiments up to the most recent projects. Results are in good agreement with those found by the HEAO3-C2 experiment and the new measurement presented by CREAM.

From an experimental point of view, this measurement has represented a challenge for AMS-01, since the experiment was not specifically conceived for this purpose. The low intensity of the ion fluxes, the AMS-01 reduced redundancy and the unfavorable trigger conditions have been the major difficulties that prevented the AMS-01 collaboration from pursuing this effort in the past.

Though the AMS-01 flight was an engineer flight – i.e. its main purpose was validating the employed technology – the statistics, energy range and quality of data were unprecedented and lead to highly interesting results concerning CR physics. A consistent amount of Z>2 nuclei has also been detected and precisely measured. This fact represented the strongest motivation for undertaking this analysis.

The majority of events recorded by AMS-01, for this study, were background cosmic protons and helium nuclei. An excellent separation is provided by the sound combination of TOF and Tracker responses. For background coming from other charged nuclei and mutual contamination between B and C, a novel approach for particle identification has been developed from the data of AMS-01.

Much care has been taken in rejecting background arising from mis-reconstructed events. Low energy particles are dominated by multiple scattering that significantly affects the trajectories. Moreover, the intense delta-ray emission produced secondary tracks or spurious hits that make difficult the track reconstruction.

Modulation effects due to the geomagnetic field, varying along the AMS-01 orbit, have been studied for the two species in order to avoid distortions in the ratio of their energy distributions. The modules of the orbiting space station MIR have been *imaged* in the nuclear channel. To see the MIR as a well defined shadow means that particles coming form MIR can be excluded with a simple geometric cut, with the possibility of considering data coming from the docking phase.

Though many systematic effects were considerably simplified in passing to the ra-

tio, much care and attention has been payed to the trigger efficiency. The AMS-01 trigger response was untrivially influenced by particle interactions occurring in the material. Since the dedicated *unbiased* trigger did not give enough statistics for Z>2 nuclei, the Monte-Carlo technique has been the most appropriate way to perform the estimation. A stand-alone simulation framework has been developed for validating the trigger efficiency under more reliable interaction models. `GEANT3+RQMD`, `GEANT4` and `FLUKA` have been employed for the purpose.

The role of indistinguishable isotopes entering in the measured B/C has been investigated, and a general method for accounting for this uncertainty has been devised. The effects of the instrumental resolution on the B/C have also been investigated using unfolding techniques. This helped in choosing a reasonable energy binning for appreciating the B/C shape while keeping resolution effects at the percent level.

Several possible sources of uncertainty have been considered in the measurement: statistics, MC finite production, charge contamination, resolution, isotopic composition and trigger efficiency. Recommendations for future works arose from these studies.

Future experiments will have to better investigate the role of all light and heavy CR ion energy spectra. Major challenges are reaching higher energies and better precision in the fluxes determination.
AMS-02 will be installed on the International Space Station (ISS) in July 2010 with the NASA shuttle mission STS-134. It represents a largely improved version of the AMS-01 spectrometer.
Once installed on the ISS, AMS-02 will be operational for 3 years. This long exposure time, together with the large acceptance $A_G \approx 0.45\ m^2sr$, will produce an improvement of a factor of 10^3 in sensitivity. Based on the experience with AMS-01, a more refined trigger will be implemented for AMS-02 to precisely determine the detection efficiencies. Improved Monte-Carlo simulations and analysis techniques are also on the agenda. All the new AMS-02 subdetectors have been built and successfully tested with particle beams and cosmic-ray muons, proving enhanced performance and suitability for space. The spectrometer has recently been integrated in its final configuration for the flight.

Accurate measurements of the CR energy spectra and chemical composition are therefore expected for a large rigidity range (up to some TV) and high charge values (up to Iron).
Expectations for the B/C ratio (Fig.5.25, on the basis of a `GALPROP` prediction) as well as other secondary/primary ratios are therefore particularly promising: conclusive constraints on the propagation parameters will shed light on open matters

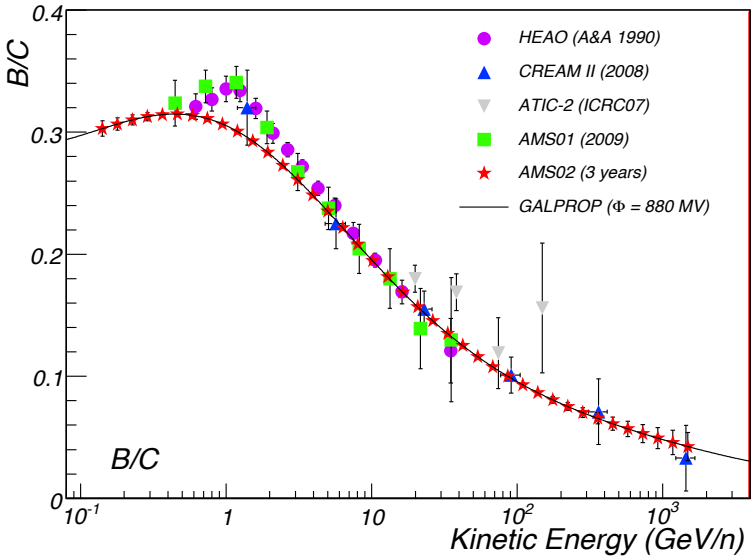

Figure 5.25: AMS-02 potential for the measurement of the B/C ratio after three years of data taking. The prediction is calculated with the conventional diffusion model from GALPROP [20] modulated with $\Phi = 800\ MV$.

in astrophysics and cosmology. An understanding of the galactic structure as well as cosmic-ray processes is the key to investigate the CR sources, including ordinary things, like stars and supernovas, as well as exotica like quark stars, dark matter annihilation or antimatter galaxies.

Exploring a new territory with a precision instrument is the key to discovery. New exciting questions are sure to be raised by the results of the Alpha Magnetic Spectrometer in space.

Acknowledgement

I want to thank all the people involved in the development of this thesis. Thanks to prof. Roberto Battiston for giving me the opportunity to work on this fascinating subject. Very special thanks go to my advisors: prof. Bruna Bertucci for her continuous encouragement and supervision in the development of this thesis, and Emanuele Fiandrini for his support and appreciation of my work. Moreover, I benefited quite a bit from the aid and knowledge of many members of the AMS group. Sincere thanks to Alberto Oliva for his invaluable contribution to the VMC project. Thanks to Giovanni Ambrosi for sharing his experience and knowledge of the AMS detector. Thanks to Paolo Zuccon for clarifying discussions on many aspects of the data analysis. Thanks to Sadakazu Haino for his precious remarks and Gabriele Alberti for his prompt technical support. Grazie Bill Burger pour sa conseils and Matteo Duranti for countless discussions. Thanks to Vitaly Choutko for his support, indeed vital, with the MC production, and Yue Zhou for his pioneering work on the TGeometry classes. Other cumulative thanks are addressed to all the individuals around the AMS experiment in Perugia and the collegues that shared my office during this PhD adventure.

Bibliography

[1] T.K. Gaisser, *Cosmic Rays and Particle Physics* (1990) Cambridge.

[2] G. Jungman *et al.*, Phys. Rep. 267 (2006) 295-373.

[3] E.N. Parker, Planet. Space. Sci. 13 (1965) 9.

[4] A.M. Hillas astro-ph/0607109 (2006)

[5] C. Amsler *et al.*, Phys. Lett. B 667 (2008) 1.

[6] V.S. Berezinsky *et al.*, *Astrophysics of Cosmic Rays*, North Holland (1990) Amsterdam.

[7] J. Horandel, astro-ph/0702370v2 (2007).

[8] T. Antoni *et al.*, Phys. Rev. Lett. 24 (2005) 1-25.

[9] K. Greisen, Phys. Rev. Lett. 16 (1966) 748.

[10] Auger Collaboration, Science 318 5852 (2007) 938.

[11] J.A. Simpson & J.J. Connel, ApJ 497 (1998) L85-L88.

[12] A.W. Strong & I. Moskalenko, ApJ 591 (2003) 1220-1247.

[13] V.L. Ginzburg, Uspekhi Fiz Nauk 39 (2) (1996) 155.

[14] E. Fermi, Phys. Rev. 75 (1949) 1169.

[15] M.S. Longair, *High Energy Astrophysics* (2004) Cambridge Univ. Press.

[16] A.M. Hillas, *Cosmic Rays*,Pergamon Press (1972), Oxford

[17] A.R. Bell, Mon. Not. R. Astr. Soc. 182 (1987) 147.

[18] V.L. Ginzburg & S.I Syrovatskii *The Origin of Cosmic Rays*, Pergamon Press (1964) Oxford.

[19] M. Simon, Frascati Physics Series Vol. XXIV (2002) 119-136.

[20] A.W. Strong & I.V. Moskalenko, ApJ 509 (1998) 212.

[21] D. Maurin *et al.*, ApJ 555 (2001) 585.

[22] D. Maurin *et al.*, A&A 394 (2002) 1039;

[23] W.R. Webber *et al.*, Phys. Rev. C41 (1990) 520.

[24] U. Heinbach & M. Simon, ApJ 441 (1995) 209.

[25] I. Lerche & R. Schlickeiser, A&A 151 (1985) 408-420.

[26] V.S. Ptuskin *et al.*, ApJ 465 (1996) 972-981.

[27] F.C. Jones, Proc 22^{nd} ICRC, Ireland (1991) OG-8.2.9, 268

[28] S.A. Stephens & R.E. Streitmatter, ApJ 505 (1998) 266-277.

[29] F.C. Jones, Phys. Rev. 2 (1970) 2787.

[30] L.J. Gleeson & WI Axford, ApJ 154 (1968) 1011;

[31] D.F. Smart *et al.*, J. Geophys. Res. 70 (1965) 4117.

[32] M.A. Huang, AMS-Note 44 (1995) 274; astro-ph/0104229v1 (2001).

[33] C.Z. Stormer, Astroph. 1 (1930) 237.

[34] C.Z. Stormer, *The Polar Aurora*, McGraw-Hill (1955).

[35] G. Gustafsson *et al.*, J. Atmos. Terr. Phys. 54 (1992) 1609.

[36] N. Olsen *et al.*, Geophys. Res. Lett. 27 (2000) 3607.

[37] A. Molnar & M. Simon, Proc 27^{th} ICRC, Germany (2001) 1860.

[38] J.J. Engelman *et al.*, ApJ 233 (1990) 96-111;

[39] J.F. Ormes & R.J. Protheroe, ApJ, 272 (1983) 756.

[40] L.C. Tan *et al.*, Proc 20^{th} ICRC, USSR V2 (1987) 239.

[41] K.E. Krombel, M.E. Wiedenbeck, ApJ 328 (1987) 940.

[42] M. Gupta & W.R. Webber, ApJ 540 (1989) 1124-1134.

[43] L. Koch-Miramond *et al.*, Proc 18^{th} ICRC, India (1983) V9-275.

[44] F.C. Jones *et al.*, ApJ 547 (2001) 264-271.

[45] R.H. Kraichnan, Phys. Fluids 8 (1965) 1385.

[46] E.G. Berezhko *et al.*, A&A 410 (2003) 189.

[47] R. Taillet *et al.*, ApJ 609 (2004) 173.

[48] A. Castellina & F. Donato, Astropart. Phys. 24 (2005) 146-159.

[49] M. Ave *et al.*, Apj 697 (2009) 106-114.

[50] D. Muller *et al.*, ApJ 374 (1991) 356-367.

[51] Y. Takahashi *et al.*, Nucl. Phys. B 60B (1998) 83-92.

[52] H.S. Ahn *et al.*, Astrop. Phys. 30-3 (2008) 133-141.

[53] A.D. Panov *et al.*, Proc 30^{th} ICRC, Mexico V2 (2007) 3.

[54] E.C. Stone *et al.*, Spac. Sci. Rev. 86 (1998) 1-4.

[55] A.J. Davis *et al.*, AIP Conf. Proc. 528 (2000) 421.

[56] A.W. Strong & I.V. Moskalenko, Proc 31^{st} ICRC, Poland (2009).

[57] E. Júliusson, ApJ 191 (1974) 331–348.

[58] C.D. Orth *et al.*, ApJ 226 (1978) 1147-1161.

[59] R.C. Maehl *et al.*, Astr.& Space Sci., 43 (1977) 163.

[60] J.H. Caldwell *et al.*, ApJ 218 (1977) 269-285.

[61] J.A. Lezniak & W.R. Webber, ApJ 223 (1978) 676-696.

[62] M. Simon *et al.*, ApJ 239 (1980) 712-724.

[63] A. Lukasiak *et al.*, Proc 26^{th} ICRC, USA. Vol.3 (1999) 389-391.;

[64] F.B. McDonald *et al.*, A&A 599 (2003) 582-595.

[65] R. Dwyer & P. Meyer, ApJ 322 (1987) 981-991.

[66] J. Buckley *et al.*, ApJ 429 (1994) 736-747.

[67] M. Hareyama & T. Shibata, J. of Phys. 47 (2006) 106-112.

[68] J.T. Link *et al.*, Proc 28^{th} ICRC, Japan (2003).

[69] S. Ahlen *et al.*, Nucl. Inst. Meth. **A**350 (1994) 351-367.

[70] M. Aguilar *et al.*, Phys. Rep., Vol.366/6 (2002) 331-405.

[71] P. Chardonnet *et al.*, Phys. Lett. B 409 (1997) 313-320.

[72] N. Tomassetti, Master Thesis (2006), Perugia University.

[73] S.W. Barbwick *et al.*, ApJ 482 (1997) L191.

[74] M. Aguilar *et al.*, Phys. Lett. B646 (2007) 145-154.

[75] O. Adriani *et al.*, Nature 458 (2009) 607-609.

[76] J. Chang *et al.*, Nature 456 (2008) 362.

[77] A.A. Abdo *et al.*, Phys. Rev. Lett. 102 (2009) 181101.

[78] M. Aguilar *et al.* (AMS), Proc. Space Part (2006), Beijing.

[79] D. Alvisi *et al.*, Nucl. Inst. Meth. A 437 (1999) 212.

[80] R. Battiston, Nucl. Phys. Proc. Suppl 44 (1995) 274.

[81] W. J. Burger, Nucl. Phys. Proc. Suppl 113 (2002) 139.

[82] G. Batignani *et al.*, Nucl. Inst. Meth. A 277 (1989) 147.

[83] M. Acciarri *et al.*, Nucl. Inst. Meth. A 351 (1994) 300.

[84] J. Alcaraz *et al.*, Nuovo Cimento II 112A (1999) 1325-1344.

[85] F. Barao *et al.*, AMS-Note (October 1, 1999).

[86] V. Choutko, AMS-Note (May 1, 1998).

[87] V. Choutko, AMS-Note (June 4, 1999).

[88] V. Plyaskin, AMS-Note (April 22, 1997).

[89] V. Choutko, AMS-Note (November 29, 1996).

[90] V. Choutko, AMS-Note (January 10, 2003).

[91] J.C. Hart & D.H. Saxon, Nucl. Inst. Meth. 220 (1984) 309.

[92] V. Innocente & E. Nagy (`GEANE`), Nucl. Inst. Meth. A 324 (1993) 297.

[93] R. Brun *et al.* (`GEANT3`), DD/EE/84-1 (1987) CERN.

[94] R.E. Kalman, J. Basic Engineering 82-1 (1960) 35-45.

[95] H. Sorge (RQMD), Phis. Rev. C52 (1995) 3291.

[96] B. Anderson *et al.*, Nucl. Phys. B 281 (1987) 289

[97] I. Hrivnacova *et al.* (VMC), Proc. CHEP (2003) La Jolla (CA).

[98] R. Brun *et al.* (ROOT), Linux J. 51 (1998).

[99] S. Agostinelli *et al.* (GEANT4) Nucl. Inst. Meth. A 506 (2003) 250-303.

[100] J.J. Gaimard & K.H. Schmidt, Nucl. Phys. Rev. C 22 (1980) 1184.

[101] A. Ferrari *et al.* (FLUKA) Nucl. Instr. Meth. **B71** (1992) 412.

[102] J. Ranftm (DPMJET), SI-99-9 (1999), Siegen University.

[103] *STS-91 Mission Highlight*, IS-1998-06-001-091, NASA/JSC Publications.

[104] http://spaceflight.nasa.gov/history/shuttle-mir/index.html.

[105] J. Alcaraz *et al.*, Phys. Lett. B461 (1999) 387-396;

[106] H. Suter, Flight Parameters for Mission STS-91 (1999) ETH, Zurich.

[107] J. Alcaraz *et al.*, Phys. Lett. B472 (26 Jan 2000) 215-226;

[108] J. Alcaraz *et al.*, Phys. Lett. B484 (2000) 10-22.

[109] J. Alcaraz *et al.*, Phys. Lett. B490 (28 Sep 2000) 27-35;

[110] J. Alcaraz *et al,*, Phys. Lett. B494 (30 Nov 2000) 193-202;

[111] E. Fiandrini *et al.*, J. Geophys. Res. 109 (2004) A 10394

[112] R. Henning, Phd Thesis (2003), MIT, Cambridge.

[113] M. Cristinziani, Phd Thesis (2002), Geneve University.

[114] NASA-GRIN http://grin.hq.nasa.gov/ABSTRACTS/GPN-2000-001315.html

[115] M. Aguilar *et al.*, Nucl. Inst. Meth. B 234 (2005) 321-332.

[116] H. Bethe, J. Ashkin, Exp. Nucl. Phys. (1953) J. Wiley, NY.

[117] L.D. Landau, J. Exp. Phys. **8**, (1944) 201.

[118] P.V. Vavilov, Sov. Phys. JETP **5** (1957) 749.

[119] K. Molino, Master Thesis (1999), Bologna University.

[120] O. Toker *et al.*, Nucl. Inst. Meth. A 340 (1994) 572.

[121] A. Korejwo *et al.*, J. Phys G: Nucl. Part. Phys 28 (2002) 1199.

[122] J.D. Sullivan, Nucl. Inst. Meth. 95 (1971) 5-11.

[123] M. Paterno, D0 Note N. 2861 (1996), FNAL.

[124] G. D'Agostini, Nucl. Inst. Meth. **A362** (1995) 487;

[125] A. Kondor, Nucl. Inst. Meth. **216** (1983) 177;

[126] G. Lamanna, Phd Thesis (2000), Perugia University.

[127] P. Fontes, Phys. Rev. C15 6 (1977) 2159-2168

[128] G.A. de Nolfo *et al.*, Adv. Space Res. 38 (2006) 1558-1564.

[129] M. Garcia-Munoz *et al.*, ApJ 217 (1977) 859-877.

[130] S.P. Ahlen *et al.*, ApJ 534 (2000) 757-769;

[131] C. Evoli *et al.*, Proc 31^{st} ICRC, Poland (2009).